

Size Effects on Lithium Storage and Phase Transition in $\text{LiFePO}_4/\text{FePO}_4$ System

Von der Fakultät Chemie der Universität Stuttgart
zur Erlangung der Würde eines Doktors der
Naturwissenschaften (Dr. rer. nat.)
genehmigte Abhandlung

Vorgelegt von

Changbao ZHU

aus Zhangjiakou, Hebei, China

Hauptberichter: Prof. Dr. Joachim Maier

Mitberichter: Prof. Dr. Joachim Bill

Prüfungsvorsitzender: Prof. Dr. Cosima Stubenrauch

Tag der mündlichen Prüfung: 17.05.2013

Max-Planck-Institut für Festkörperforschung

Stuttgart

2013

Erklärung

Die vorliegende Doktorarbeit wurde vom Autor selbst in der Abteilung von Prof. Maier am Max-Planck-Institut für Festkörperforschung, im Zeitraum von September 2009 bis März 2013 angefertigt. Der Inhalt ist die eigene Arbeit des Autors, Ausnahmen sind gekennzeichnet, und wurde noch nicht zur Erlangung einer Qualifizierung oder eines Titels an einer akademischen Institution eingereicht.

Stuttgart, March 25, 2013

Changbao ZHU

Declaration

The work described in this thesis was carried out by the author in the Department of Prof. Maier at the Max Planck Institute for Solid State Research from September 2009 to March 2013. The contents are the original work of the author except where indicated otherwise and have not been previously submitted for any other degree or qualification at any academic institution.

Stuttgart, March 25, 2013

Changbao ZHU

Contents

Zusammenfassung	1
Abstract	3
1. Introduction and motivation	5
1.1 Basic aspects of lithium battery.....	6
1.2 General introduction on LiFePO ₄	9
1.3 Defect Chemistry of LiFePO ₄ / FePO ₄ redox couple.....	14
2. Instrumental techniques	20
2.1 Structural characterization.....	20
2.1.1 X-ray diffraction (XRD).....	20
2.2 Electron microscopy.....	21
2.2.1 Scanning electron microscopy (SEM).....	21
2.2.2 Transmission electron microscopy (TEM).....	22
2.2.3 Scanning transmission electron microscopy (STEM) and annular-bright-field (ABF).....	23
2.3 Electrochemical characterization.....	24
2.3.1 Cyclic voltammetry (CV).....	24
2.3.2 Galvanostatic intermittent titration technique (GITT).....	25
2.3.3 Potentiostatic intermittent titration technique (PITT).....	26
2.4 Instrumental details.....	28
3. Synthesis and electrochemical performance of LiFePO₄	30
3.1 Introduction.....	30
3.2 Electrospinning of carbon-coated single crystalline LiFePO ₄ nanowires..	32
3.2.1 Introduction.....	32
3.2.2 Synthesis.....	33
3.2.3 Results and discussions.....	34
3.2.3.1 Morphology and formation mechanism of LiFePO ₄ nanowires..	34
3.2.3.2 Electrochemical performance of LiFePO ₄ nanowires.....	40

3.2.4	Conclusions.....	46
3.3	Surfactant-assisted polyol method for preparation of LiFePO_4 nanoparticles.....	46
3.3.1	Introduction.....	47
3.3.2	Synthesis.....	47
3.3.3	Results and discussions.....	48
3.3.3.1	Size controlled synthesis of LiFePO_4 nanoparticles.....	48
3.3.3.2	Formation mechanism of LiFePO_4 nanocrystals in the OL-assisted polyol method.....	53
3.3.3.3	Electrochemical performance of LiFePO_4 nanoparticles.....	54
3.3.4	Conclusions.....	61
3.4	Amorphous LiFePO_4 by precipitation method.....	61
3.4.1	Introduction.....	61
3.4.2	Preparation of amorphous LiFePO_4	62
3.4.3	Results and discussions.....	62
3.4.3.1	Characterization of amorphous LiFePO_4	62
3.4.3.2	Electrochemistry of amorphous LiFePO_4	67
3.4.4	Conclusions.....	68
3.5	Conclusions.....	68
4.	Size effects on lithium storage in LiFePO_4.....	70
4.1	Introduction.....	70
4.2	Experimental.....	72
4.3	Size effect on the miscibility gap of LiFePO_4	73
4.4	Lithium potential variations for metastable LiFePO_4	76
4.5	Conclusions.....	88
5.	Size effects on phase transition process in $\text{LiFePO}_4/\text{FePO}_4$.....	90
5.1	Introduction.....	90
5.2	Experimental.....	92
5.3	Phase transition in large LiFePO_4 single crystal.....	94
5.4	Size-dependent staging and phase transition in $\text{LiFePO}_4/\text{FePO}_4$	98

5.4.1 Direct observation of Li staging in partially delithiated LiFePO_4	98
5.4.1.1 Literature review on phase transition in LiFePO_4 investigated by conventional TEM technique.....	98
5.4.1.2 Observation of staging structure for partially delithiated LiFePO_4 by STEM-ABF technique.....	101
5.4.2 Size-dependent lithium staging structure.....	105
5.5 Conclusions.....	113
6. Overall Conclusions.....	115
Appendix.....	118
References.....	121
Abbreviations and Symbols.....	131
Acknowledgement.....	135
Curriculum Vitae.....	137

Zusammenfassung

LiFePO₄ hat als eines der vielversprechendsten Kathodenmaterialien, vor allem hinsichtlich seines Potentials in Elektro- oder Hybridfahrzeugen kürzlich großes Interesse geweckt. Dies beruht vor allem auf den attraktiven Vorteilen einer hohen theoretischen Kapazität (170 mAhg⁻¹), einer hohen Sicherheit in der Anwendung, einer guten Umweltverträglichkeit und einer preiswerten Verfügbarkeit. Obwohl bereits große Fortschritte in Bezug auf elektrochemische Leistungsfähigkeit von LiFePO₄ durch Dotieren, Verringerung der Größe oder Netzwerkbildung erzielt wurden, sind einige intrinsische Eigenschaften von LiFePO₄ noch immer nicht aufgeklärt und bedürfen weiter gehender Untersuchungen. Einen der wichtigsten Aspekte stellen die Größeneffekte in Bezug auf Lithiumspeicherung sowie der Phasenübergang in LiFePO₄/FePO₄-Systemen dar, welche nicht nur für das grundlegende Verständnis des Verhaltens von LiFePO₄ bedeutsam sind, sondern auch von hoher Relevanz für die Anwendung dieser Materialien sind.

In dieser Arbeit wurden zu Beginn geeignete Synthesen zur Kontrolle der Morphologie und Größe von LiFePO₄ sowie die entsprechende elektrochemische Leistungsfähigkeit diskutiert. Im Anschluss daran wurden Größeneffekte auf die Mischungslücke, die Variationen des Lithiumpotentials sowie den Phasenumwandlungsprozess systematisch untersucht. Die hauptsächlichen Schlussfolgerungen sind wie folgt:

Mit Kohlenstoff beschichtete einkristalline LiFePO₄-Nanodrähte wurden erfolgreich mittels der Methode des Elektrosplennens hergestellt, welche eine gute Ratenleistungskurve und eine exzellente Zyklenstabilität aufgrund der einzigartigen Morphologie aufweisen.

Kleine LiFePO₄-Partikel (Dicke lediglich ca. 10 nm) können durch die Polyolmethode unter Verwendung von Oleylamin hergestellt werden, während die Partikelgrößen durch schrittweise Anpassung der experimentellen Parameter variiert

werden können, wie etwa das Verhältnis von Oleylamin zu TEG, Eduktkonzentration, Reaktionszeit und das Hinzufügen von Kohlenstoffnanoröhrchen. Das Sintern des Materials bei 700 °C für 2 Stunden resultiert in einer guten elektrochemischen Leistungsfähigkeit.

Das Schrumpfen der Mischungslücke durch Reduktion der Partikelgröße wurde anhand einer potentiostatischen Puls-Technik verfolgt. Zudem wurden im Ein- und Zweiphasenregime Variationen des Lithiumpotentials für nanokristallines und amorphes LiFePO_4 beobachtet und systematisch in thermodynamischer und experimenteller Hinsicht untersucht. Für nanokristallines LiFePO_4 wurden verringerte Zellspannungen als Folge der Reduktion der Partikelgrößen gefunden. Es wurde gezeigt, dass nicht nur die Größe, sondern auch die Oberflächenchemie eine entscheidende Rolle spielt. Große Zellspannungseffekte werden auch für amorphes LiFePO_4 gefunden, die auf die veränderte Thermodynamik von Ionen- und Elektroneneinbau zurückgehen.

Der Phasenübergang innerhalb eines großen LiFePO_4 -Einkristalls wurde mittels chemischer Delithiierung untersucht. Es entstanden FePO_4 -Schichten mit hoher Porosität. Die Kinetik wird durch ein quadratisches Wachstumsgesetz bestimmt, was auf Diffusionslimitierung hinweist. Allerdings ist die effektive Diffusion in diesem inhomogenen Netzwerk aus Poren und Rissen gegenüber dem reinen Festkörper deutlich erhöht.

Mit Hilfe von speziellen STEM-ABF Techniken konnte eine langreichweitige Ordnung für die partiell delithiierten $\text{Li}_{1-x}\text{FePO}_4$ ($x \sim 0,5$) Nanodrähte beobachtet werden. Ebenso wurde beobachtet, dass diese überraschende Struktur auch als Grenzflächenphase zwischen FePO_4 und LiFePO_4 auftritt. Die Dicke derselben erhöht sich mit kleiner werdender Partikelgröße.

Abstract

LiFePO₄ is one of the most promising cathode materials, especially for its great potential to be applied in electric vehicles (EVs) and hybrid electric vehicles (HEVs), and has attracted great interest due to its appealing advantages, such as high theoretical capacity (170 mAhg⁻¹), high safety, environmental benignity and low cost. Although a great improvement has already been reached in terms of electrochemical performance of LiFePO₄ by doping, size-reduction, and network formation, several intrinsic properties of LiFePO₄ are still not clear and need further investigation. One of the most important unresolved issues is the effect of size on lithium storage and phase transition in the LiFePO₄/FePO₄ system, which is not only crucial for fundamental understanding of LiFePO₄ behavior, but also relevant to the application of such materials.

In this thesis, morphology and size controlled synthesis of LiFePO₄ and related electrochemical performance are discussed at first. Afterwards, size effects on miscibility gap, lithium potential variations and phase transition process are investigated systematically. The main results of this thesis are the following:

Carbon-coated single-crystalline LiFePO₄ thin nanowires are successfully prepared by the electrospinning method, which show good rate performance and excellent cycling stability due to the unique morphology.

Small LiFePO₄ nanoparticles (the thickness only around 10 nm) can be prepared by the oleylamine-assisted polyol method and the particle sizes can be controlled by adjusting experimental parameters, such as the ratio of oleylamine to tetraethylene glycol (TEG), the precursor concentration, the reaction time and the addition of carbon nanotubes. After sintering at 700 °C for 2 hours the material displays excellent electrochemical performance.

The shrinking of the miscibility gap with reduction of the particle size is observed by the potentiostatic intermittent titration technique (PITT). Lithium

potential variations for nanocrystalline and amorphous LiFePO_4 are investigated thermodynamically and experimentally by considering the lithium intercalation regime (single phase regime and two phase regime). For nanocrystalline LiFePO_4 , the reversible open-circuit voltage (OCV) values decrease with reduction of particle sizes. Surface chemistry (γ) plays a crucial role in the OCV variations. For amorphous LiFePO_4 , compared with crystalline Li_xFePO_4 , the excess OCV can be either negative or positive, which can be explained by the signs of the ionic part and the electronic part of the excess chemical potential of lithium.

Phase transition of large LiFePO_4 single crystal is investigated by chemical delithiation. FePO_4 layers with high porosity and cracks are observed at the surface of LiFePO_4 . The kinetics is governed by a parabolic growth law that indicates diffusion limitation. The pore/crack network provides fast diffusion channels and enhances the kinetics pronouncedly.

With the help of the advanced scanning transmission electron microscopy with annular bright field imaging (STEM-ABF) performed in Sendai (Japan), a first order lithium staging structure is directly observed in the partially delithiated $\text{Li}_{1-x}\text{FePO}_4$ ($x \sim 0.5$) nanowires for the first time. Size-dependent staging structure is also found. For large crystals, staging structures form an intermediate phase between LiFePO_4 and FePO_4 , and the staging area narrows with increasing size. For small crystals, the staging structure appears throughout the whole particle.

Chapter 1

Introduction and motivation

The objective of this work is to investigate the size effects on lithium storage and phase transition in $\text{LiFePO}_4/\text{FePO}_4$. In order to study such size effects together with the related electrochemical performance, LiFePO_4 with various particle sizes, crystallinities and morphologies has to be prepared. The thesis is structured as follows:

In Chapter 1 basic aspects of lithium batteries and LiFePO_4 cathode materials are presented.

In Chapter 2 the most important instrumental techniques and instrumental details used in this work are introduced.

Chapter 3 contains morphology- and size-controlled synthesis of LiFePO_4 and the corresponding electrochemical performance. Carbon-coated single crystalline LiFePO_4 nanowires with good electrochemical performance were successfully prepared by the electrospinning technique. In addition, size controlled preparation of LiFePO_4 nanoparticles was performed by the surfactant-modified polyol method. Detailed experimental parameters such as the surfactant concentration, reaction temperature, reaction time, and precursor concentration were carefully adjusted to control the particle size. Last but not least, amorphous FePO_4 and LiFePO_4 were prepared by the precipitation method.

In Chapter 4 lithium potential variations for metastable phases (nanocrystalline vs. amorphous phase) are predicted considering both the single phase and the two phase regime. Furthermore, nanocrystalline LiFePO_4 with different particle sizes and amorphous $\text{LiFePO}_4/\text{FePO}_4$ are investigated using thermodynamic considerations of the obtained experimental results.

In Chapter 5 the phase transition mechanism for large single crystals and nanosized LiFePO_4 were systematically investigated. Especially, the focus was put on

the staging effect in LiFePO_4 with different sizes (70 nm and 50 nm) and morphologies (nanowires and particles). Finally, these findings are discussed in the light of phase transition thermodynamics and kinetics.

Chapter 6 summarizes the most important conclusions regarding size effects on lithium storage and phase transition in LiFePO_4 and FePO_4 system.

1.1 Basic aspects of lithium battery

The importance of energy storage and its link to environmental issues is universally recognized. Major concerns refer to the present energy economy based on fossil fuels, which leads to depletion of the non-renewable energy sources, to unstable oil production due to political reasons and presumably to dramatic climate changes associated with high CO_2 emission.¹

Therefore it is advised to reduce greenhouse gas emissions by using clean and renewable energy such as solar, wind, geothermal and nuclear energy.² Nuclear reactors are able to provide a constant energy source, however, they are associated with problems of radioactive waste disposal. Geothermal energy is limited by location. Solar and wind energy technologies are fairly mature, but the intermittence of these resources is dependent on high efficiency energy storage systems. There are four types of energy storage technologies available³ based on mechanical, electrical, chemical and electrochemical modes. Among those, electrochemical energy storage based on batteries is very promising. Replacing the internal combustion engine (ICE) vehicles¹ with electric vehicles (EVs) and hybrid electric vehicles (HEVs) is a possible way to mitigate CO_2 emission in the future. Therefore, the development of rechargeable batteries with high energy density, high power density and high safety is of particular interest.

The rechargeable lithium battery is at present a most promising battery system. Since Sony announced commercialized lithium ion battery (LIB) for the first time in 1991, LIB has greatly increased the quality of our everyday life. Many new types of portable electronic devices (e.g. laptop, cell phone, MP3 player, iPhone and iPad) are taking advantage of this advanced technology and are being used worldwide for the

past decades. Recently, pushed forward by green technologies, the application of LIB expanded from portable electronics to large scale ones, particularly EVs and HEVs. The wide application of LIB lies in its high energy and power densities compared to other battery systems, such as lead acid, nickel-cadmium and nickel-metal hydride batteries as shown in Figure 1.1.

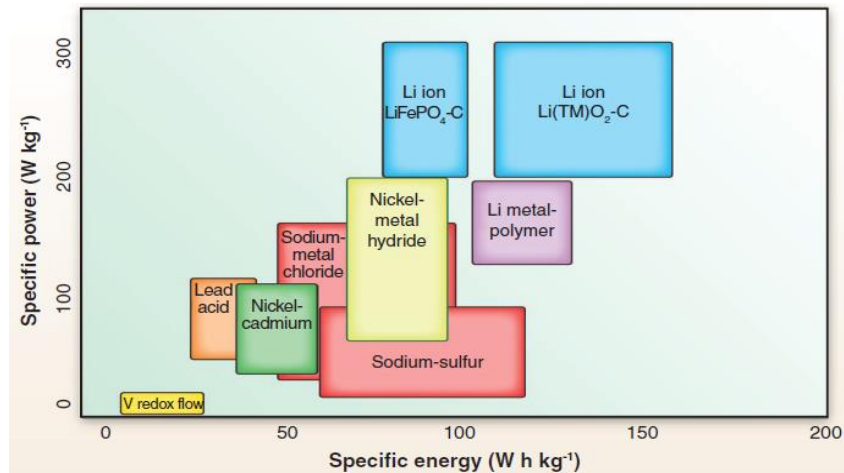


Figure 1.1 Comparison of gravimetric power and energy densities for different rechargeable battery systems.³

A typical lithium battery mainly consists of four parts: cathode, anode, electrolyte and separator. The most common anode materials are graphite (e.g. mesocarbon microbeads, MCMB¹) and materials based on alloy reactions, such as Sn, which have also been commercialized as NEXELION.³ Firstly used cathode materials are layered lithium transition metal oxide⁴ (e.g. LiCoO_2), a class of electrodes that was later expanded to lithium manganese oxide spinels^{5, 6} (LiMn_2O_4) and lithium transition-metal phosphate^{7, 8} (LiFePO_4) in order to reduce the cost, improve the safety, and increase energy and power densities. A solution of a lithium salt (e.g. LiPF_6) in a mixed organic solvent (e.g. ethylene carbonate - dimethyl carbonate, EC-DMC) soaked in a separator (Celgard) is the commonly used LIB electrolyte system¹. The on-going electrolyte research is focusing on polymer electrolytes,^{9, 10} electrolyte additives,^{11, 12} and ionic liquid based electrolytes¹³⁻¹⁵ for further battery safety improvement.

Let us take the firstly used battery system (LiCoO₂/graphite) as an example to understand the basic working principle of LIB. During the charge/discharge process, lithium ions are shuttled between the cathode (working potential is generally higher than 3 V vs. Li⁺/Li) and anode through a non-aqueous electrolyte which is sandwiched between the cathode and anode (Figure 1.2). Both cathode and anode can reversibly insert and withdraw Li ions from their respective structures. During the discharging process, Li ions are removed from graphite and inserted into layered transition metal oxide (LiCoO₂) simultaneously, while the electrons are transported from anode to the cathode through an external circuit. On charging directions of transport for lithium ions and electrons are reversed.

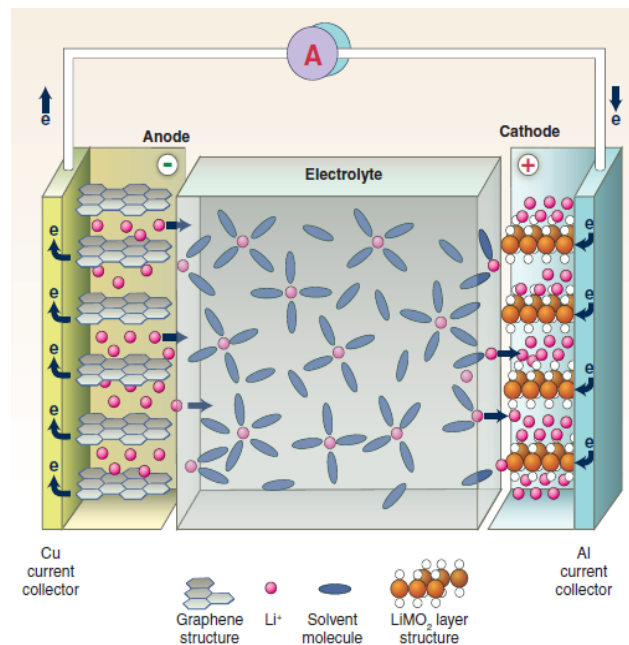


Figure 1.2 Schematic of the LIB working principle.³

On discharging, from the electrochemical point of view, the anode is the reductant and the cathode is the oxidant. During discharging, lithium is oxidized to Li⁺ and loses one electron, while the transition metal ion is reduced and accepts one electron. Electrons flow from the anode through the external circuit where they can do useful work before reaching the cathode. This is a typical process by which batteries convert chemical to electrical energy. From the thermodynamic point of view, the cell

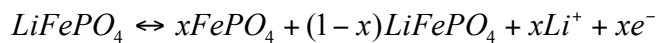
voltage is determined by the difference of chemical potentials of lithium between anode (μ_A) and cathode (μ_C) within the electrochemical window of electrolyte. It holds

$$\mu_C - \mu_A = -nEF = \Delta_r G, \quad (1-1)$$

where n is the number of electrons per mole transferred in the redox reaction, E is the thermodynamic equilibrium cell voltage (electromotive force, e.m.f, or open circuit voltage, OCV), F is the Faraday constant and $\Delta_r G$ is the Gibbs free energy of the reaction.

1.2 LiFePO₄ as a cathode material for lithium battery

LiFePO₄ has been considered as the most promising cathode materials, especially for its great potential for the next-generation large-scale lithium ion batteries to be applied in EVs or HEVs, due to its appealing advantages, such as high theoretical capacity (170 mAhg⁻¹), high safety, environmental benignity and low cost. LiFePO₄ is a typical material with a two phase reaction mechanism⁷ (e.g. nucleation and growth of second phase during phase transition process) as $V = 3.45$ V vs. lithium over a large composition range based on the following reaction:



Its excellent electrochemical cycling stability is attributed to the potential which lies in the window of presently used carbonate electrolytes. This cathode material was first proposed by Goodenough and coauthors in 1997,⁷ and since then, a number of studies have been done to investigate synthesis routes,¹⁶⁻¹⁹ crystallographic structure,^{20, 21} defect chemistry,²² prospective physical,²³ chemical²⁴ and electrochemical properties.²⁵

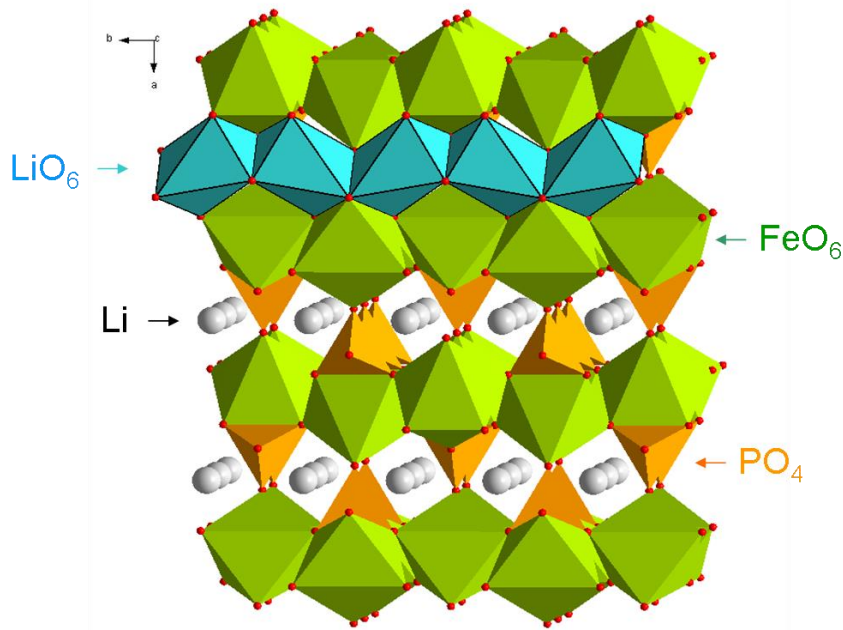


Figure 1.3 Crystal structure of LiFePO_4 along $[001]$ direction.

LiFePO_4 is a typical polyoxyanionic structure (M-O-X bonds) material, whose nature will change through inductive effect by the ionic-covalent character of the M-O bonding.²⁶ LiFePO_4 has a distorted hexagonal close packed olivine structure with a space group $Pnma$. There are two distinct octahedral positions in the lattice: the M1 site on an inversion center and the M2 site on a mirror plane. Li usually occupies M1 sites and Fe occupies M2 sites whereas P occupies tetrahedral sites. The FeO_6 octahedra are linked together by corner sharing in the $b - c$ plane (Fig. 1.3). LiO_6 octahedra share edges with each other along the b -axis creating a one dimensional channel for Li transport (marked blue in Fig.1.3). PO_4 groups connect the frameworks of FeO_6 with one edge and share two edges with LiO_6 . Corner-shared FeO_6 octahedra are separated by the oxygen atoms of PO_4 tetrahedra and cannot form a continuous FeO_6 network. Due to the strong covalent P-O bonds in the PO_4 , the skeleton of PO_4 polyanions is very stable. On the other hand, the fully delithiated phase FePO_4 has essentially the same crystallographic structure.²⁷ However, upon removal of all the lithium from the structure, the FePO_4 framework deforms slightly from orthorhombic symmetry. The detailed crystallographic information has been retrieved by single

phase Rietveld refinement of powder XRD data²⁸ and Neutron powder diffraction.²⁹ After removing lithium from LiFePO_4 frameworks, the volume decreases by 6.81% and the material's density increases by 2.59%.³⁰

Several intrinsic properties (both advantageous and disadvantageous) of LiFePO_4 root in its unique crystallographic structure. The redox potential of LiFePO_4 vs. Li is 3.4 V which is much higher compared to NASICON framework compounds,⁷ e.g. 2.8 V for $\text{Li}_3\text{Fe}_2(\text{PO}_4)_3$ and 2.75 V for $\text{Li}_2\text{FeTi}(\text{PO}_4)_3$. The excellent thermal stability^{7,31} of $\text{LiFePO}_4/\text{FePO}_4$ is a consequence of strong covalent P-O bonds. The preservation of the olivine host framework improves the stability of the material during cycling, and no loss of oxygen during charge-discharge process fulfills safety requirements for lithium batteries. The similarity of the crystallographic structures of LiFePO_4 and FePO_4 can effectively avoid capacity degradation usually occurring due to volumetric changes upon charging and discharging. However, such a polyanion structure can also lead to some problems for this material. One of the main drawbacks of LiFePO_4 is its poor electronic conductivity,³² as the non-continuous FeO_6 octahedra are separated by PO_4 tetrahedrons in the LiFePO_4 structure.³³ Moreover, because of one-dimensional curved trajectory for lithium migration along the [010] channel,³⁴ defects or impurities can easily block the one-dimensional lithium transport pathway, hindering the electrochemical performance of LiFePO_4 .

Further development of LiFePO_4 is going mainly in two directions:³⁵ one direction is to improve the electrochemical performance of LiFePO_4 , e.g. capacity, rate performance, and cycling stability, in order to satisfy the requirements of portable electronic devices and electric vehicles; the other direction lies in fundamental understanding of LiFePO_4 performance, such as size effects on lithium storage, phase transition mechanism, and defect chemistry.

In order to improve the electrochemical performance, intrinsically sluggish mass and charge transport³⁶⁻⁴⁰ in LiFePO_4 should be overcome. The lithium diffusion coefficient has been measured by different techniques such as galvanostatic intermittent titration technique (GITT)⁴¹ and electrochemical impedance spectroscopy (EIS),⁴² and a large range of values have been obtained, e.g. from 10^{-16} to 10^{-13} cm^2/s .³⁰

In our group, a systematic investigation of electronic and ionic conductivity as well as chemical diffusivity of lithium for different crystallographic orientations in big LiFePO_4 single crystals as a function of temperature has been conducted.^{32,43} Precise determination of the chemical diffusion coefficient for LiFePO_4 yielded extrapolated values of 10^{-12} cm^2/s at room temperature, which is much lower than that of LiCoO_2 (5×10^{-9} cm^2/s).³⁰ In general, there are mainly three methods available to overcome the slow diffusion issue, namely second phase effects, size reduction and defect regulation.

As regards the first issue, conductive surface coating on the LiFePO_4 mainly increases the electronic conductivity of the material, and the coating with Cu, Ag, conductive polymers and carbon has been applied until now.^{44,45} Carbon coating of LiFePO_4 was first suggested by Armand et al.,⁴⁶ who demonstrated that LiFePO_4 with carbon coating can achieve almost theoretical capacity. Afterwards, there have been numerous investigations on carbon coating approach, because carbon is of low cost, exhibits high conductivity, with low concentrations (0.5~2wt%)⁴⁴ needed, is simple to be introduced *in-situ* or *ex-situ*, and is highly chemically stable in a battery. Different types of carbonaceous organic compounds, e.g. sucrose,¹⁷ glucose,⁴⁷ polymers,⁴⁸ and carbon-containing precursors⁴⁹ can be used as carbon sources, using different synthesis approaches. It is very important to reduce the amount of carbon, to achieve a homogeneous carbon distribution and to improve conductivity of carbon, in order for such optimized materials to be applied in the commercial LiFePO_4 batteries.^{50,51} Compared to carbon coating, coating with conductive metal particles can also increase the electronic conductivity. However, it is difficult to form a uniform metal dispersion on the surface of LiFePO_4 , and metals are not stable and compatible in practical composite electrode.⁴⁴ High cost of metal additives should be considered as well. Conductive polymers, e.g. PPy, PANI and PEDOT cannot only increase electronic conductivity of the final composite, but also serve as a binder, being themselves electrochemical active, which can contribute to extra capacity.⁴⁰ A beneficial ion-conducting polyphosphate glass coating the surface of LiFePO_4 is reported by Ceder's group,⁵² such optimized networks can provide both high electronic (carbon)

and ionic (polyphosphate) conductivities for the final composite. On the other hand, the incomplete and non-uniform carbon layer will lead to polarization.⁵³ In our group, we tried to repair this incomplete network by using RuO₂, which has high electronic conductivity and lithium permeation, and good surface-surface interaction with LiFePO₄ and carbon. As a result, a much improved rate performance with less polarization was achieved.⁵⁴ Other metal oxides have also been investigated for modification of the LiFePO₄ surface, such as V₂O₃, CeO₂, ZrO₂, TiO₂.^{55, 56}

Decreasing the particle size is yet another method to improve the electronic and ionic transport properties of LiFePO₄. According to the diffusion formula $t = L^2/2D$ (where t is the diffusion time, L is the diffusion distance, and D is the diffusion coefficient), decreasing the particle size can significantly shorten the diffusion time of Li in LiFePO₄, resulting in a greatly enhanced power performance. However, nanometer-sized LiFePO₄ often suffers from low tap density and poor cycling performance due to undesirable reactions arising from its higher surface area.^{31, 57} In principle, low temperature routes are most commonly used to prepare nanosized tailored particles, such as hydro(solvo)thermal synthesis, ionothermal and low temperature ceramic routes. On the other hand, using low temperature methods, it is difficult to obtain the required highly crystalline materials, not to speak of effective conductivity of carbon coating. However, some recent reports argue that the specific capacity of LiFePO₄ has no clear dependence on the particle size in the range of 50-400nm.^{44, 58} From theoretical calculations⁵⁹ and experimental measurements,³² ionic and electronic transport along b -direction and c -direction is much faster compared to a -direction in LiFePO₄, and rapid lithium diffusion along b -axis is expected. As a result, to achieve ideal morphology of LiFePO₄, e.g. morphology with short b directions or short b and c directions, is crucial as well.

Doping of LiFePO₄ with supervalent cations (Nb⁵⁺, Ti⁴⁺, W⁶⁺) was firstly reported by Chiang's group⁶⁰ and electronic conductivity of LiFePO₄ was increased by 8 orders of magnitude to 10⁻² S/cm, which is comparable to that of LiCoO₂ and LiMn₂O₄. Following this work, many different cations, e.g. V⁵⁺, Ti⁴⁺, Cr³⁺, Al³⁺, Nb⁵⁺, Zn²⁺, Mg²⁺, Mo⁶⁺, La³⁺, Ga³⁺ have been investigated as dopants in the LiFePO₄, and

even multi-element doping and anion doping (e.g. F⁻, Cl⁻) were studied.³⁰ However, the origin of the increased conductivity is still under debate. Arguments against cationic doping mainly focus on the residual carbon from carbonaceous precursors⁶¹ and appearance of highly conductive Fe₂P³⁷ due to high temperature annealing in the reducing atmosphere. Atomistic simulation investigation suggests that LiFePO₄ is not tolerant to aliovalent doping on Li site or Fe sites, since it cannot yield mixed-valent Fe³⁺/Fe²⁺.⁶² Yet examples on single crystals clearly showed that donor as well as acceptor dopants can enter the lattice and vary the defect chemistry considerably.^{63, 64}

Compared to the success of LiFePO₄ in terms of electrochemical performance, deeper insight on understanding of the intrinsic properties of such cathode material is still needed. Defect chemistry of LiFePO₄, size effects on lithium storage and phase transition mechanism will be discussed in detail in this thesis.

1.3 Defect chemistry of LiFePO₄ and FePO₄

The analysis of defect chemistry of an electrode material is a powerful tool to achieve deeper understanding of material's properties. To get knowledge about the intrinsic transport properties, the defect chemistry of LiFePO₄ and heterosite FePO₄ was investigated in detail both experimentally^{32, 43} and by theoretical modeling.³⁴ The investigation on the variation of charge carrier concentration as a function of external thermodynamic parameters such as temperature, lithium activity and dopant concentration, allows not only to obtain conductivity and diffusion coefficient values, but also to conduct rational material optimization.²² Figure 1.4 demonstrates the charge carrier concentration as function of dopant concentration (both donor and acceptor) for LiFePO₄ and its counter-part FePO₄.

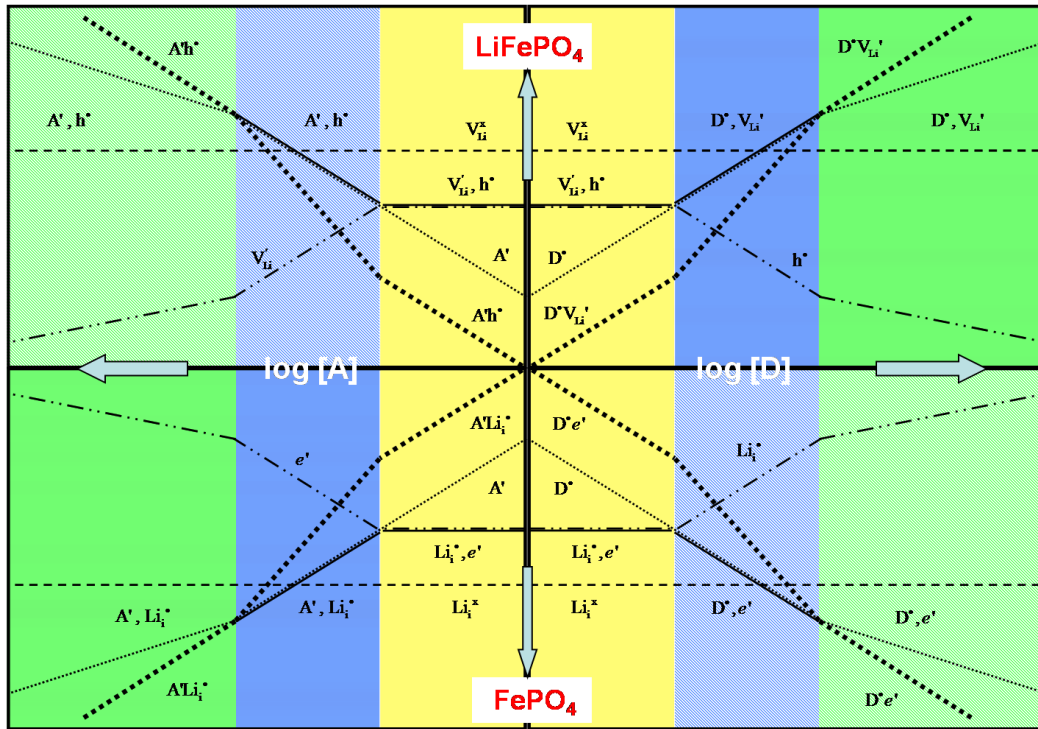


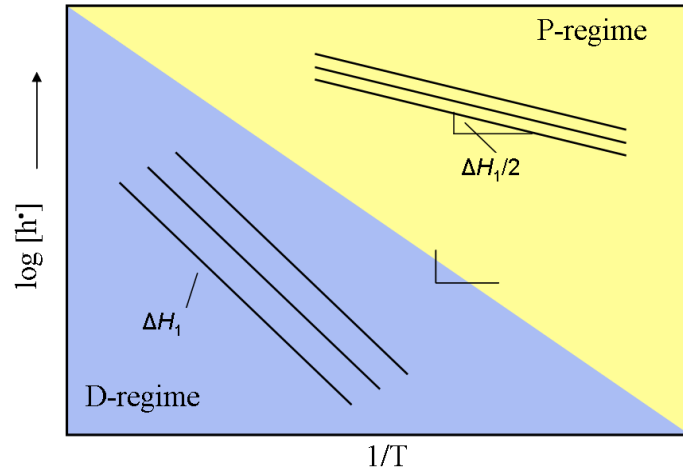
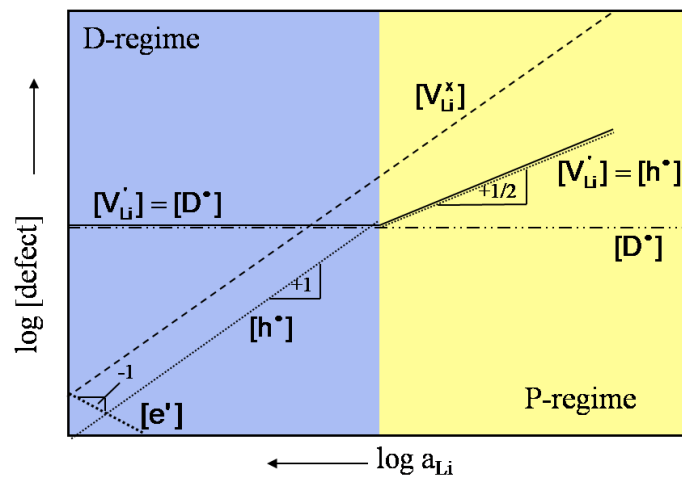
Figure 1.4 The charge carrier concentration as function of dopant concentration (both donor and acceptor) for LiFePO_4 and heterosite FePO_4 .⁶⁵

Transport properties and defect chemistry of LiFePO_4 were systematically investigated using LiFePO_4 single crystal grown by optical floating zone technique.⁴³ Ionic and electronic conductivities as well as chemical diffusion for Li (D_{Li}^δ) in LiFePO_4 single crystal was studied as a function of crystallographic orientation over an extended temperature range by using impedance and direct current (DC) polarization measurements with electronically as well as ionically blocking cells. Several important conclusions are derived. The activation energies for electronic and ionic conductivities are located in the range of 0.55-0.59 eV and of 0.62-0.74 eV, depending on the crystal orientation.²² Anisotropy of two dimensional (b , c plane) electronic and ionic conductivities as well as anisotropic chemical diffusion of Li are observed. In addition, the electronic conductivity dominates in LiFePO_4 , as the ionic conductivities along all the directions (a , b , c) are much smaller compared to the electronic conductivities. On the other hand, theoretical calculation predicts that lithium transport along b -axis (along the LiO_6 octahedral chains) is predominant,

since the energies barriers along the b direction is much lower.⁵⁹ That such a b -axis preference is not seen in the experimental results obtained from single crystal LiFePO_4 measurement can be explained by anti-site defects (Fe_{Li}^\bullet) which block lithium migration pathway along b direction.

From the energetical point of view, vacancies and interstitials in the Fe- or O-sublattices are unfavorable³⁴ in LiFePO_4 . Oppositely, anti site defects are found to be easily formed. The appearance of anti site defects (Fe_{Li}^\bullet) localize the nominal pure LiFePO_4 in the D-regime (donor doped regime). For the LiFePO_4 , the majority of charge carriers are lithium vacancies (V_{Li}') and holes (h^\bullet), since the formation energy is very low for V_{Li}' and low pressure of Li in the surrounding, which is confirmed by measurements on single crystalline and polycrystalline LiFePO_4 . As a result, p-type conductivity has been found for LiFePO_4 .

Transport properties of LiFePO_4 as function of lithium activity were investigated by annealing the polycrystalline LiFePO_4 at different temperatures.⁶⁶ Upon the annealing process, the activation energy initially stays constant around 0.65 eV and finally decreases to almost half of its value (0.30 eV), which can be explained by a transition from D-regime to P-regime, as showed in Figure 1.5. In the D-regime, lithium vacancies are compensated by either native anti-site defects or by extrinsic donor doped materials (will be discussed later), and hole concentration will decide the final conductivity behavior. This region can be observed at high lithium activity or in highly donor doped LiFePO_4 . In the P-regime, lithium vacancies are compensated by electronic defects, which can be found at low lithium activity (high lithium deficiency). Figure 1.6 shows the dependency of defect concentrations on lithium activity in the Brouwer diagram, showing the transition of the two defect regimes (D-regime and P-regime).


 Figure 1.5 Hole concentration vs. temperature for frozen-in Li-stoichiometry.²²

 Figure 1.6 Defect concentrations as a function of lithium activity.²²

Single crystals of Al-doped LiFePO_4 (1% Al)^{63, 67} and Si-doped LiFePO_4 (1% Si)⁶⁴ were also successfully grown by an optical floating zone technique. The transport properties along b - and c - directions are similar but significantly different from the a -directions, which shows lower values. Compared to pure LiFePO_4 , a donor effect was observed. Donor doping results in enhancement of ionic conductivity (lithium vacancies), while the electronic conductivity (holes) is decreased. When the doping level is high enough, the concentration of lithium vacancies is fixed by the concentration of doping level, and the material is in the D-regime. Unlike pure LiFePO_4 , not only the association of holes with lithium vacancies but also purely ionic association plays a crucial role, as shown in the Figure 1.7.

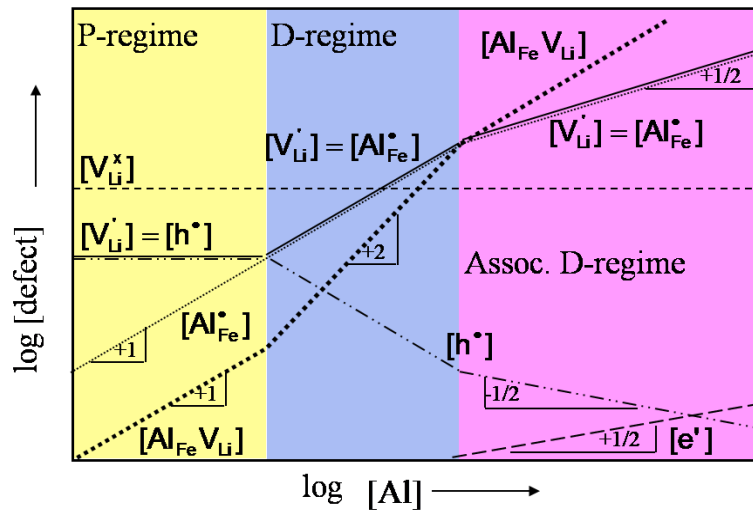


Figure 1.7 Defect concentrations vs. donor content including strong association.⁶⁷

The transport properties and defect chemistry of orthorhombic FePO_4 (heterosite), the lithium-poor part of the $\text{LiFePO}_4/\text{FePO}_4$ redox couple were investigated using polycrystalline FePO_4 .⁶⁸ The FePO_4 obtained by chemical delithiation of LiFePO_4 shows a predominant electronic conductivity, which is similar to LiFePO_4 . A residual lithium content of 0.03 wt% was found and has to be considered as lithium interstitials in the FePO_4 ground structure. As a result, the major charge carriers are lithium interstitials (Li_i^\bullet) and electrons (e') in FePO_4 . Compensation by electrons induces n-type conductivity, which is confirmed by the $P(\text{O}_2)$ dependence of the electronic conductivity (Figure 1.8). The $P(\text{O}_2)$ dependency can be attributed to the formation of an oxidic surface composition (Li_2O_2) leading to bulk depletion of lithium, rather than to filling of oxygen vacancies.

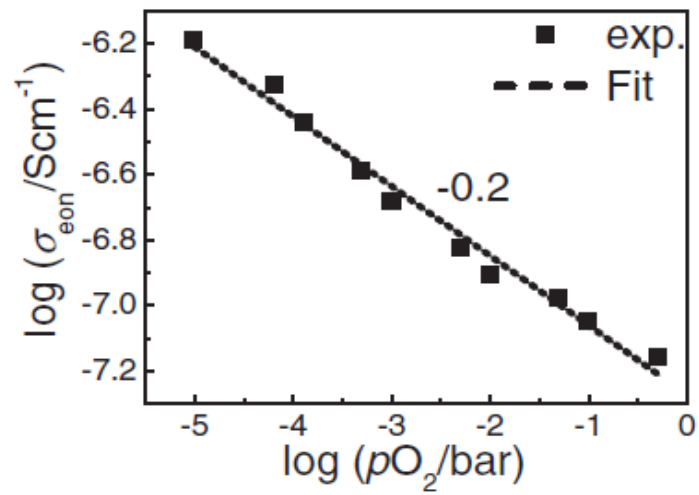


Figure 1.8 Oxygen partial pressure dependence of the electronic conductivity of heterosite FePO₄ at T=175 °C.⁶⁸

Chapter 2

Instrumental techniques

2.1 Structural characterization

2.1.1 X-ray diffraction (XRD)

X-ray diffraction (XRD) is an effective nondestructive analytical method for characterization of crystalline materials, providing the information on chemical composition and crystallographic structure of both natural and manufactured materials. The theory of XRD is based on the well known Bragg's law:⁶⁹

$$2d_{hkl} \sin \theta = n\lambda, \quad (2-1)$$

where d_{hkl} is the interplanar spacing in specific crystalline lattice, θ is the angle between incoming (outgoing) X-ray beam and lattice plane, and n is a natural number representing the order of the diffraction peak as shown in Figure 2.1.

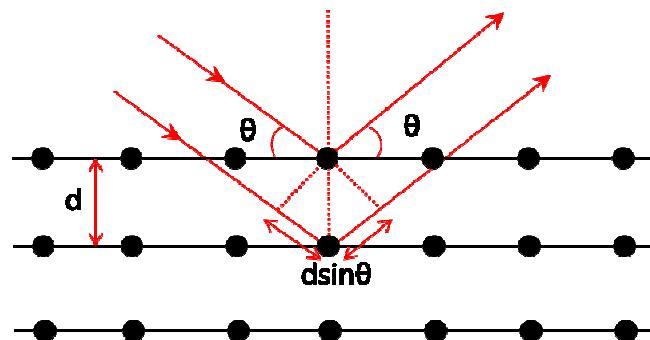


Figure 2.1 Schematic representation of the geometry considered for derivation of the Bragg condition.

The peak position, intensity and shape in XRD pattern provide abundant information on the crystal structure of the material, e.g. unit cell parameters, atomic parameters, crystallinity, disorder and defects. The peaks are characteristic for certain material and the crystalline orientation of the grains in a polycrystalline layer. The average grain size, d , can be estimated from the Scherrer formula⁷⁰

$$d=K\lambda/\beta_{1/2}\cos\theta, \quad (2-2)$$

Where K is the shape factor, λ is the wavelength of X-ray, $\beta_{1/2}$ is the corrected width of diffraction peak at half-height and θ is Bragg diffraction angle.

In this work, all the samples were characterized by XRD using Cu-K $_{\alpha}$ radiation in Phillips PW 3020 diffractometer and the diffraction data collected at 0.02° step width over a 2θ range from 10° to 90°. XRD measurements were carried out with short run (1 sec/step) to check the crystal structure and long run (15 sec/step) to check for minor impurities. LiFePO $_4$ particle size (d) was calculated using whole powder pattern refinement by Topas4 software.

2.2 Electron microscopy

2.2.1 Scanning electron microscopy (SEM)

The scanning electron microscope (SEM) is a powerful tool to investigate the morphology of the samples, using a focused high-energy electron beam to generate a variety of signals at the surface of solid specimens. The signals derived from electron-sample interactions provide information on the sample such as external morphology, chemical composition, and crystalline structure.

The kinetic energy from accelerated electrons in SEM is dissipated as a variety of signals produced by electron-sample interactions. These signals are generated from secondary electrons, backscattered electrons, diffracted backscattered electrons, photons, visible light, and heat. Secondary electrons and backscattered electrons are commonly used for imaging samples. Secondary electrons are used for showing morphology and topography on samples while backscattered electrons are explored for illustrating contrasts in composition in multiphase samples. Characteristic X-rays produced for each element in a sample which is excited by the electron beam can be used for compositional analysis.

A typical SEM instrument includes electron column, sample chamber, energy-dispersive (EDS) detector, electronics console, and visual display monitors.

In this work, the morphology of the obtained samples was investigated using a JEOL 6300F field-emission scanning electron microscope (JEOL, Tokyo, Japan) operated at 15 keV.

2.2.2 Transmission electron microscopy (TEM)

Transmission electron microscopy (TEM) is a unique and versatile characterization tool because it can provide not only a real space atomic-resolution lattice images for the nanocrystal and its surface, but also chemical information at a spatial resolution of 1 nm or better, hence allowing direct identification of the chemistry of a single nanocrystal. A simplified ray diagram of a TEM consists of an electron source, condenser lens with aperture, specimen, objective lens with aperture, projector lens and fluorescent screen.

TEM has three functions, imaging, spectroscopy and diffraction. By TEM images, we can obtain the information on the size, shape and texture of nanocrystals. For better imaging, high-resolution transmission electron microscope (HR-TEM) has to be applied, since it is capable of giving resolutions on the picometer scale due to the highly stable electron acceleration voltage and operability on the fixed current. The lattice fringes (in HR-TEM), obtained by interference between the transmitted beam and the diffracted beam, can provide information on the periodicity of the crystal. Electron diffraction (ED) is a TEM mode which allows users to determine the atomic arrangement of crystals. When combined with other functions such as EDS, it can help indentifying unknown crystals and determining the *d*-spacing of newly described crystals. The ED pattern is completely dependent on the *d*-spacing and composition of the crystal that is being investigated. An ED of a single crystal will result in a series of diffraction spots arranged in concentric rings around the central bright spot which is comprised of transmitted electrons. While for polycrystals, some of which are oriented at the Bragg's angle while others are not, an ED pattern with well defined concentric rings, but not spots, will appear. As to amorphous structure (i.e. no crystalline formation), only a central bright spot comprised of transmitted electrons and a single ring of randomly forward scattered electrons in ED pattern is

observed.

In this work, HRTEM and SAED analysis were performed using a JEOL 2010F transmission electron microscope operated at 200 keV. The interpretable resolution defined by the contrast transfer function of the objective lens is 0.19 nm. EDX analysis was carried out using an Oxford system attached to a JEOL 2010F microscope.

2.2.3 Scanning transmission electron microscopy (STEM) and annular-bright-field (ABF)

In order to achieve better resolution, scanning transmission electron microscopy (STEM) with annular bright field (ABF) imaging was developed,⁷¹ which can directly image lithium at atomic resolution. A novel imaging mode for STEM with an annular detector spanning a range within the illumination cone of the focused electron beam was designed⁷². It was demonstrated that the resultant images enable one to determine the location of columns containing light elements. This imaging mode is the so called annular bright field (ABF) imaging, different from the well-established high angle annular dark field (HAADF) imaging mode, in which the collection range of the annular detector is outside of the illumination cone. A schematic of the imaging geometry of STEM-ABF is given in Figure 2.2.

Because of the relatively poor scattering ability of light atoms, *e.g.* O and Li, they can not be revealed by the HAADF image. However, in the ABF collection geometry at lower collection angles, namely from 11 to 20 mrad, the light elements can be effectively revealed, because the ABF contrast tends to minimize the variance of the atomic number by following a $Z^{1/3}$ dependency⁷³. On the other hand, compared to normal bright-field acquisition including the signals from the optical-axis, which corresponds mainly to the phase contrast conventional high-resolution TEM conditions from the reciprocity theorem, dynamic effects here are annihilated to a great extent. As a result, the ABF image can withstand a larger thickness of a specimen without an occurrence of the contrast reversal, which makes it a robust imaging geometry in particular for light atoms.

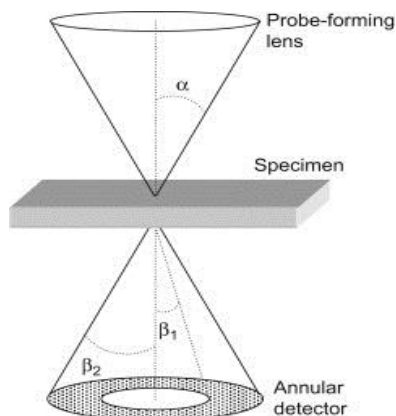


Figure 2.2. Schematic of the general imaging geometry of STEM-ABF. The probe-forming aperture semiangle, α , and the diffraction plane annular detector inner and outer angles, β_1 and β_2 , are the main parameters to vary. As drawn, $\alpha = \beta_2$. This is not essential, though the appellation of “bright field” imaging will only strictly hold if $\beta_2 \leq \alpha$.⁷²

Schematic of the ABF imaging conditions used in this work are shown in the Figure 2.2, working with a convergent beam and an annular-shaped bright-field detector. A fine probe with a spot size less than 1 angstrom scans across the specimen, and the annular detector defines a collection semi-angle at given camera lengths. The whole layout is performed by a JEOL 2100F (JEOL, Tokyo, Japan) microscope operated at 200 keV with a CEOS hexapole Cs corrector (CEOS GmbH, Heidelberg, Germany) to cope with the probe-forming objective spherical aberration. The experimental illumination semiangle was fixed to 20mrad for both high-angle annular-dark-field (HAADF) and ABF collection conditions.

2.3 Electrochemical characterization

2.3.1 Cyclic voltammetry (CV)

Cyclic voltammetry (CV) is one of the most versatile electroanalytical techniques to investigate electroactive species. CV is usually the first experiment to perform in an electrochemical study, because it allows rapid observation of the redox

behavior over a wide potential range.

In cyclic voltammetry, the electrode potential ramps linearly versus time with a triangular waveform, which is characterized by a given scan rate (V/s). The current (I) measured between the working electrode and the counter electrode is plotted versus the voltage (E) applied between the reference electrode and the working electrode to give the cyclic voltammogram trace.

Much thermodynamic and dynamic information about the redox potential and electrochemical reaction rates of electroactive species can be obtained by CV. If the electronic transfer at the surface is fast and the current is limited by the diffusion of species to the electrode surface, then the current peak will be proportional to the square root of the scan rate. If different scan rates are applied and linear relation of I_p vs $v^{1/2}$ is obtained, then the apparent chemical diffusion coefficient can be estimated by Randles-Sevcik equation⁷⁴ as follows:

$$I_p = KnFAC(nFvD / RT)^{1/2}, \quad (2-3)$$

where I_p is current maximum (A), K is constant, n is number of electrons transferred in the redox event, A is electrode area (cm^2), F is Faraday constant (C/mol), D is diffusion coefficient (cm^2/s), C is concentration (mol/cm^3) and v is scan rate (V/s).

2.3.2 Galvanostatic intermittent titration techniques (GITT)

The voltage-composition relation for the electrode materials of batteries can be determined either in a current controlled mode referred to as galvanostatic intermittent titration techniques (GITT) or in a potential controlled mode as potentiostatic intermittent titration technique (PITT, next section). GITT is applied which combines both transient and steady-state measurements to obtain kinetic properties of mixed conductors, as well as thermodynamic parameters.

GITT carries on successive charge (discharge) increments (decrements) by applying a small constant current for a given time, then switching to open circuit for determining the corresponding equilibrium potential. The procedure will be repeated until the voltage reaches the pre-set values. The time dependence of the potential can

give information on the kinetics of the process. From thermodynamic point of view, GITT is an effective method to measure the open circuit values for the electrode as function of different lithium content.

If one-dimensional diffusion in a solid solution electrode is considered (assumption made accordingly), the lithium ion diffusion coefficient for the materials with single phase lithium intercalation regime can be calculated by Fick's law through the following equation⁷⁵

$$D_{GITT} = \frac{4}{\pi} \left(\frac{IV_M}{z_A FS} \right) \left[\frac{dE(x)/dx}{dE(t)/d\sqrt{t}} \right]^2 (t \ll L^2 / D_{GITT}), \quad (2-4)$$

where D is diffusion coefficient (cm²/s), L (cm) is the characteristic length of electrode materials, F (C/mol) is the Faraday constant, z_A is the charge number of electroactive species, S (cm²) is the contact area between the electrode and electrolyte, I (A) is the applied current, and V_M (cm³/mol) is the molar volume of the electrode material. The value of $dE(t)/dt^{1/2}$ can be calculated from a plot of the voltage versus the square root of the time during constant current step, and $dE(x)/dx$ can be obtained by plotting of the equilibrium electrode voltage as function of composition after each current pulse.

As for phase transition electrodes, GITT has to be modified in order to calculate the lithium ion diffusion coefficient, since in the two-phase region, lithium ions are transported through both movement of an interphase boundary and diffusion in the electrode.

In this work, GITT is performed as follows: the 1/20 C current was used for charging and discharging the samples for 1 hour followed by a 10-30 hours waiting time leading to the relaxation to equilibrium state as a function of different lithium contents.

2.3.3 Potentiostatic intermittent titration technique (PITT)

Potentiostatic intermittent titration technique (PITT) is a reckoned useful method, which can provide thermodynamic, kinetic and phase transformation information.^{76,77} PITT is performed in the following steps: 1) the electrochemical cell is initially in

equilibrium or close to equilibrium state with a potential of V_{initial} ; 2) the small potential step dV slightly higher or lower than the V_{initial} is applied, and the current is continuously monitored until it decays to a pre-set minimum value, I_{min} ; 3) when $I = I_{\text{min}}$, the cell voltage is stepped by dV again; 4) the steps continue until the cell voltage reaches a preset maximum value V_{max} (V_{min}), then the direction of voltage goes back.

During each step, the current can be integrated to calculate the differential capacity, which can be used for effective characterization of order/disorder and structural ordering phenomenon in intercalation systems. In addition, the time-dependent charge or current can be monitored on each step in order to extract kinetic information. For instance, the decay of the current in each step is proportional to $t^{-\frac{1}{2}}$ for linear diffusion in a semi-infinite system. As a result, the apparent chemical diffusion coefficient for the electrode can be calculated at each voltage decrement or increment step by applying standard Cottrell equation. The diffusion coefficient of ions in solid solution electrodes can be estimated based on Fick's law using the following equation⁴¹

$$D_{\text{PITT}} = -\frac{d \ln I(t)}{dt} \frac{4L^2}{\pi^2} (t \gg L^2 / D_{\text{PITT}}), \quad (2-5)$$

where L (cm) is the characteristic length of the electrode material and $I(t)$ (A) is the current measured during the constant voltage step. While for the phase transformation materials in the two phase region, PITT is not a reliable method to calculate the diffusion coefficient since it based on the Fick's law, and need to be modified.

PITT is also an effective tool to investigate the lithium intercalation regime, e.g. single phase regime and two phase regime, by looking at the difference of current relaxation time scales and shape of the current curves $I(t)$. When transformation limited by nucleation and growth occurs, a local maximum should appear in the $I(t)$ curves; while in a single-phase diffusion model, there is no bell-shaped current response.

In this work, PITT was performed as follows: a "staircase" voltage profile with a 5 mV voltage increment / decrement (each titration was stopped when the current

reached around $\sim C/20$) was applied, and the response of current vs time was recorded at each constant potential.

2.4 Instrument details

Differential Scanning Calorimetry (DSC)

DSC measurement was carried out on a STA 449C instrument (Netzsch Co., Germany) under nitrogen atmosphere. The measurements were conducted from 20°C to 820°C at a rate of 10°C min⁻¹. The phase transition temperature (onset temperature of the endothermic peak) was determined from the DSC thermogram.

Inductively Coupled Plasma Analysis Coupled with Atomic Emission Spectroscopy (ICP-AES)

ICP-AES (spectro Cirrus 2000) analysis was carried out to determine the elemental composition of the samples. The material was dissolved in acidic solution and emission spectra were obtained by introducing the solutions into argon plasma (6000°C). Obtained emission spectra were fed into a linear plot (amount of element vs. intensity of peak) obtained from other standard solutions. This reverse analysis yields the amount of the element (based on the intensity of emission spectra specific for the element) present in the sample.

Electrochemical cell assembly

LiFePO₄ (70 wt. %), carbon black (20 wt. %, Super-P, Timcal), and poly(vinylidene fluoride) binder (10 wt. %, Aldrich) in N-methylpyrrolidone were mixed into a homogeneous slurry. The obtained slurry was pasted on Al foil using the Doctor Blade technique, followed by drying in a vacuum oven for 12 hours at 80 °C. Electrochemical test cells (Swagelok-type) were assembled in an argon-filled glove box (O₂ ≤ 0.1 ppm, H₂O ≤ 3 ppm) with the coated Al disk as working electrode, lithium metal foil as the counter/reference electrode, and 1 M solution of LiPF₆ in a 1:1 vol/vol mixture of ethylene carbonate and diethyl carbonate as the electrolyte (Novolyte technologies). Celgard 2400 film was used as separator.

Electrochemical battery test

The batteries were charged and discharged galvanostatically in the fixed voltage

window between 2.5 V to 4.3 V on an Arbin MSTAT battery tester at room temperature (charge and discharge rate respectively the same). A rate of nC denotes an intercalation/deintercalation of 1 Li in 1/nh.

Fourier transform infrared spectroscopy (FTIR)

FTIR spectra were collected by using Bruker IFS 66 spectrometer.

Cyclic voltammetry (CV)

Cyclic voltammetry was carried out with a Voltalab system (D21V032, Radiometer Analytical SAS, France) on Swagelok-type cells.

Chapter 3

Synthesis and electrochemical performance of LiFePO₄

3.1 Introduction

In order to achieve morphology controlled as well as size controlled synthesis of LiFePO₄, it is necessary to understand different synthesis approaches for the preparation of LiFePO₄. Studies focusing on LiFePO₄ synthesis were numerous in the last decade. In general, the synthetic routes can be divided into two types: solid state reaction and soft chemistry approach. Mechanical alloying process and carbothermal reduction can be subsumed under the former, while the latter includes sol-gel, hydro(solvo)thermal, polyol, and coprecipitation methods.

It is a solid state reaction that has been used firstly for preparing LiFePO₄.⁷ Here, stoichiometric amounts of the iron source, a lithium salt and a phosphate are mixed first, followed by a decomposition process at a chosen temperature (normally 600-800 °C) and time (several hours to several days).³⁰ Such a long time sintering at high temperature is needed to obtain a pure olivine phase. The decomposition and sintering process can be carried out in one step or in two separated steps. If a mechanical alloying method (ball milling) is applied, the sintering time can be significantly reduced,⁷⁸ and homogeneous particles of smaller sizes can be obtained. If a Fe(III) precursor is chosen, either reductive gas is needed or carbothermal reduction has to be used to reduce the Fe³⁺ to Fe²⁺. Generally, for the carbothermal reduction method, very high temperature is necessary to get LiFePO₄/C composite, which, however, leads to undesired impurities,³⁰ e.g. phosphide, Fe₂O₃ and Li₃Fe₂(PO₄)₃ and particle agglomeration. The carbon coating process can be applied during or after solid state sintering by addition of a suitable carbonaceous precursor. The final electronic conductivity of the carbon coating is dependent not only on the sintering temperature but also on the type of the precursor used. At the moment, solid state reaction is the most common method used for the large-scale commercial production of LiFePO₄.

Nevertheless, this method leads to uncontrollable particle growth and agglomeration as well as large particles with irregular morphology. This was the incentive to explore more easily controllable and more economical synthetic approaches.

Compared to the solid state reaction, the soft chemistry method (solution chemistry approach) is a powerful method which enables tailoring of the particle size and the morphology of LiFePO₄. The soft chemistry method starts from a liquid solution containing precursor salts, in which intimate mixing of the starting ingredients at the atomic level is ensured, leading to smaller particles of high purity. A post heat treatment at high temperature is often necessary to obtain well crystalline LiFePO₄.

A hydrothermal method for preparation of LiFePO₄ was firstly carried out by Whittingham's group,¹⁷ followed by modified hydrothermal synthesis developed by other groups to further optimize morphology and improve electrochemical performance.⁷⁹ Usually, LiFePO₄ prepared by hydrothermal route requires a post-heat treatment at high temperature, e.g. 700 °C, in order to eliminate the Fe-Li cation disorder,⁸ which can block lithium transport channel and leads to poor electrochemical performance. Addition of some reducing agents,⁸⁰ for example, ascorbic acid and sugar, as well as addition of some organic surfactants such as CTAB (hexadecyl- trimethylammonium bromide) have also been investigated in hydrothermal synthesis.⁸¹ The former can prevent the formation of surface ferric film and the latter can result in LiFePO₄ with higher surface areas. The solvothermal process is similar to the hydrothermal method, whereby water is replaced with organic solvents such as ethylene glycol, tetraethyleneglycol, benzyl alcohol, polyethyleneglycol-water mixtures and different types of room temperature ionic liquids.⁷⁹ The polyol process is a type of solvothermal process, which uses polyol, e.g. ethylene glycol, diethylene glycol and tetraethyleneglycol as solvent. However, polyol medium serves not only as a solvent, but also as a reducing agent and stabilizer to prevent the particle growth and agglomeration.⁸²⁻⁸⁴ The sol-gel method has also been applied for preparation of LiFePO₄ and optimization of the distribution of carbon⁵⁰ in the final LiFePO₄/carbon composite as well as porosity.⁵¹ Dominko et al. used Fe(III)

citrate as a precursor to prepare carbon coated porous LiFePO₄/carbon composite with high tap density (1.9 g cm⁻³)¹⁶ and excellent rate performance.

Let us now discuss the LiFePO₄ morphology required for achieving satisfying electrochemical performance. First of all, LiFePO₄ should be highly crystalline with unblocked lithium transported channels. Secondly, the particle size should be small enough enabling short diffusion pathways for both ionic and electronic transport. Thirdly, a uniform and thin conductive carbon layers should be formed on the particle surface to ensure that electrons can be transported isotropically (from all directions) and ions can penetrate freely through the coating layer.

In this chapter, carbon coated single-crystalline LiFePO₄ nanowires prepared by electrospinning technique will be discussed in detail. Additionally, controlled synthesis of LiFePO₄ nanoparticles by surfactant-assisted polyol method, as well as precipitation method for obtaining amorphous FePO₄ and LiFePO₄ will be shown. The related electrochemical performance of LiFePO₄ with different morphologies and sizes will be discussed.

3.2 Electrospinning of carbon-coated single crystalline LiFePO₄ nanowires

3.2.1 Introduction

Numerous previous work has been done with respect to developing synthetic methods especially solution methods (e.g. sol-gel,¹⁶ hydro(solvo)thermal,⁸⁵ polyol,⁸² coprecipitation⁸⁶ methods, etc.) to prepare nano-sized LiFePO₄ of different morphologies. So far, LiFePO₄ spherical nanoparticles,⁸⁷ nanoplates,⁸⁵ nano-porous structures⁸⁸ and nanowires^{45, 89} have been successfully synthesized and exhibited improved electrochemical performance.

Among the wide range of morphologies found in electrode materials, nanowires are especially promising, as they offer a better percolation behavior compared to particles.⁵⁷ However, up to now, only a few papers report on the synthesis of LiFePO₄ nanowires. A rather tedious hard templating method was used by Lim⁸⁹ *et al.*, involving post-treatment with HF or NaOH, during which LiFePO₄ can be dissolved or even chemically react.⁸⁸ After synthesis, bundles of nanowires are obtained, where

each wire is formed by agglomeration of individual particles.⁸⁹ Another possible method is inexpensive, simple and versatile electrospinning technique usually used to obtain nanofibers⁹⁰ of a variety of materials such as polymers,⁹¹ ceramic metal oxides,⁹² or metals.⁹³ Depending on the individual experimental setup, porous, hollow, amorphous, and polycrystalline nanowires can be prepared.^{90, 92} However, single-crystalline nanowires produced by electrospinning are in general quite rare. Recently, Hosono *et al.* synthesized carbon-coated LiFePO₄ nanowires as well as triaxial LiFePO₄ nanowires with a carbon nanotube core and a carbon shell by the electrospinning method.⁹⁴ The thickness of such LiFePO₄ nanowires (500 nm up to 1 μm in diameter) constrains their performance and smaller dimensions are needed for practical use in lithium batteries. Consequently, preparation of well crystalline and thin LiFePO₄ nanowires with effective carbon coating was the first goal of this thesis.

3.2.2 Experimental

Synthesis: 0.63 g of LiH₂PO₄ (6.1 mmol, Aldrich, ≥ 99%) and 2.42 g of Fe(NO₃)₃·9H₂O (6 mmol, Aldrich, ≥ 99.99%) were dissolved in 30 ml water and 0.6 g poly(ethylene oxide) (Aldrich, M_v = 600000, CAS: 25322-68-3) were added. The resultant precursor solution was poured into a syringe connected to a blunt cannula (*d*=1.6 mm). The flow rate was *ca.* 10 μl/min and a grounded stainless steel plate was placed 15 cm below the spinneret to collect the nanowires. A high voltage of 15 kV was applied by a high voltage power supply (Model HCE35-35000, FUG DC power source, Germany). The as-collected electrospun fibers were calcined in an Al₂O₃ crucible in a tube furnace at 600 °C for 2 hours under H₂ (5 vol%)/Ar (95 vol%) atmosphere to obtain single-crystalline LiFePO₄ nanowires (heating rate 2 °C/min, cooling rate 5 °C/min). Commercial carbon-coated LiFePO₄ (particle size around 200 nm, carbon content about 1 wt%) was purchased from Advanced Lithium Electrochemistry Co., Ltd, Taiwan.

Electrochemical measurements: Single-crystalline LiFePO₄ nanowires or the commercial carbon-coated LiFePO₄ (70 (80) wt. %), carbon black (20 (10) wt. %, Super-P, Timcal), and poly(vinylidene fluoride) binder (10 wt. %, Aldrich) in

N-methylpyrrolidone were mixed into a homogeneous slurry (grinding in mortar for 10 minutes followed by magnetical stirring overnight in a closed beaker). The obtained slurry was pasted on Al foil using the Doctor Blade technique, followed by drying in a vacuum oven for 12 hours at 80 °C. Finally, round disks of 1 cm in diameter were cut, the loading of each was *ca.* 1.3 mg/cm² with an electrode thickness of around 50 μm. Electrochemical test cells (Swagelok-type) were assembled in an argon-filled glove box (O₂ ≤ 0.1 ppm, H₂O ≤ 3 ppm) with the coated Al disk as working electrode, lithium metal foil as the counter/reference electrode, and 1 M solution of LiPF₆ in a 1:1 vol/vol mixture of ethylene carbonate and diethyl carbonate as the electrolyte (Novolyte technologies). Celgard 2400 film was used as a separator. The batteries were charged and discharged galvanostatically (from 0.1 C to 10 C) in the fixed voltage window between 2.5 V to 4.3 V on an Arbin MSTAT battery tester at room temperature (charge and discharge rate respectively the same). Cyclic voltammetry was performed with Voltalab system (D21V032, Radiometer Analytical SAS, France) on Swagelok-type cells with the scan rate of 0.1mV/s.

3.2.3 Results and discussions

3.2.3.1 Morphology and formation mechanism of LiFePO₄ nanowires

Figure 3.2.1 demonstrates the schematic setup for the preparation of LiFePO₄ nanowires. First of all, an aqueous precursor solution containing LiH₂PO₄, Fe(NO₃)₃ and poly(ethylene oxide) was used to prepare a polymer nanowire with the LiFePO₄ precursor inside by electrospinning process. After that, the as-prepared polymer nanowires are sintered at high temperature (e.g. 600~800 °C) in Ar/H₂ atmosphere to obtain *in situ* carbon coated LiFePO₄ nanowires. The final morphology of LiFePO₄ is mainly determined by the first step, *i.e.* the electrospinning process.

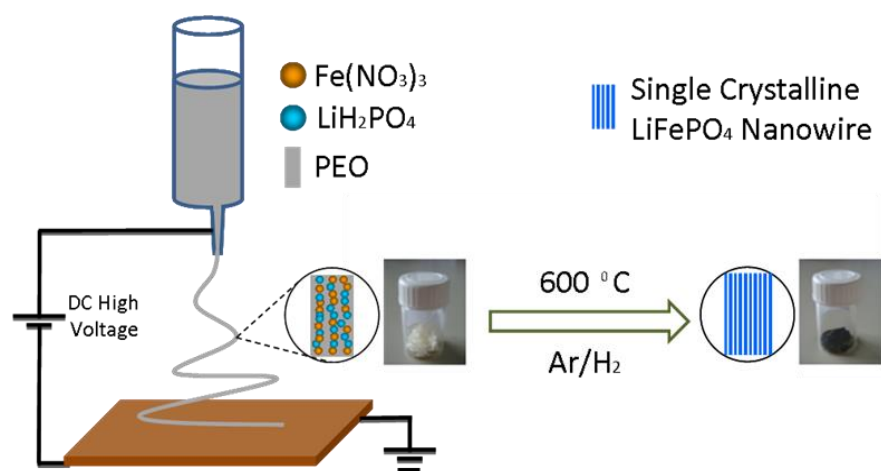


Figure 3.2.1 Schematic illustration of LiFePO₄ nanowire preparation by electrospinning process.

After electrospinning, long (several μm) and continuous polymer nanowires of fibrous morphology were obtained with thin and uniform diameters of about 100 nm. The wires are in contact with each other as shown by scanning electron microscopy (SEM) (Figure 3.2.2a). Sintering of these as-prepared nanowires at 600 °C in H₂ (5 vol%)/Ar (95 vol%) atmosphere leads to the polymer decomposition and formation of carbon-coated LiFePO₄ nanowires with a similar diameter (\sim 100 nm) (Figure. 3.2.2b). The obtained LiFePO₄ nanowires are much thinner compared to the previously reported ones.⁹⁴

X-ray diffraction (XRD) analysis reveals well crystalline single phase LiFePO₄ without detectable impurity phases (all peaks could be indexed according to ICDD card No. 01-081-1173, Figure 3.2.3). It is worth mentioning that, at high temperatures, Li evaporation often occurs and Li insufficiency results in Fe₂P₂O₇ impurity, which has been found many times in solid state synthesis of LiFePO₄. However, in this work, the in situ obtained amorphous carbon probably reduces Li losses during sintering of the material, and leads to pure and highly crystalline LiFePO₄ nanowires. However, if the sintering temperature is increased to 800 °C, the impurity Fe₂P appears.

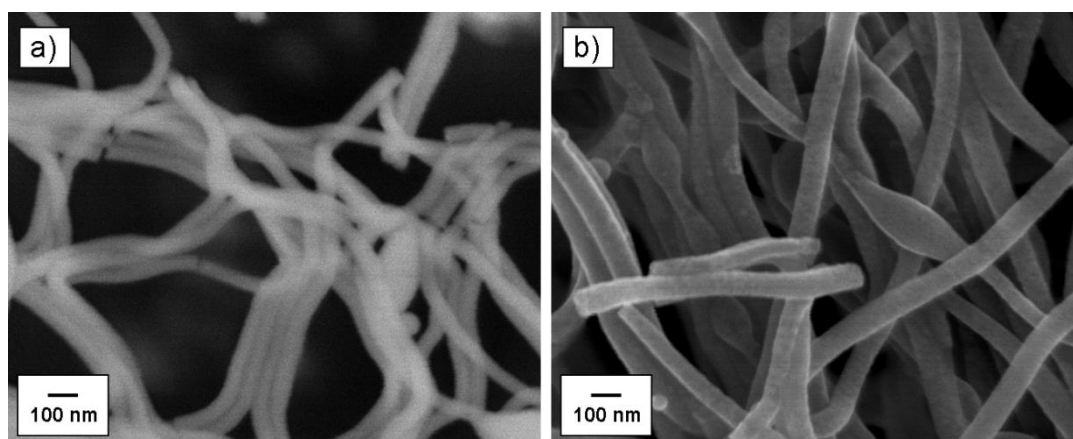


Figure 3.2.2 SEM images of a) as-prepared polymer nanowires containing LiFePO_4 precursors b) LiFePO_4 nanowires after sintering at 600 °C for 2 hours in Ar/H₂ atmosphere.

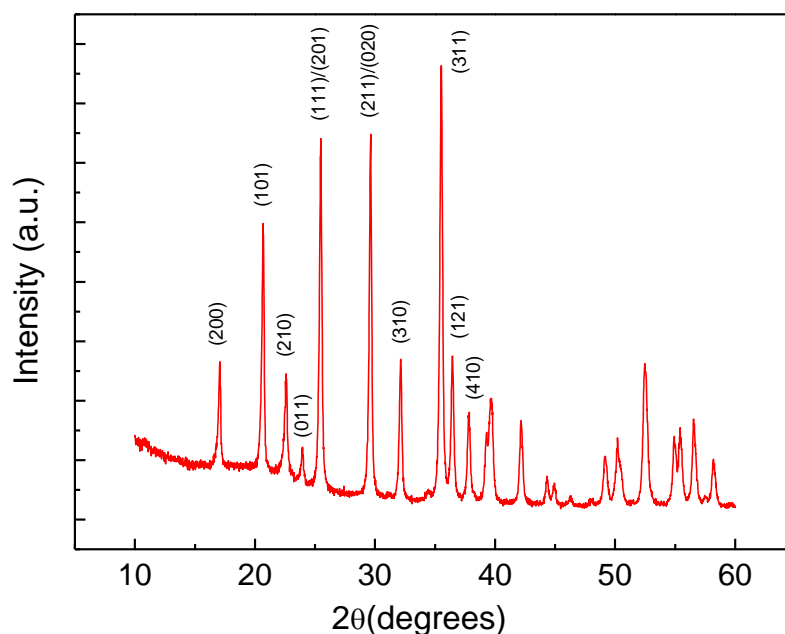


Figure 3.2.3 X-ray diffraction pattern of LiFePO_4 nanowires sintered at 600 °C for 2 hours.

Both energy-dispersive X-ray (EDX) spectroscopy (Figure 3.2.4) and transmission electron microscopy (TEM) (Figure 3.2.5b) confirm the presence of carbon in the final LiFePO_4 nanowires, the content of which amounts to 6 wt% as detected by elemental analysis.

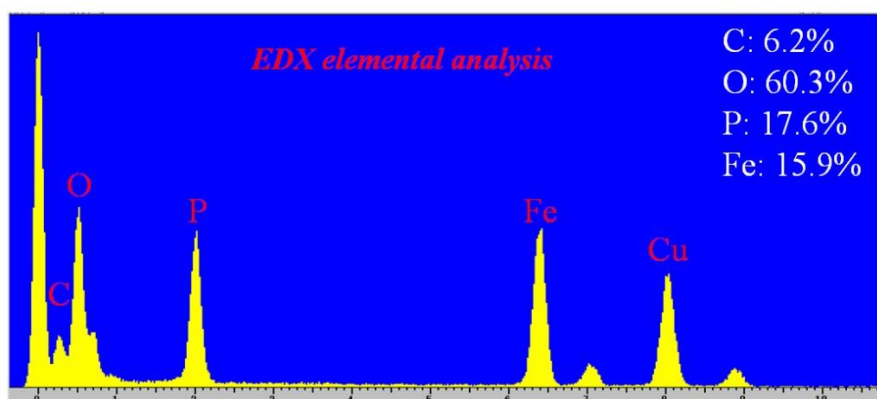


Figure 3.2.4 EDX spectrum of carbon-coated LiFePO₄ nanowires with the elemental composition given in wt%.

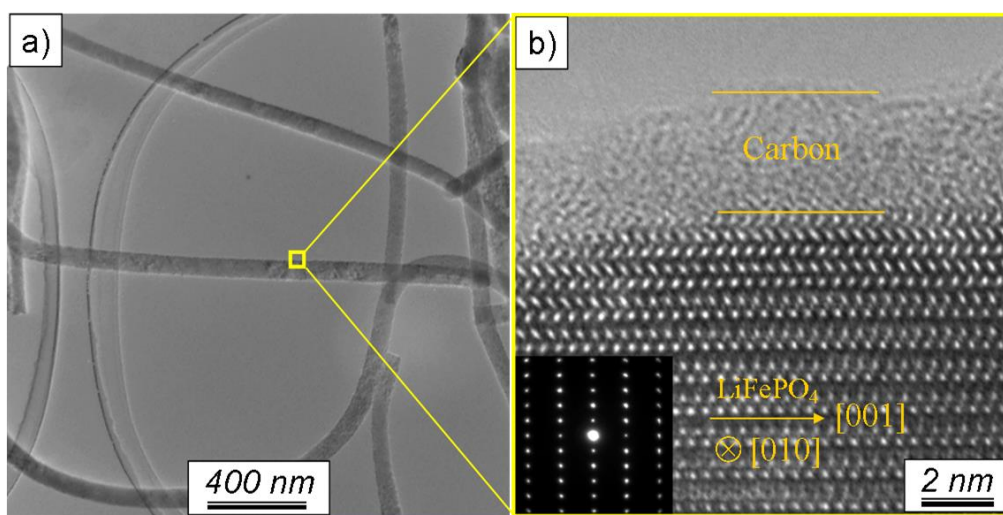


Figure 3.2.5 a) Overview TEM micrograph showing nanowires with a diameter of around 100 nm. b) Corresponding HRTEM image from the marked region, inset: SAED pattern, region of 500 nm in diameter. SAED pattern demonstrates that the growth direction is along *c*-axis (space group *Pnma*).

As seen in TEM (Figure 3.2.5a), the LiFePO₄ nanowires have a diameter of ~100 nm, which is also confirmed by SEM images. Selected area electron diffraction (SAED) allowed acquisition of a diffraction pattern over the whole diameter of a single nanowire, with the selected-area aperture being 500 nm. Figure 3.2.5b demonstrates single-crystallinity of the entire nanowire (hence denoted as SCNW-LFP) as well as growth of the nanowire along *c*-direction (referring to space

group *Pnma*). A preferred growth along the *c*-axis was also observed for plate-like LiFePO₄⁹⁵ and thumblike LiMPO₄ (*M* = Mn, Fe, Co, Ni) nanocrystals.⁹⁶ However, the main growth direction of large single crystals obtained by optical floating zone growth was along the *b*-axis.⁹⁷

As can be shown in Figure 3.2.5b, each nanowire is coated with an amorphous carbon layer of 2-5 nm thickness, which suppresses aggregation and at the same time it is thin enough not to block Li transport. (Note that efficient coating also results in isotropization of the Li transport.) All carbon coated single crystalline LiFePO₄ nanowires are loosely connected with each other to form a three-dimensional network.

As already stated, inorganic nanowires produced by electrospinning technique are usually polycrystalline. Only recently, single-crystalline metal oxide nanowires were reported (V₂O₅⁹⁸ and Nb₂O₅⁹⁹), and up to now, there are no reports on single-crystalline nanowires of multi-element materials such as LiFePO₄. Here reported single-crystalline LiFePO₄ nanowires are very stable in terms of structure. Remarkably, even after repeated Li extraction and insertion during battery cycling LiFePO₄ nanowire remains single-crystalline proved by HRTEM and related SAED pattern (Figure 3.2.6 a and b). It is interesting to compare such SCNW-LFP with single-crystalline Si, SnO₂, ZnO nanowires as battery materials. Si nanowires are transformed to amorphous phases during cycling due to the lattice expansion and SnO₂ and ZnO nanowires are converted to polycrystalline phase as a result of the conversion reaction.¹⁰⁰

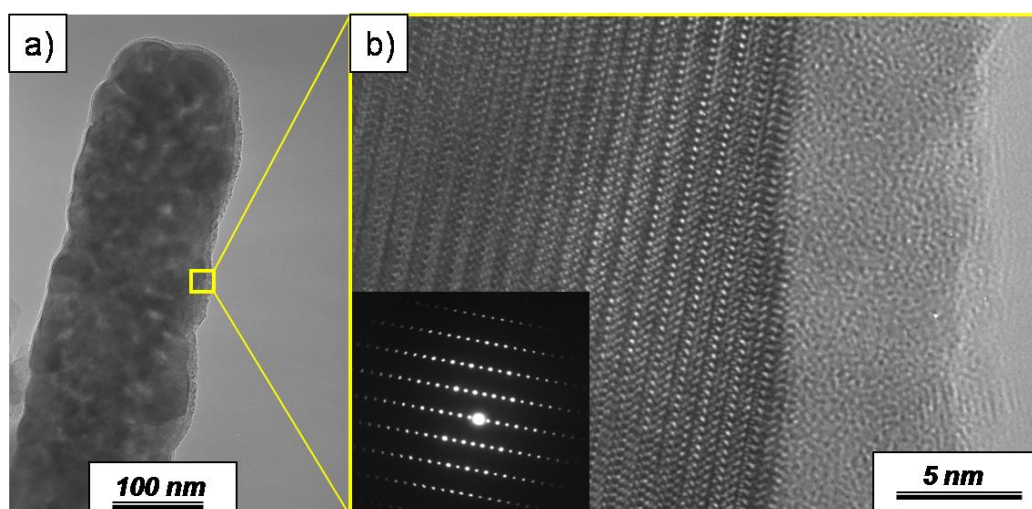


Figure 3.2.6 a) TEM image of SCNW-LFP after 25 charge-discharge cycles. b) Corresponding HRTEM image from the marked region showing that the single-crystalline structure is maintained. Inset: SAED pattern, region of 500 nm in diameter.

The proposed mechanism leading to single-crystalline nanowires is shown in Figure 3.2.7. In the polymer solution, all the PEO chains are curved and randomly oriented; the precursor ions, such as Fe³⁺, Li⁺ interact with the oxygen atom in the PEO chain. During the electrospinning process, the alignment of the PEO molecular chains as well as of the precursor ions along the fibrous axis is induced by the electric field.¹⁰¹ During heating of the as-prepared fibers, the well-oriented LiFePO₄ nucleus are formed which then fuse together to form single-crystalline LiFePO₄ nanowires with the help of the spatial confinement effect of the PEO chain. There are two possible reasons for the growth along the *c*-axis. The first one is that PEO chains could have different interactions with LiFePO₄ facets, causing the different growth rates for different facets. There are reports on other single-crystalline nanowires prepared using PEG polymer (short PEO chain, lower molecular weight) by the wet chemical methods, with similar anisotropic growth directed by the polymer.^{102, 103} The second possible reason could be the intrinsic properties of LiFePO₄ itself. Similarly, a preferred growth along the *c*-axis was also observed for plate-like LiFePO₄ nanocrystals,⁹⁵ and nano-thumblike LiMPO₄ (M = Mn, Fe, Co, Ni).⁹⁶

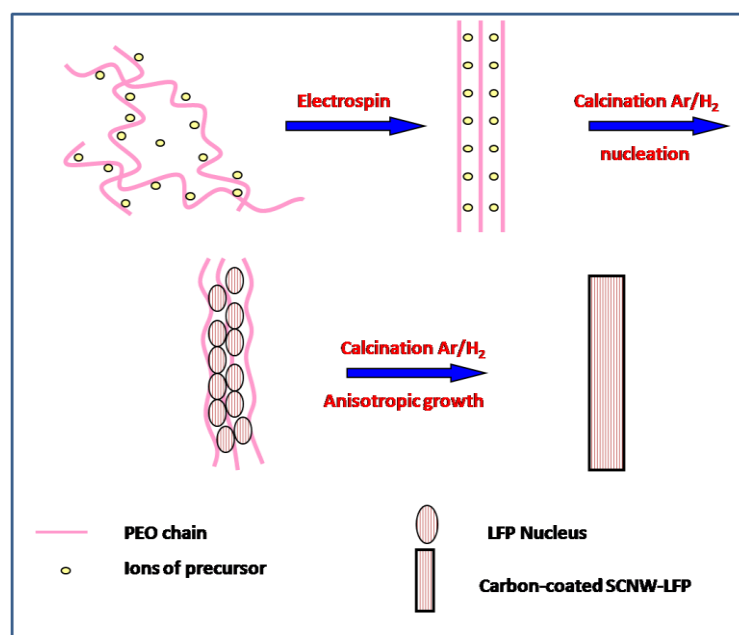


Figure 3.2.7 Proposed formation mechanism of carbon coated single crystalline LiFePO_4 nanowires.

3.2.3.2 Electrochemical performance of LiFePO_4 nanowires

Cyclic voltammetry was applied to investigate the electrochemical behavior of LiFePO_4 nanowires. The cyclic voltammetry curve of the initial cycle reveals redox peaks centered at 3.52 V (anodic peak) and 3.35 V (cathodic peak) and an additional small shoulder in the voltage range between 3.5 and 4.3 V. However, the shoulder gradually disappears in the subsequent cycles.¹⁰⁴ The redox peaks correspond to Li^+ extraction and insertion from the LiFePO_4 framework, respectively.

The unique structure of SCNW-LFP results in fair discharge capacities and rate performance, e.g., 169 (0.1 C), 162 (0.5 C), 150 (1 C), 114 (5 C), 93 mAh/g (10 C) at room temperature (charge and discharge profiles as shown in Figure 3.2.9). Note that the capacity at 0.1 C is close to the theoretical one of 170 mAh/g.

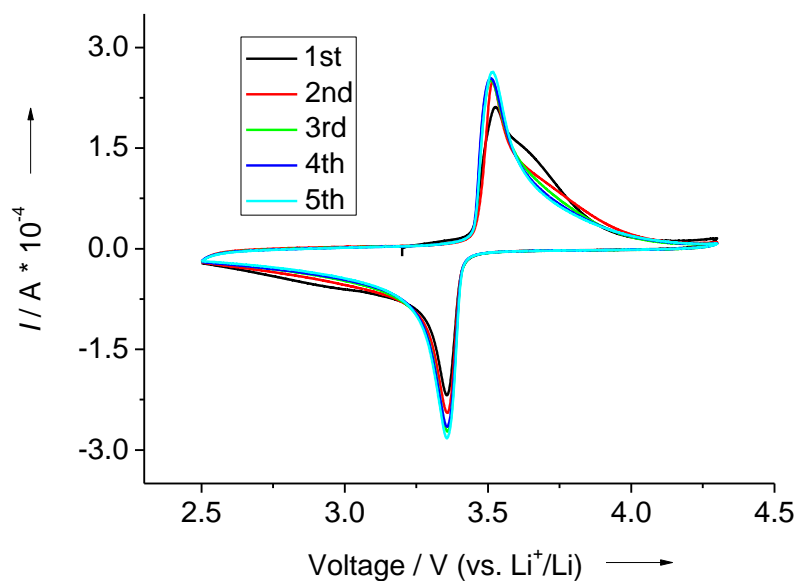


Figure 3.2.8 Cyclic voltammetry of SCNW-LFP, scan rate 0.1 mV/s.

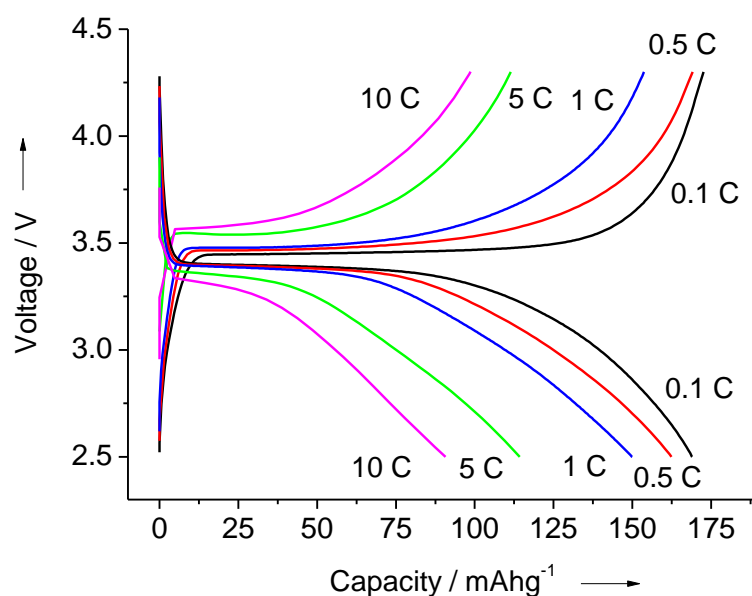


Figure 3.2.9 Charge and discharge profiles of SCNW-LFP at different C-rates.

However, also the battery assembly procedure has a pronounced influence on the final electrochemical performance of electrode materials (e.g. the thickness of active material, the loading of active material, amount of conductive carbon (Super-P)). In this work, usually 20 wt% of conductive carbon (Super-P) was used to prepare the electrode if without specially mentioning. For comparison, the rate capability of electrode containing only 10 wt% of conductive carbon is investigated as well.

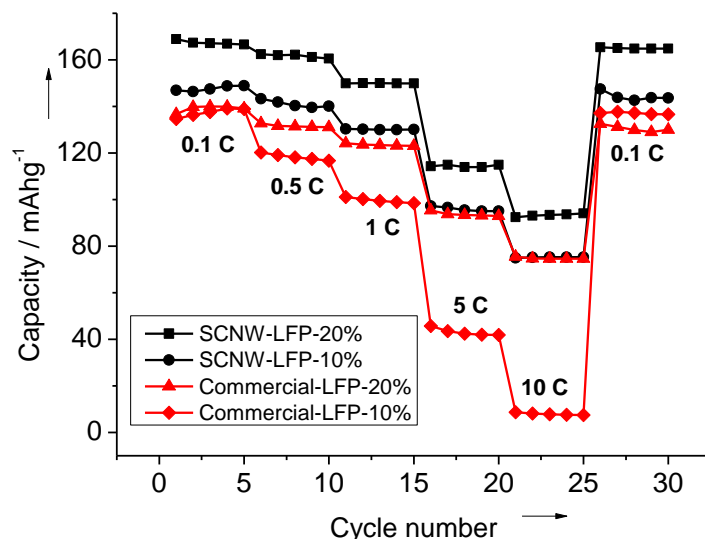


Figure 3.2.10 Rate performance of SCNW-LFP and commercial LiFePO₄ with 10 wt% and 20 wt% additional conductive carbon, respectively.

SCNW-LFP electrodes containing only 10 % conductive carbon show a capacity drop of only 15-20 mAh/g compared to electrodes with 20 % of carbon at each C-rate, even at the highest rate of 10 C (Figure 3.2.10). For comparison, the performance loss of commercial LiFePO₄ with only 10 % conductive carbon is more severe, and at 10 C rate the capacity becomes negligible (Figure 3.2.10). The results show very clearly that in case of SCNW-LFP the amount of additional conductive carbon is of less impact on the performance than for the commercial carbon-coated LiFePO₄ particles at high C-rate (over 1C). Therefore it can be concluded that the *in situ* carbon coating of the here presented nanowires produces a very effective electronic wiring of the active material which increases the electronic contact to the active material and reduces the charge transfer resistance. However, as demonstrated by cyclic voltammetry and impedance spectroscopy, polarization of the electrode increases with decreasing carbon content as expected, due to the reduction of electronic pathways to the current collector (Figure 3.2.11).

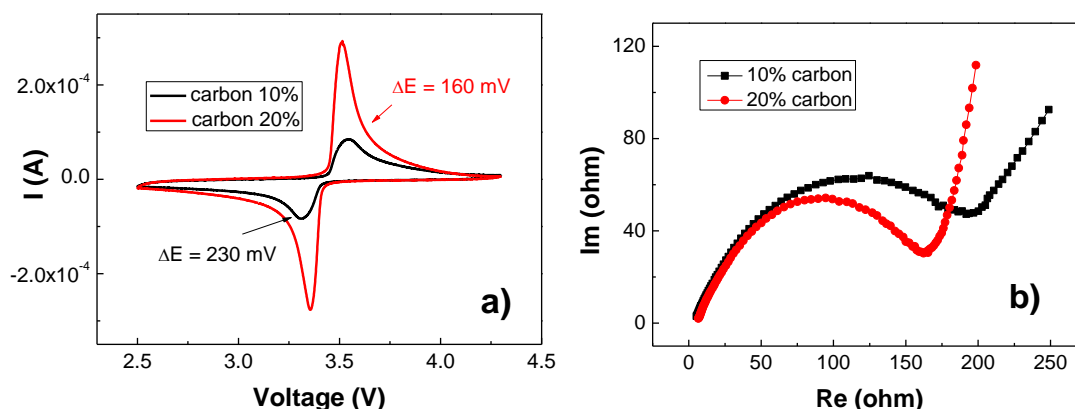


Figure 3.2.11 a) The 5th cyclic voltammetry scans of SCNW-LFP containing 20% and 10% conductive carbon, scan rate 0.1 mV/s. b) Impedance spectra for fresh cells assembled with the SCNW-LFP containing 20% and 10% conductive carbon.

The effect of elevated operating temperature on the electrochemical performance of SCNW-LFP was also studied. The discharge capacity of the electrode increases at 60 °C due to improved kinetics, as expected. At relative low C-rate (0.5 C), SCNW-LFP with both 10 % and 20 % additional conductive carbon deliver almost theoretical capacity (170 mAh/g), and even at 10 C, capacity values as high as 134 mAh/g (20 % carbon) and 123 mAh/g (10 % carbon), respectively, were obtained (Figure 3.2.12). Furthermore, SCNW-LFP shows excellent cycling stability at both room temperature and elevated temperature (Figure 3.2.13). At room temperature, a capacity as high as 146 mAh/g can still be obtained after 100 cycles at 1C discharge rate (86 % of the theoretical capacity). As already shown, the morphology of SCNW-LFP is maintained during cycling (Figure 3.2.6), enabling good capacity retention and cycling stability. At 60 °C, almost the theoretical capacity was achieved at 1 C, and 98 % capacity retention was obtained after 100 cycles, which implies good control of iron dissolution in SCNW-LFP even at high temperatures due to homogenous in-situ carbon coating. Excellent cycling stability could be attributed to the single-crystalline properties of the nanowires, as ordered atom arrangement in single-crystalline nanowires enables fast and reverse Li⁺ ion intercalation / deintercalation, contrary to polycrystalline nanowires, which suffer from poor

interconnection between nanograins during cycling.¹⁰⁵

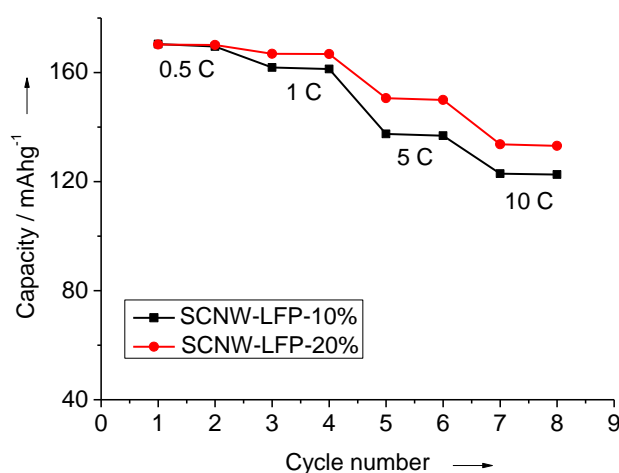


Figure 3.2.12 Rate performance of SCNW-LFP with 10 % and 20 % additional conductive carbon, respectively, at 60 °C.

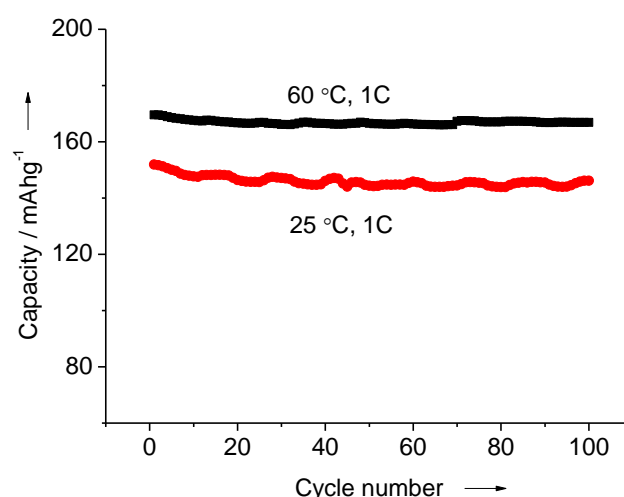


Figure 3.2.13 Cycling stability of SCNW-LFP at 1C rate at room temperature and 60 °C.

The battery performance of SCNW-LFP is improved compared to previously reported carbon-coated LiFePO₄ nanowires also produced by electrospinning.⁹⁴ Even triaxial LiFePO₄ nanowires with a carbon nanotube core, which improves the conductive network as well as the performance, show lower discharge capacities (160 (0.06 C), 130 (0.6 C), 80 mAh/g (6 C)⁹⁴) than SCNW-LFP, which can be attributed to the smaller thickness and well-ordered structure of single-crystalline nanowires. (The

comparison is based on the reported discharge capacities whereas parameters such as electrode thickness and loading were not given in Ref. ⁹⁴. Note that these parameters can largely affect the battery performance.) Similar electrochemical behaviour was observed in selected carbon-coated nanoparticles with 100 nm¹⁰⁶ diameter for which decisive parameters such as carbon content, thickness of the carbon layer, and transport lengths are comparable to such SCNW-LFP. However, the overpotentials of oxidation and reduction as derived from cyclic voltammetry are significantly higher in case of the nanoparticles ($\Delta V \sim 0.9$ V) than for SCNW-LFP ($\Delta V \sim 0.23$ V, Figure 3.2.11). As a result, SCNW-LFP is close to an optimized morphology for the performance: one long dimension supports the fast electron transport through the wires and two short dimensions facilitate fast Li transport. This has been previously emphasized by Bruce for the TiO₂ electrode.⁵⁷

In brief, the good electrochemical performance of LiFePO₄ nanowires is attributed to their unique morphology, which is beneficial for the improvement of both electronic and ionic transport. Firstly, the growth of SCNW-LFP along the *c*-axis (Figure 3.2.5b) leads to short transport pathways along *b*- and *a*-direction. As stated in the introduction of this thesis, in the orthorhombic LiFePO₄ with space group *pnma*, Li⁺ ion preferably move along the *b*-direction rather than *a*- or *c*- directions. (Whether or not transport in the *b*-direction is perceptibly faster than along the *c*-axis seems to depend on the degree of Li/Fe anti-site disorder⁴³.) The short distance in the *b*-direction (~100 nm) will lead to the short diffusion time for Li⁺ ion in LiFePO₄, and rapid lithium diffusion, *viz.* along *b*-axis, is expected. Together with the well ordered single-crystalline structure of the nanowires, this promotes fast Li insertion/extraction. Secondly, the homogeneous and continuous carbon layer allows fast electron transport and is not too thick to damage the Li⁺ ion intercalation. Finally, the SCNW-LFP are connected to each other to form 3D network, enabling electron transport through the whole conductive network.

In terms of morphology of LiFePO₄, carbon coated nanowires have better percolation behavior compared to LiFePO₄/C nanoparticle composite (Figure 3.2.14). Nanowires only need several connection points in order to ensure the transport of

electrons in the whole network, while for the nanoparticles, the lost of contact of LiFePO₄ particles will lead to the polarization behavior.⁵³

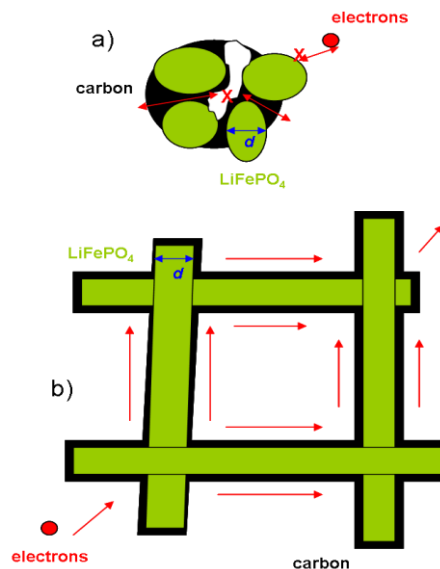


Figure 3.2.14 a) Electron transporting pathway for LiFePO₄ with discontinuous carbon layers. b) Ideal electron-transfer pathway for SCNW-LFP with homogeneous and continuous carbon layers.

3.2.4 Conclusions

In summary, single-crystalline carbon-coated LiFePO₄ nanowires synthesized by the electrospinning method are reported. These nanowires do not only differ in crystallinity from previous reports, they are also substantially thinner. The nanowires grow along the *c*-direction and feature a uniform and continuous carbon coating of moderate thickness. In this way, an efficient conductive network is formed with very short diffusion lengths along *b*-axis leading to very good rate performance (theoretical capacity at 0.1C and 93 mAh/g at 10C) and cycling capability (146 mAh/g at 1C after 100 cycles). Moreover, this synthesis procedure gives us a possibility to prepare single crystal nanowires of different cathode materials, such as LiMPO₄ (M=Fe, Mn, Co), Li₂MSiO₄ (M=Fe, Mn, Co) and Li₂MPO₄F (M=Fe, Mn, Co).

3.3 Surfactant-assisted polyol method for preparation of LiFePO₄ nanoparticles

3.3.1 Introduction

As already stated, reduction of size is a very crucial approach to increase the rate performance of LiFePO₄ through shortening of the electronic and ionic transport pathways. Moreover, size effects of LiFePO₄ are very important fundamental questions which still need to be answered. In order to get a deeper insight, LiFePO₄ with various particle sizes has to be prepared. There are numerous investigations on the synthesis methods for reduction of the particle size of LiFePO₄, especially soft chemistry approaches. Wang et al. successfully prepared ~50 nm LiFePO₄ with effective carbon coating by co-precipitation method combined with *in situ* polymerization.⁵³ Aniline monomers were polymerized and covered the surface of as-formed FePO₄ particle simultaneously during precipitation reaction, which prevented further growth of nuclei. Such polymeric surface was transformed into thin conductive carbon layer during sintering step. However, synthesizing LiFePO₄ with particle sizes smaller than 40 nm and systematic control of the particle size remains a challenge. Such size controlled synthesis is another objective of this thesis.

Polyol method is a widely used method to prepare nano-structured materials, including metals,¹⁰⁷ oxides¹⁰⁸ and metal-containing compounds¹⁰⁹ in different polyol mediums (e.g. diethylene glycol, triethylene glycol and tetraethylene glycol). Kim et al. used polyol method to prepare LiFePO₄ nanorods (20*50 nm) for the first time.⁸² Rangappa et al. employed Oleyamine (OL) as surfactant to synthesize nanosized LiFePO₄ with thickness smaller than 20 nm (the smallest size ever reported for such materials) by a supercritical ethanol process.¹¹⁰ In this work, an oleyamine-assisted polyol method was developed to prepare LiFePO₄ nanoparticles with various sizes.

3.3.2 Synthesis

A stoichiometric equimolar ratio of Li-CH₃COO, Fe-(CH₃COO)₂, and NH₄H₂PO₄ was dissolved/dispersed in a tetraethylene glycol (TEG) and oleyamine (OL) mixture with different volume ratios. For attaining LiFePO₄/carbon nanotube (CNT) nanocomposite, ~5wt% of CNTs was suspended in the TEG/OL solution. The

precursor solution was heated at 320 °C (controlled by the thermocouple) in a round-bottom flask with magnetic stirring attached to a refluxing condenser. The resultant LiFePO₄ nanorods were collected by repeated washing and centrifugation with ethanol, acetone and hexane for 3 times respectively, followed by drying in a vacuum oven at 80 °C for 20 hours. In some cases, the as-prepared powders are post heat treated in Ar (95%)/H₂ (5%) atmosphere for 2 hours.

3.3.3 Results and discussions

3.3.3.1 Size controlled synthesis of LiFePO₄ nanoparticles

There are several significant parameters involved in the OL-assisted polyol method, such as e.g. surfactant concentration, reaction temperature, reaction time, and precursor concentration. In this work, all the reported sizes of LiFePO₄ particles (*d*) were calculated by whole powder pattern refinement using Topas4 software. In each set of experiments, one of the parameters was varied while all remaining parameters were kept constant.

a) Effect of OL concentration

The effect of surfactant concentration on the size of the final product was investigated by varying the volume ratio of OL and TEG. Figure 3.3.1 exhibits the powder XRD patterns of LiFePO₄ prepared in the OL/TEG mixture, with volume ratios 0:1 (black curve), 1:1 (red curve) and 7:3 (blue curve), respectively. All the peaks can be indexed to orthorhombic olivine LiFePO₄ with space group (*Pnma*) (JCPDS card No.01-081-1173) without any detectable impurities such as Fe₂P₂O₇, Fe₂O₃, or Li₃PO₄. As shown in Figure 3.3.2 a, higher volume ratios of OL/TEG lead to smaller particle sizes. Without OL, LiFePO₄ nanocrystals with particle size of about 60 nm were obtained, while the particle size can be reduced to ~40 nm and ~30 nm, when the amount of OL is increased (volume ratios of OL/TEG 1:1 and 7:3, respectively).

The influence of the surfactant addition on the particle size was also confirmed by transmission electron microscopy (TEM) (Figure 3.3.3) (thickness and length distributions are given in the Figure 3.3.4). Without OL (Figure 3.3.3 a, Figure 3.3.4)

the obtained nanorods (with thickness around 20~40 nm and length about 30~80 nm) have similar morphologies as previously reported.⁸² With the increased concentration of OL such nanorods become smaller in diameter and of more homogeneous shape (Figure 3.3.3 b, 3.3.3 c, Figure 3.3.4). For example, with OL/TEG volume ratio of 7:3, the thickness of nanoparticles can be reduced to about 10~20 nm with length of around 20~40 nm. The consistent trend deduced from the TEM images and estimated XRD values demonstrates that OL is a very effective capping agent inhibiting particle growth and favoring anisotropic growth.

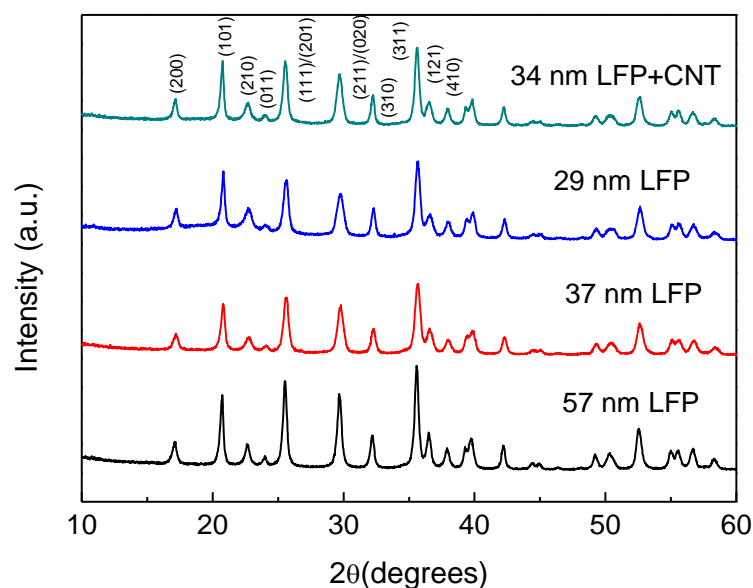


Figure 3.3.1 XRD patterns of LiFePO₄ nanocrystals with different particle sizes and LiFePO₄/CNT composite prepared by oleylamine-assisted polyol method.

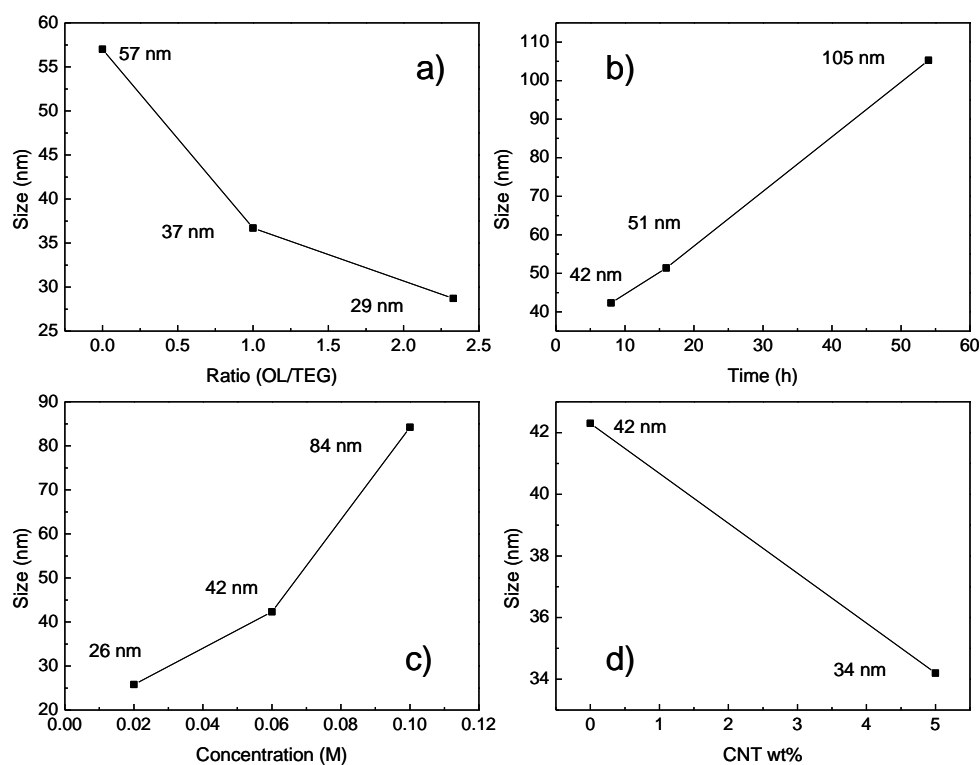


Figure 3.3.2 Effects of different reaction parameters on the particle size of LiFePO_4 nanocrystals prepared by OL-assisted polyol method: (a) volume ratio of OL and TEG (0.02M, 12h); (b) reaction time (0.06M, OL/TEG=7:3); (c) precursor concentration (OL/TEG=7:3, 8h); (d) carbon nanotube addition (0.06M, OL/TEG=7:3, 8h).

b) Effects of reaction temperature and reaction time

The reaction temperature was kept constant at the boiling point of TEG (320°C^{111}). The maximum temperature drop is around 10°C due to the boiling of the solution. No LiFePO_4 phase could be detected if the reaction temperature is set below 270°C .

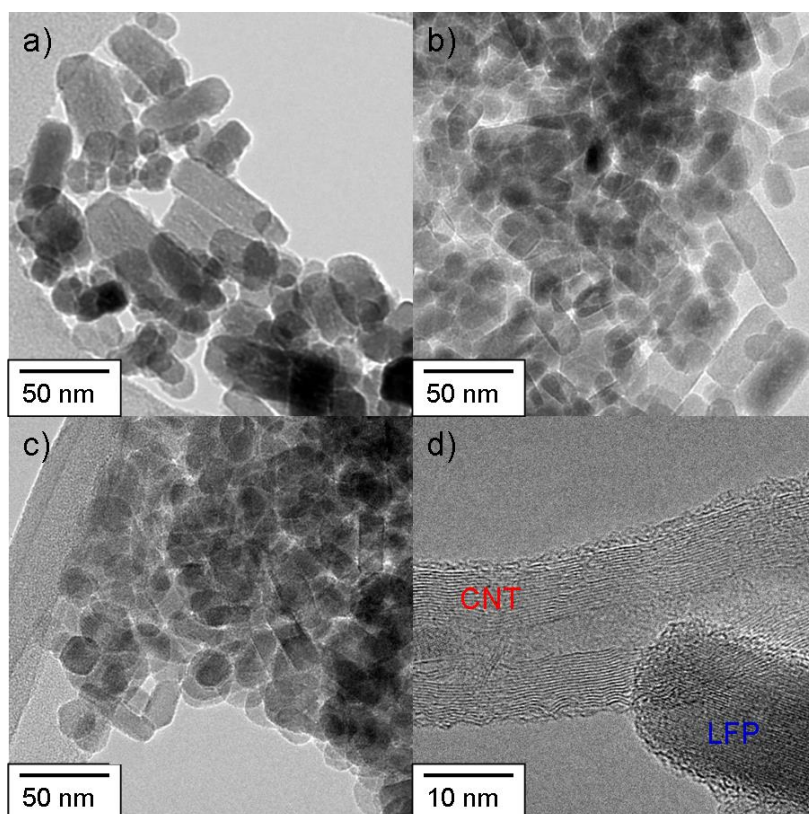


Figure 3.3.3. TEM images; (a, b, c) LiFePO₄ nanocrystals with different sizes (57nm, 37 nm, 29nm) prepared using different OL/TEG volume ratio (0:1, 1:1, 7:3). (d) HRTEM image of LiFePO₄/carbon nanotube composite.

The particle size variation as a function of reaction time was also investigated. As indicated from Figure 3.3.2 b, the nanorods become larger by extending the reaction time from 8h to 54h. Therefore, smaller particle sizes could be synthesized by using shorter reaction times. However, the reaction time was found to have no obvious influence on the size once it was reduced to less than 12h.

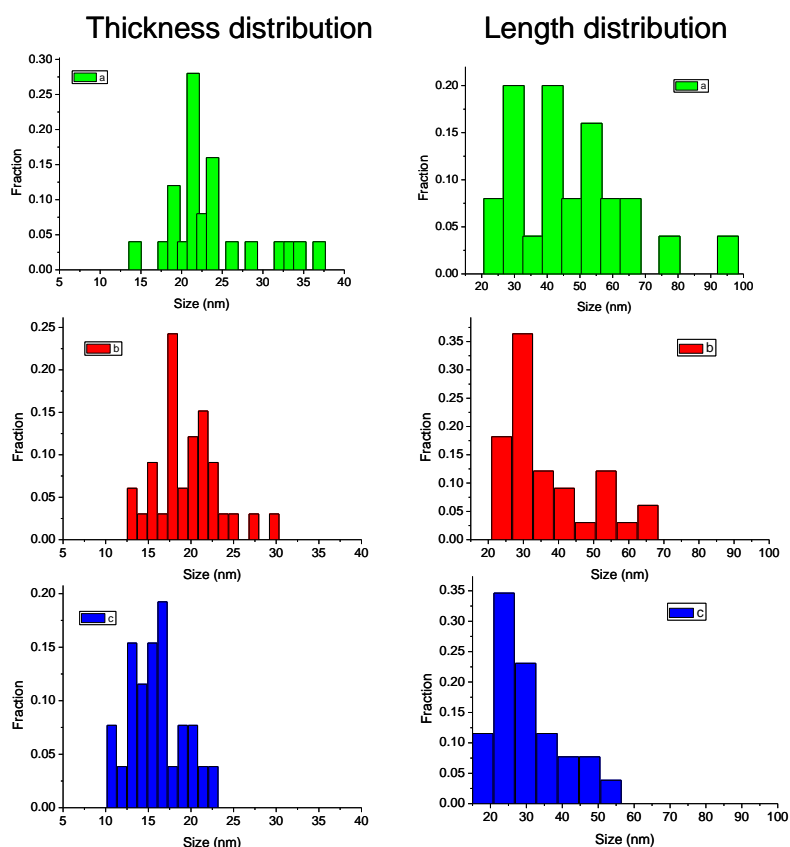


Figure 3.3.4 Thickness and length distributions of nanocrystalline LiFePO_4 (corresponding to Figure 3.3.3 a, b and c).

c) Effect of the precursor concentration

In soft chemical synthesis, a higher precursor concentration typically leads to a higher number of nuclei with smaller critical radius, thus smaller particles with high interfacial energy are obtained. Subsequently, small particles undergo Ostwald ripening.¹¹² In OL-assisted polyol method, the precursors formed a suspension instead of a real solution; therefore, the precursor concentration indeed has an influence on the nucleation and growth of LiFePO_4 nanocrystals. As shown in Figure 3.3.2 c, the particle size obtained with a precursor concentration of 0.02 M is around 30 nm, while the sizes increase to ~40 nm and ~80 nm when the concentration is raised to 0.06 and 0.1 M, respectively. In conclusion, a smaller particle size is favored with lower precursor concentrations. Nevertheless, with very low concentration of the precursors, the yield of the reaction is unsatisfactory and only limited amount of material can be retrieved.

d) Effect of carbon nanotube (CNT) addition

Composites of LiFePO₄ and CNT (LiFePO₄/CNT) provide promising morphologies with enhanced percolation effect and improved electrochemical performance. Murugan et al. synthesized nano-thumblike LiFePO₄ particles and then subsequently mixed them with carbon nanotubes via solution-based method to obtain a final composite, which showed improved electrochemical performance.¹¹³ LiFePO₄/CNT nanocomposites can be prepared through both *in situ* synthesis and *ex situ* mixing. Here, an appropriate amount of carbon nanotubes were added *in situ* to the precursor solution of TEG and OL (leading to formed ~5 wt% of the CNT in the composite). Single phase LiFePO₄ without any impurities as indicated by Figure 3.3.1 was obtained. As displayed in Figure 3.3.3 d, LiFePO₄ nanorods and CNTs are connected to each other, which gives rise to an effectively mixed conducting network. Furthermore, the carbon nanotube may inhibit the growth of LiFePO₄ nanocrystals, as shown in Figure 3.3.2 d, which is also suggested by literature.³⁰

3.3.3.2 Formation mechanism of LiFePO₄ nanocrystals in the OL-assisted polyol method

Based on the literature and the experimental results presented here, the nanocrystal formation mechanism for both polyol method and OL-assisted polyol method is believed to be surfactant-assisted oriented attachment growth. This mechanism has also been suggested by Rangappa et al. for the supercritical synthesis of LiFePO₄.¹¹⁴ Figure 3.3.5 schematically illustrates LiFePO₄ nanocrystal formation for polyol and OL-assisted polyol method. In the non-modified polyol method, only TEG acts as a capping agent, while in the OL-assisted polyol process, both TEG and OL serve as capping agents. In the early stage, sub-ten nanometer LiFePO₄ nanocrystals are formed. Subsequently, the TEG or OL molecules are capped on the surface of such nanocrystals directing the growth of LiFePO₄ nanocrystals through reducing the overall surface energy by eliminating specific surfaces. Furthermore, since OL is a more effective capping agent than TEG, it can lead to the formation of smaller nanorods. On the other hand, increasing reaction time and

precursor concentrations, naturally leads to larger particle sizes.

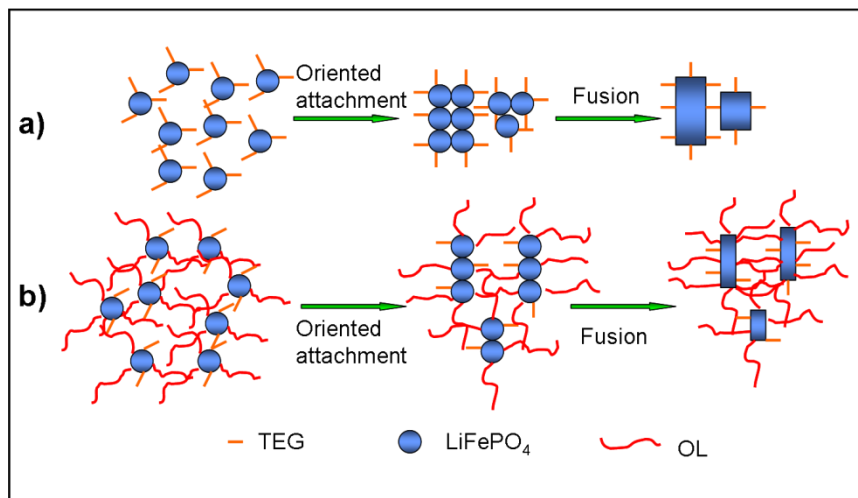


Figure 3.3.5 Schematic illustration of the LiFePO_4 nanorod formation mechanism in polyol (a) and OL-assisted polyol method (b).

3.3.3.3 Electrochemical performance of LiFePO_4 nanoparticles

The electrochemical performances for differently sized LiFePO_4 particles are shown in Figure 3.3.6. When the battery was charged and discharged with 0.1 C rate ($1\text{C} = 150\text{ mA/g}$) between 2.5 and 4.3V, the measured discharge capacities are 102, 64, 40 mAh/g for 44, 37, and 29 nm LiFePO_4 , respectively.

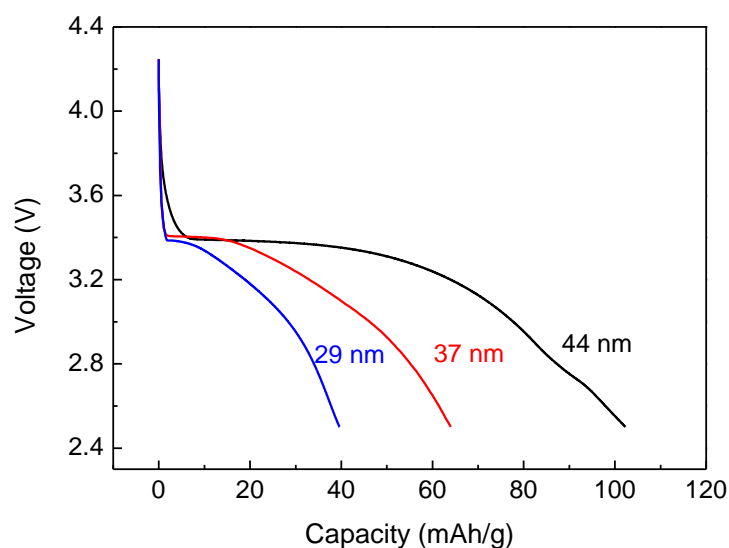


Figure 3.3.6 Discharge curves for LiFePO_4 with different sizes at 0.1C rate.

The lower capacity for smaller sized LiFePO₄ samples (Figure 3.3.6) indicates that the surface of the as-prepared sample (sample without post heat treatment) was covered with non-conductive amorphous carbon or with remaining organic molecules, which would affect electronic and ionic conductivity.¹¹⁵ The presence of an organic surface layer was confirmed by both HRTEM (Figures 3.3.7) and FTIR (Figure 3.3.8). As known from literature, the bands in the region 2800-2960 cm⁻¹ are attributed to the C-H stretching mode of methyl and methylene groups in FTIR spectra.¹¹⁰ From Figure 3.3.8, both LiFePO₄ prepared by non-modified polyol method and by OL-assisted polyol method are covered by organic molecules. In order to remove these non-conductive coatings, two methods can be used: washing with suitable solvents and sintering at high temperatures (≥ 400 °C). As to the non-modified polyol method, the resultant LiFePO₄ is usually washed by ethanol and acetone; while for OL-assisted supercritical ethanol method, tetramethylammonium hydroxide (TMAOH) is suggested for the removal of the OL ligand.¹¹⁰ However, in this work, washing is not effective as it does not remove TEG and OL residues for both synthesis methods as confirmed by FTIR. In fact, for nanoparticles, especially those smaller than 40 nm with large surface area and high surface energy, difficulties in removal of all of the CH_x ligands on the surface of particles are expected. Additionally, TMAOH is a basic solvent, which is harmful to LiFePO₄ (Fe²⁺ leaching). During the washing process, a slight color change of LiFePO₄ powders was indeed observed.

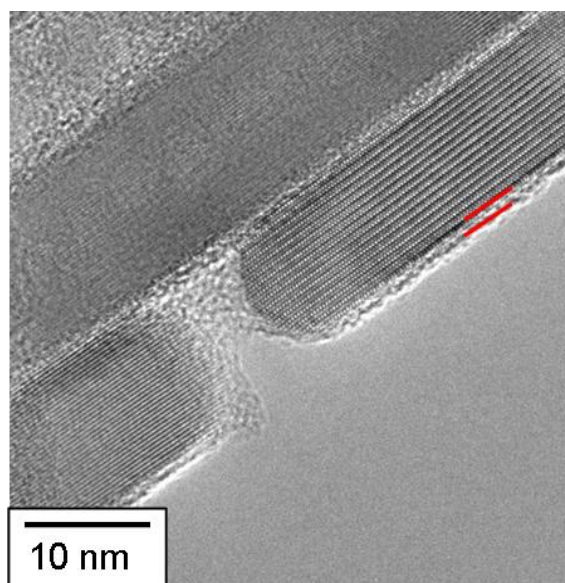


Figure 3.3.7 HRTEM image of LiFePO_4 nanocrystals. An organic layer can be seen on the surface of LiFePO_4 nanocrystals. Note that the surface layer was marked by red lines.

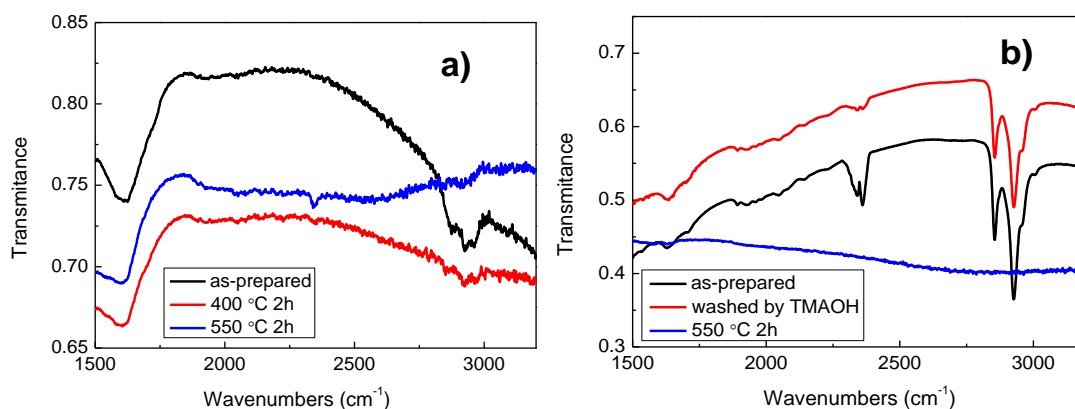


Figure 3.3.8 FTIR spectra: (a) LiFePO_4 prepared by polyol method (as-prepared sample and samples sintered at 400 and 550 °C); (b) LiFePO_4 prepared by oleylamine assisted polyol method (as-prepared sample, sample additionally washed with TMAOH and sample sintered at 550 °C).

Sintering nanoparticles at higher temperatures is an effective approach to remove the organic layers, as confirmed by FTIR (Figure 3.3.8). For LiFePO_4 heated at 400 °C, 550 °C and 700 °C in Ar/H_2 atmosphere, organic molecules and non-conductive carbon on its surface was converted to more conductive carbon layer. Typically a short

sintering time (2 hours) is enough for such a surface modification. As shown in Figure 3.3.8, small amount of CH_x remained on the surface if the sample was sintered at 400°C; while all of the organic CH_x transformed to carbon if the temperature was increased above 550°C.

The effective chemical diffusion coefficient approximately determines the transport property of Li in the lattice of the host electrode, which is normally the rate determining step during charge and discharge. Measuring diffusion coefficients is hence crucial for understanding the intrinsic kinetics in LiFePO₄. Here, cyclic voltammetry (CV) was applied to measure the effective chemical diffusion coefficient for LiFePO₄/CNT composite sintered at different temperatures. Figure 3.3.9a shows CV curves at different scan rates for the samples sintered at 700°C for 2 hours (CV curves for other samples are similar). The cyclic voltammetry curve reveals redox peaks centered at 3.55 V (cathodic peak) and 3.33 V (anodic peak) at scan rate (ν) of 0.1 mV/s. The redox peaks correspond to Li⁺ extraction and insertion from the LiFePO₄ framework, respectively, which can still be clearly identified at a scan rate of 2 mV/s. The cathodic peaks shift to higher potential while anodic peaks shift to lower potential respectively as scan rates increase. The peak current (I_p) increases with the higher scan rate as well. The intensity of cathodic peaks is higher than that of anodic peaks, indicating differences between Li extraction and insertion kinetics. Figure 3.3.9b shows the plot of I_p vs $\nu^{1/2}$, and the linear relation is typical for a diffusion controlled process.

The effective chemical diffusion coefficient can be obtained by the Randles-Sevcik equation. The effective chemical diffusion coefficients for charge and discharge process regarding samples sintered at different temperatures are summarized in Table 3.3.1. For all the samples, they are larger for the charge than for the discharge process. The value of the diffusion coefficient for the sample sintered at 700°C for 2 hours is the highest, and it is almost 2 orders of magnitude higher than for as-prepared sample, proving the importance of the surface modification. An enhanced electrochemical performance can be expected for the samples with higher diffusion coefficients.

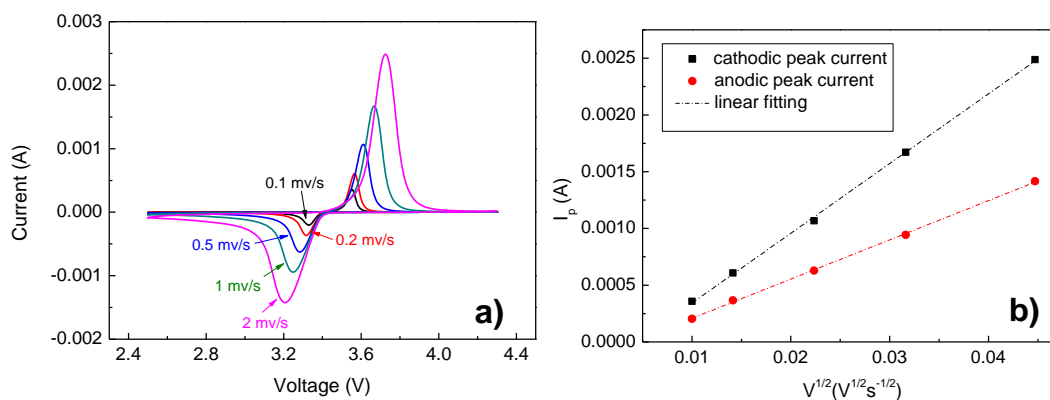


Figure 3.3.9 (a) Cyclic voltammetry curves of LiFePO₄/CNT composite sintered at 700 °C for various scan rates; (b) Peak current I_p as a function of square root of scan rate $v^{1/2}$.

Table 3.3.1 Apparent chemical diffusion coefficient for both charge and discharge process in LiFePO₄/CNT: as-prepared sample and samples sintered at 550 and 700 °C.

Sample	D charge (cm ² /s)	D discharge (cm ² /s)
As-prepared	1.167E-12	6.731E-13
550 °C -2h	5.188E-11	2.570E-11
700 °C -2h	1.628E-10	5.156E-11

Studies on the electrochemical performance of LiFePO₄/CNT composite allowed getting deeper insight into the sintering effect. The as-prepared LiFePO₄ shows a fair discharge capacity and rate performance (Figure 3.3.10), e.g. 116 (0.1C), 89 (0.5C), 78 (1C), 53 (5C), 42 (10C) mAh/g (1C=150 mA/g, the same C-rate was applied to both charge and discharge process), while the sample sintered at 550 °C for 2 hours exhibits considerably better capacities at all C rates. However, when it comes to even higher C-rate, in the range of 20C to 100C, the capacity drops drastically. The sample sintered at 700 °C for 2 hours shows the best rate performance at all C-rate compared to other samples, e.g. 157 (0.1C), 153 (0.5C), 147 (1C), 121 (5C) and 109 (10C) mAh/g, and even for very high C-rate (note: both charge and discharge at high C-rate), the electrochemical performance is still good enough, 102 (20C), 92 (30C),

78 (50C), 72 (60C) and 56 (100C) mAh/g. The good capacity retention (almost 99%) was also observed in the sample sintered at 700 °C, which after high rate test (100C) still had a capacity of 145 mAh/g at 1C rate.

Figure 3.3.11 shows the cycling performance at 10C for 1000 cycles with respect to the samples cycled after high C-rate performance test (Figure 3.3.10, up to 100C) and the freshly prepared sample. In general, the lattice structure of the electrode materials will be distorted after many high C-rate charge/discharge cycles. Additionally, the particles easily loose contact with each other and with the conductive carbon black due to the volume change after cycling, which will also damage cycling stability. However, in this work, sintered LiFePO₄ showed excellent cycling performance. The sample sintered at 700 °C exhibited better cycling performance than the one sintered at 550 °C, with 82% capacity retention compared to the first cycle even after high C-rate test (up to 100C). When a freshly prepared cell (Li//LiFePO₄) was directly cycled at 10C, the capacity gradually increased for the first 200 cycles and then stabilized, with 92% capacity retention even after 1000 cycles at 10C.

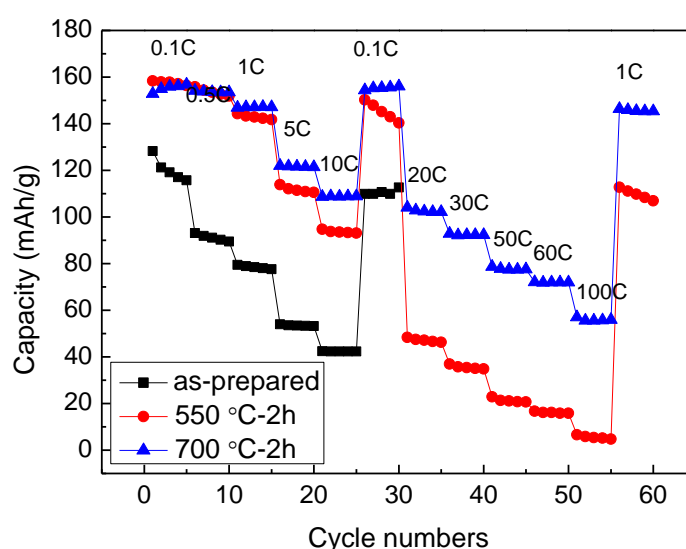


Figure 3.3.10 Rate performance of as-prepared LiFePO₄/CNT composite sample, samples sintered at 550 and 700 °C.

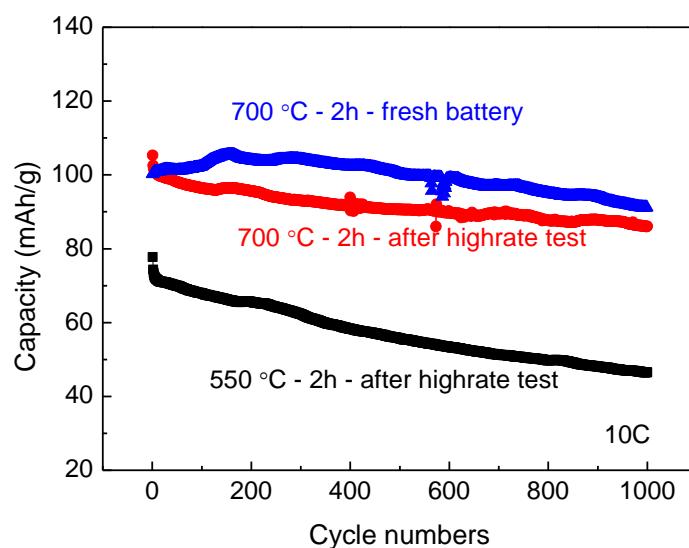


Figure 3.3.11 Cycling stability at 10C of LiFePO₄/CNT composite sintered at 550 and 700 °C (after high rate test and freshly prepared).

The improved rate performance and cycling stability are attributed to two possible reasons. Firstly, high temperature sintering converts the remaining organic molecules and non-conductive amorphous carbon to conductive carbons, which will increase the electronic and ionic conductivity, as well as the effective chemical diffusion coefficient, and finally leads to excellent rate performance. Secondly, sintering at high temperature can improve crystallinity and minimize the defects (e.g. anti-site defects, blocking Li transport channel⁸), thus enhancing the Li conductivity in the lattice.

However, it is important to mention that after sintering (550, 700 °C), the LiFePO₄ does not maintain its morphology and size, and the particles grow into 100-200 nm (Figure 3.3.12). Based on the discussion above, it is obvious that the electrochemical performance of 100 nm LiFePO₄ is much better than of 40 nm LiFePO₄ with different surface modification (effective surface carbon coating vs. organic molecule or non-conductive amorphous carbon). As a result, in terms of electrochemical performance, the surface modification is more important than the variation of particle size, which is also suggested in a recent publication.⁴⁴

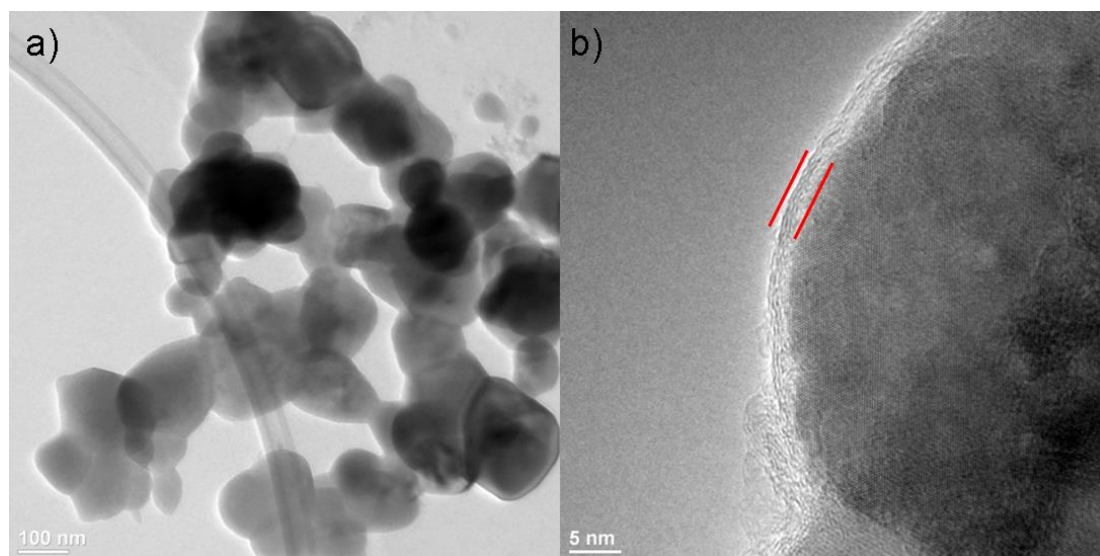


Figure 3.3.12 a) TEM and b) HRTEM images for LiFePO₄/CNT composite after heat-treatment (550 or 700 °C). A thin carbon layer (~3 nm, marked by red lines) can be seen on the surface of LiFePO₄ nanocrystals.

3.3.4 Conclusions

In summary, oleylamine-assisted polyol method is a facile process to prepare LiFePO₄ nanocrystals smaller than 40 nm (the thickness is only around 10 nm). The particle size could be systematically controlled by variation of the concentration of surfactant, reaction time, precursor concentration and CNT admixtures. A surfactant-assisted oriented attachment growth mechanism was proposed for the oleylamine-assisted polyol method. The good rate performance (up to 100C) and cycling stability (1000 cycles at 10C) for the sample prepared through oleylamine-assisted polyol method with sintering at 700 °C for 2 hours indicates that given the size window of 20~150 nm, the surface modification (quality of carbon coating) is more important than the particle size in terms of the electrochemical performance.

3.4 Amorphous LiFePO₄ by precipitation method

3.4.1 Introduction

In order to further investigate the size effects on LiFePO₄, the other metastable

form of LiFePO₄ cannot be ignored, namely amorphous LiFePO₄. Amorphous LiFePO₄ can be treated as an extreme case of nanocrystalline LiFePO₄, in which the grain sizes are further reduced and the whole material loses long range order.¹¹⁶ As for amorphous LiFePO₄, there has been very scarce work about its synthesis and electrochemical properties, not to mention the size effect on the open circuit voltage (OCV) variations. Isono¹¹⁷ et al. applied melt quench technique to investigate different kinds of amorphous Li-Fe-P-B-O, and monotonically charge-discharge curves were displayed, with the capacity between 76 and 119 mAh/g. In contrast to amorphous LiFePO₄, amorphous FePO₄ was prepared by different synthesis approaches and the corresponding electrochemical properties were investigated by some groups.¹¹⁸⁻¹²¹

3.4.2 Preparation of amorphous LiFePO₄

Amorphous FePO₄ was prepared as follows: an equimolar water solution of Fe(NH₄)₂(SO₄)₂•6H₂O and NH₄H₂PO₄ were mixed in a 1:1 volume ratio. H₂O₂ was added to the solution under vigorous stirring. The white precipitate was collected by the repeated washing and centrifugation with distilled water 3 times. After drying in the oven at 400 °C for 2 hours, amorphous FePO₄ was obtained. Amorphous LiFePO₄ was prepared by chemical lithiation of amorphous FePO₄ by LiI in the acetonitrile solution, after stirring for 24h and then was collected by centrifugation. Heating the amorphous LiFePO₄ in Ar/H₂ (95:5) atmosphere at 550°C for 2 hours, the crystalline LiFePO₄ can be obtained.

3.4.3 Results and discussions

3.4.3.1 Characterization of amorphous LiFePO₄

Amorphous LiFePO₄ was prepared by spontaneous precipitation method as described in the experimental section. The amorphous FePO₄ was obtained first, which is confirmed by the XRD pattern (Figure 3.4.1). The TG/DSC curves for amorphous FePO₄ are shown in Figure 3.4.2. Continuous weight loss from room temperature until 400 °C is observed, which corresponds to the water loss (green line

in TG curve). The water elimination process is also confirmed by the broad peak in DSC curve around 250 °C (blue curve in Figure 3.4.2). The molecular formula of as-prepared FePO₄ is FePO₄•1.5H₂O, calculated from the 15% weight loss seen in TG curves. The sharp peak in the DSC curve at 560 °C reveals the crystallization process of amorphous FePO₄, and the sharp peak at 770 °C in DSC curve (without weight loss) can be assigned to $\alpha \rightarrow \beta$ transition in quartz-like materials.¹²² Before lithiation of the amorphous FePO₄, the residual water should be removed. Thus, based on the TG/DSC measurements, the material was heated in the air at 400 °C for 24 hours. Its amorphous property maintains after such heat treatment as confirmed by XRD patterns in the Figure 3.4.1.

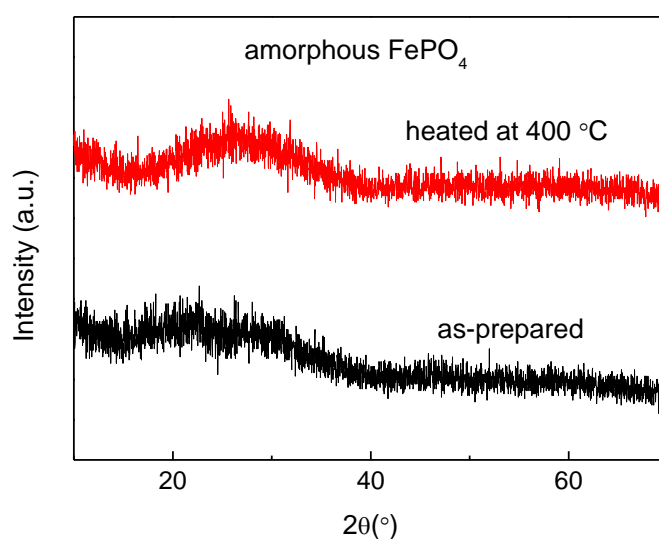


Figure 3.4.1 XRD patterns of as-prepared amorphous FePO₄ and after heating at 400 °C.

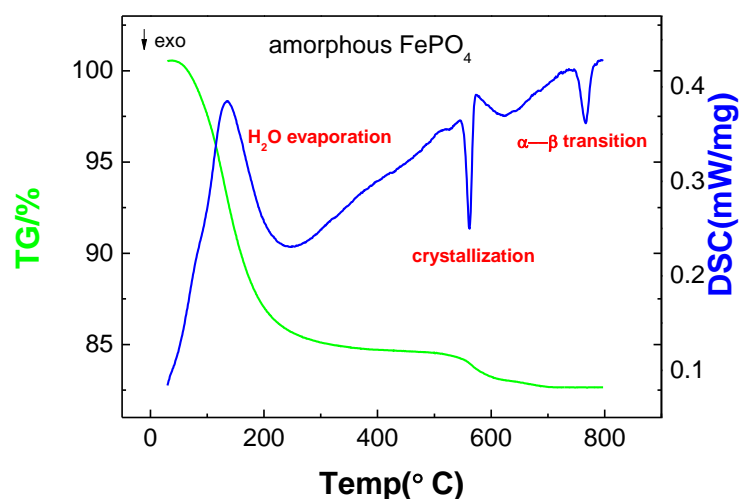


Figure 3.4.2 TG (green) / DSC (blue) curves for as-prepared amorphous FePO_4 recorded from room temperature to 800 °C at a heating rate of 10 °C/min.

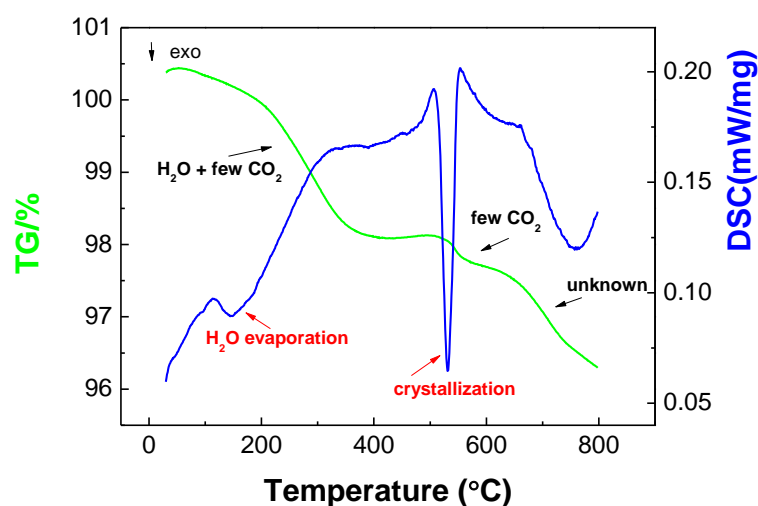


Figure 3.4.3 TG (green) / DSC (blue) curves for as-prepared amorphous LiFePO_4 recorded from room temperature to 800 °C at a heating rate of 10 °C/min.

Figure 3.4.3 shows TG/DSC curves for amorphous LiFePO_4 . The peak in the DSC curve (blue curve in Figure 3.4.3) around 142 °C corresponds to the water loss; the peak at 529 °C can be attributed to the crystallization of amorphous LiFePO_4 and the peak around 758 °C is probably due to decomposition.

The evolution of amorphous LiFePO_4 with heating (in Ar/H_2 atmosphere) was investigated by XRD (Figure 3.4.4). When the temperature is lower than 400 °C,

amorphous LiFePO₄ is maintained, while if temperature is above the 450 °C, crystalline LiFePO₄ starts to form. When the heating temperature is 550 °C, well-crystalline and phase-pure LiFePO₄ is obtained, and all the peaks in XRD can be indexed to orthorhombic olivine LiFePO₄ with space group (*Pnma*) (JCPDS card No.01-081-1173).

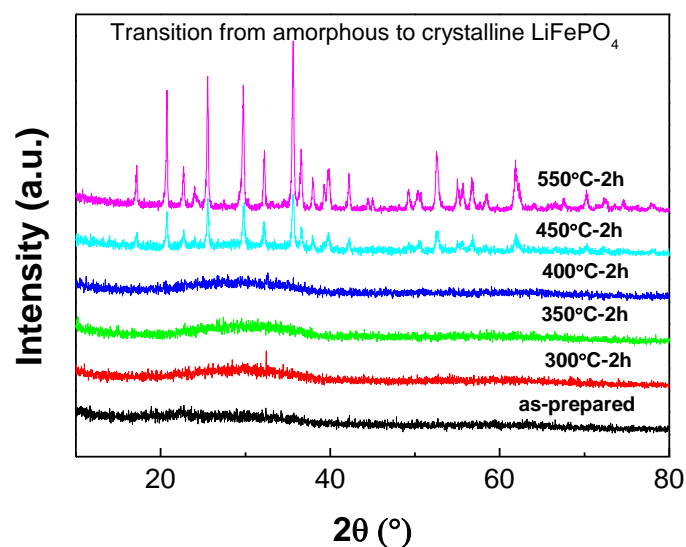


Figure 3.4.4 XRD patterns of amorphous LiFePO₄ sintered at various temperatures in Ar/H₂ atmosphere. The transition process from amorphous to crystalline LiFePO₄ can be observed.

Figure 3.4.5 shows SEM micrographs of amorphous FePO₄ obtained after precipitation, after sintering at 400 °C and amorphous LiFePO₄ after lithiation, respectively. In spite of their amorphous properties, particles are still distinguishable with size of 20~50 nm. Sintering at 400 °C or lithiation does not lead to the particle growth. The BET analysis gives the surface area of 58.13 m²/g and 56.19 m²/g for amorphous FePO₄ and amorphous LiFePO₄, respectively.

TEM and HRTEM images of amorphous FePO₄, amorphous LiFePO₄ and crystalline LiFePO₄ obtained by sintering at 550°C in Ar/H₂ atmosphere are shown in Figure 3.4.6. The amorphous properties of FePO₄ and LiFePO₄ were confirmed by HRTEM (no visible lattice fringe) and SAED patterns. The particle sizes of

amorphous FePO₄ and LiFePO₄ are around 50 nm. As shown in TEM and HRTEM, crystalline LiFePO₄ can be obtained by heating the amorphous LiFePO₄ in Ar/H₂ atmosphere at 550 °C. The particle size is grown to 100~200 nm after heating.

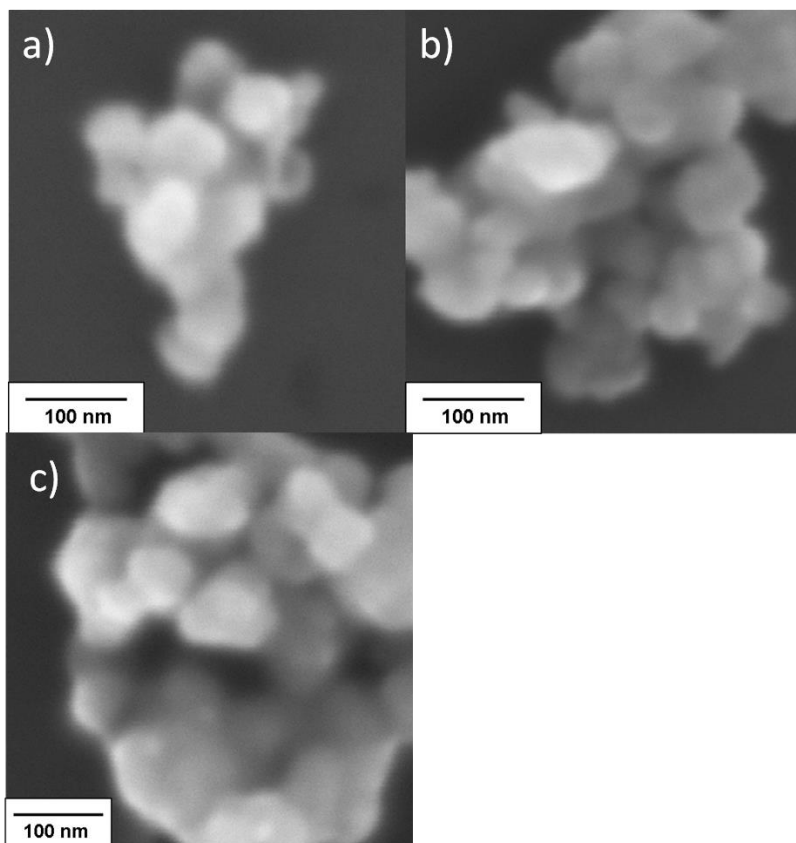


Figure 3.4.5 SEM images for a) amorphous FePO₄, b) amorphous FePO₄ sintered at 400 °C, c) amorphous LiFePO₄.

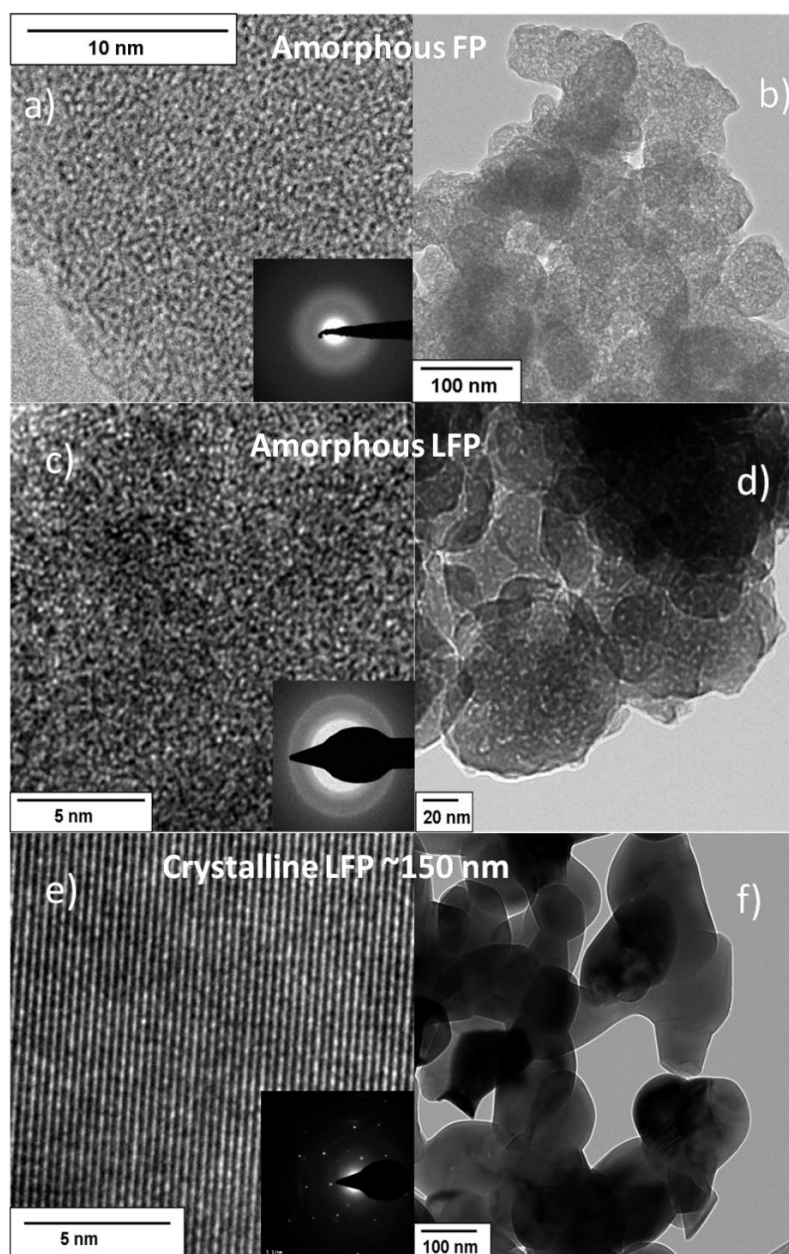


Figure 3.4.6 TEM images (b, d, f) and HRTEM micrographs (a, c, e) for amorphous FePO_4 (a, b), amorphous LiFePO_4 (c, d) and crystalline LiFePO_4 (e, f) obtained by sintering amorphous one in the Ar/H_2 atmosphere. The insets in (a, c) is SAED patterns for amorphous FePO_4 and amorphous LiFePO_4 , which indicates the amorphous properties of these materials. The inset in (e) is SAED pattern for crystalline LiFePO_4 with particle size of ~ 150 nm.

3.4.3.2 Electrochemistry of amorphous LiFePO_4

The charge and discharge profiles for amorphous LiFePO_4 were shown for the

first time at 0.01C rate (1C=170 mA/g) with electrochemical window of 2-4 V for the first three cycles (Figure 3.4.7). Even at such low current, only ~0.6 lithium can be reversible intercalated. The S-shaped charge and discharge curves instead of voltage plateau are observed, which indicates single phase regime of lithium intercalation. The profiles of charge and discharge curves for amorphous LiFePO₄ are very similar to the amorphous FePO₄ previously reported in literatures.¹²³

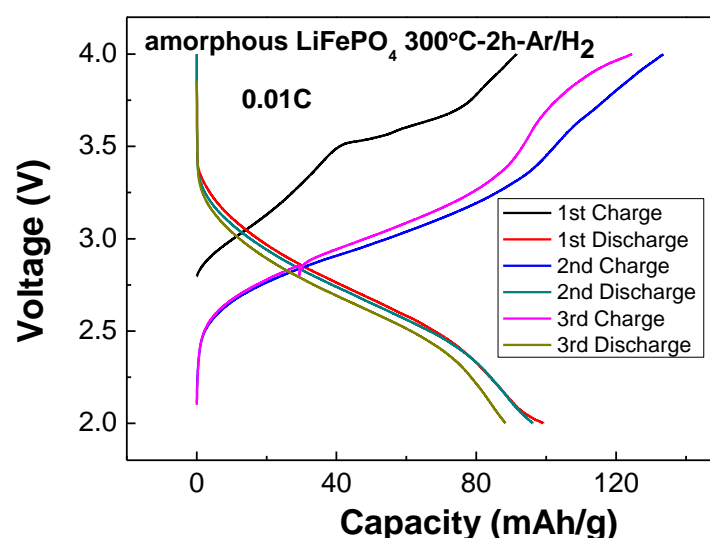


Figure 3.4.7 Charge and discharge profiles for amorphous LiFePO₄ heated at 300 °C for the first three cycles at 0.01C rate.

3.4.4 Conclusions

In order to systematically investigate the size effects of LiFePO₄, not only nanocrystalline LiFePO₄, but also amorphous LiFePO₄ was prepared. Both amorphous FePO₄ and LiFePO₄ were prepared by the precipitation method and characterized by XRD, TG/DSC, SEM, TEM and BET. Heat treatment of amorphous LiFePO₄ at high temperature (550°C) leads to LiFePO₄ nanocrystalline particles. For amorphous LiFePO₄, the S-shaped charge and discharge curves instead of voltage plateau were found, suggesting single phase regime of lithium intercalation.

3.5 Conclusions of Chapter 3

In this chapter, the synthesis and electrochemical performance of LiFePO₄ were investigated. Carbon-coated single crystalline LiFePO₄ nanowires have been successfully prepared by the electrospinning method. These thin nanowires are single-crystalline with growth orientation in *c* direction, and are covered by a 2-5 nm carbon layer on the surface. Such unique morphology of LiFePO₄ leads to good electrochemical performance and excellent cycling stability. On the other hand, in order to study size effects, nanocrystalline LiFePO₄ and amorphous LiFePO₄ were synthesized by surfactant-assisted polyol method and precipitation method, respectively. Using the OL-assisted polyol method, the size of the particles can be controlled by adjusting experimental parameters, such as the ratio of surfactant to TEG, the concentration of the precursors, the reaction time and the CNT addition. LiFePO₄ particles prepared by this method and post heat-treated at 700 °C show excellent rate performance and cycling stability. In terms of electrochemical performance, surface coating proved more important than particle size. Electrochemical performance of amorphous LiFePO₄ was investigated for the first time, and the sloped-typed discharge curve at low current density indicates solid solution behavior.

Chapter 4

Size effects on lithium storage in LiFePO₄

4.1 Introduction

Thermodynamic equilibrium behavior of LiFePO₄, more specifically the size effects in LiFePO₄ are of great importance for the understanding of its behavior. The firstly established size effect was a report on the size-dependent lithium miscibility gap in nanoscale LiFePO₄.¹²⁴ The electrode reaction of LiFePO₄ is predominated by the two phase coexistence of Li_αFePO₄ and Li_{1-β}FePO₄ with narrow single phase regions ($0 < x < \alpha$ and $1 - \beta < x < 1$) which is close to stoichiometric end members at room temperature.¹²⁵ The narrow single phase regions were first experimentally confirmed by Yamada's group through careful XRD investigation.²⁷ Further study on isolated solid solution phase Li_αFePO₄ and Li_{1-β}FePO₄ with different particle sizes performed by the same group confirmed the single phase range ($\alpha=0.056$, $\beta=0.12$ for 40 nm LiFePO₄).¹²⁶ Chiang et al. observed a systematic miscibility gap shrinkage in pure LiFePO₄ with reduction of particle size for nanoscale LiFePO₄ by XRD, charge-discharge profiles and PITT technique.¹²⁴ This study predicts that the miscibility gap will completely disappear below a certain critical particle size (15nm at room temperature). Afterwards, Masquelier et al. for the first time observed single phase behavior at the whole lithium range by *in situ* XRD technique for 40 nm LiFePO₄ nanoparticles obtained by a low temperature precipitation method.¹²⁷ However, it is not only the particle size but also high degree of disorder that lead to such single phase behavior for the whole lithium content.¹²⁷ Besides the particle size, there are also other parameters which influence the miscibility gap, for example, temperature,²⁵ cation-doping,¹²⁸ overall compositions¹²⁹ and carbon coating.¹³⁰ Masquelier et al.²⁵ found experimental evidence of total single phase Li_xFePO₄ ($0 \leq x \leq 1$) for temperatures higher than 450 °C, as well as two new metastable phases at room temperature with composition of Li_{0.75}FePO₄ and Li_{0.5}FePO₄ (confirmed by the XRD refinement). Chiang et al. also observed the shrinkage of the miscibility gap

with increase of temperature and for cation-doped LiFePO₄ of the same size.¹²⁸ Using neutron diffraction as well as modeling of the diffuse interface, Wagemaker et al. showed that the miscibility gap not only shrinks with reduction of particle size, but also strongly depends on the overall composition.¹²⁹ Zaghbi et al. found that carbon coating can also limit the single phase range of LiFePO₄.¹³⁰ Taking into consideration all the present studies, size effects on miscibility gap in LiFePO₄ are still not completely clear and needs further investigation.

Metastable materials have drawn considerable attention due to their small transport lengths and separation distances similar to fluids.¹³¹ Metastable materials include not only nanocrystalline but also amorphous materials, which can be treated as an extreme case of nanocrystalline ones where grain sizes are reduced to atomistic dimensions and the whole material loses its long range order.¹¹⁶ Compared to the bulk materials, metastable phases have several special properties. One typical example is a decrease of the melting point¹³² of nanocrystals compared to macroscopic single crystals, because of increased Gibbs energy. Additionally, defect chemistry of metastable materials is also different due to variation of the defect-chemical mass action constants.¹³³

Size effects on chemical potential are of importance in electrode materials, as chemical potential is related to the cell voltage in a battery system. The chemical potential of a component, for example, Li potential in the lithium intercalation compound, can be predicted thermodynamically.¹³³ Regarding battery systems, the reversible OCV (or e.m.f.) is determined by the difference of Li potential in the lithium foil and lithium intercalation compound (LiX). In other words, it is feasible to measure the lithium potential just by monitoring the OCV of the cell (LiX//Li). The most appropriate example is the observation and explanation of excess potentials in amorphous RuO₂.¹¹⁶

It is significant to investigate lithium potential variations for more complex and applicable systems, for example, metastable LiFePO₄. In LiFePO₄, Li can be exchanged freely, and FePO₄ maintains its stable crystal structure. Consequently, we can treat LiFePO₄ as a pseudo binary system (LiX). A number of studies on the

lithium potential variations for nanocrystalline LiFePO₄ are available.^{122, 132} A slight enhancement of OCV of nanocrystalline LiFePO₄/FePO₄ two phase plateau was observed by several groups.^{124, 134} Lee et al. measured the OCV values of half-discharged cell with long relaxation time (100 h) for nano-Li_{0.5}FePO₄ and bulk-Li_{0.5}FePO₄, and found the OCV increases by ~8 mV.¹³⁴ Similar results were reported by Meethong et al.¹²⁴. They measured OCV from a half-charged cell followed by a long-time relaxation and found a two phase plateau voltage increase by 3~7 mV.¹²⁴ However, such measured OCV values only from half-charged or half-discharged electrodes are not always obtained from equilibrium states, as hysteresis between charge and discharge often occurs.¹³⁵ The OCV values are also found to be influenced by the surface energy value and particle size geometry as shown by Wagemaker et. al. using thermodynamic analysis of various LiFePO₄/FePO₄ cases.¹³⁶ Additionally, particle size distribution and the variation in the local chemical potential of lithium need to be taken into account, which makes the situation far from being clarified.

The main objective of this chapter is to investigate the size effects on lithium storage in LiFePO₄. First of all, the miscibility gap variation as function of particle size, especially comparison of nanocrystalline case and amorphous case is important. Afterwards, focus will be shifted to the lithium potential variations in the nanocrystalline and amorphous LiFePO₄. Lithium potential variations for metastable phases (nanocrystalline vs. amorphous phase) considering single phase regime and two phase regime are predicted. Furthermore, nanocrystalline LiFePO₄ with different particle sizes and amorphous LiFePO₄/FePO₄ are considered from a thermodynamic point of view. Consequently, a deeper conceptual insight of LiFePO₄ as cathode materials is aimed at that may open doors for the investigation of other cathode materials.

4.2 Experimental

Synthesis and materials: Nanocrystalline LiFePO₄ and amorphous LiFePO₄ were prepared by surfactant-assisted polyol method and precipitation method, respectively.

The detailed information on synthesis of LiFePO₄ was described in the Chapter 3. Crystalline FePO₄ with hexagonal structure was obtained by heating of commercial amorphous FePO₄ at 550 °C for 12 hours in air. Commercial carbon-coated LiFePO₄ (particle size around 200 nm, carbon content about 1 wt%) was purchased from Advanced Lithium Electrochemistry Co., Ltd, Taiwan.

Characterizations: Potentiostatic intermittent titration test (PITT) was performed as follows: a “staircase” voltage profile with a 5 mV voltage increment / decrement (each titration was stopped when the current reached around $\sim C/20$) was applied, and the response of current *vs* time was recorded at each constant potential. Galvanostatic intermittent titration techniques (GITT) is performed as follows: the 1/20 C current was used for charging and discharging the samples for 1 hour followed by a 10-30 hours waiting time leading to the relaxation to equilibrium state as a function of different lithium contents. Cyclic voltammetry was performed with Voltalab system (D21V032, Radiometer Analytical SAS, France) on Swagelok-type cells.

4.3 Size effect on the miscibility gap of LiFePO₄

LiFePO₄ is a typical first order phase transition material, in which the nucleation and growth of the second phase will occur during the phase transition process. In this work, PITT is applied to semi-quantitatively investigate different lithium intercalation regimes, e.g. single phase regime or two phase regime, as well as miscibility gap variation as function of the sizes for amorphous LiFePO₄ and crystalline LiFePO₄ with different particle sizes.

A “staircase” voltage profile (black curves in Figures 4.1) was carried out with a 5 mV voltage increment (for the charge process) or decrement (for the discharge process). The response of current *vs* time was recorded at each constant potential (red curves in the Figure 4.1). On the one hand, the appearance of plateau in the voltage curves (black curves, in Figure 4.1) can qualitatively demonstrate two phase coexistence of LiFePO₄ and FePO₄. On the other hand, different lithium intercalation regimes (single phase *vs.* two phase) can be deduced from the difference of current relaxation time scales and shape of the current curves as suggested by Meethong et

al.¹²⁸. In the single phase region, the current relaxation is fast, and the shape of relaxation curves at each constant voltage step is similar to each other. In the two phase region, rate-limiting step is phase transformation instead of diffusion, the local maximum (minimum) in the $I(t)$ curves is observed, as well as a voltage plateau in the $E(t)$ curves.

For amorphous LiFePO₄, the whole range of diffusion-like current relaxation profiles for both charge and discharge process (red curves in Figure 4.1 a) and b)), demonstrates single phase regime (solid solution behavior) for the lithium intercalation, which means absence of any miscibility gap for the amorphous LiFePO₄.

4. Size effects on lithium storage in LiFePO₄

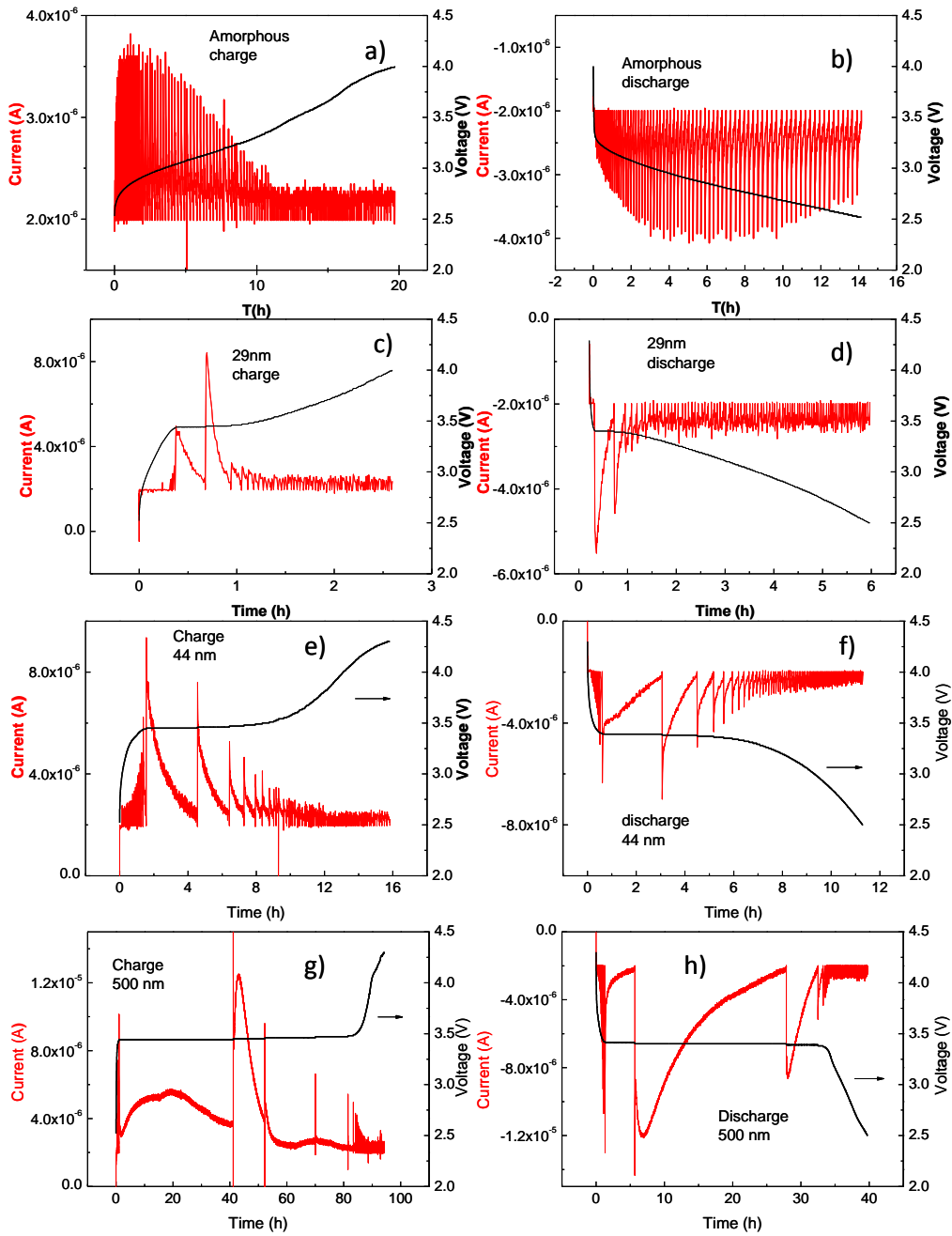


Figure 4.1 PITT measurements on LiFePO₄ with different particle sizes (29 nm, 44 nm and 500 nm) and crystallinity (crystalline and amorphous LiFePO₄).

Commercial carbon coated LiFePO₄ with particle size around 500 nm was chosen for comparison with nanocrystalline LiFePO₄ prepared by the surfactant-assisted polyol method with different sizes. For commercial LiFePO₄, phase transformation occurs, resulting in a local maximum in the $I(t)$ curves, unlike in a single-phase diffusion model. The comparison of $I(t)$ curves of different LiFePO₄

sizes in Figure 4.1, clearly indicates that with decreasing particle size, the width of the two phase region reduces. The same phenomenon, shrinkage of the miscibility gap with decrease of the particle size, was also reported by other research groups.^{124, 125}

4.4 Lithium potential variations for metastable LiFePO₄

Lithium potential variations for both nanocrystalline materials and amorphous materials are strongly related to reaction mechanism of lithium intercalation, such as single phase regime and two phase regime. In principle, for curved metastable materials, the capillary pressure effect $(2\gamma/r)V$ is an effective tool to predict the lithium potential variations, with γ , r and V being effective surface tension, effective radius, and partial molar volume of lithium or mole volume of the phase, respectively. Regarding nanocrystalline materials, in the single phase regime, the excess lithium potential can be described as $(2\gamma/r)V_{Li}$, where V_{Li} is partial molar volume of lithium in the phase. For the two phase storage mode, calculating lithium potential is more straightforward according to the $EF = -\Delta_R G^0$, with E , F , $\Delta_R G^0$ being reversible cell voltage (OCV), Faraday constant, and Gibbs free energy of reaction. The excess lithium potential is hence determined by $(2\gamma_1/r_1)V_1 - (2\gamma_2/r_2)V_2$, as for a phase transformation, one refers directly to the chemical potentials of involved phases, (V_1 and V_2 are molar volume of phase 1 and phase 2). In this situation, if one phase is macrosized (e.g. phase 2) instead of nanocrystalline, as the special case of RuO₂/LiRuO₂,¹¹⁶ then the final excess lithium potential will be $(2\gamma_1/r_1)V_1$. On the other hand, for amorphous materials, it is a rough estimate to apply the capillary pressure correction but with the particle size r being replaced by atomistic size (r_0).¹³³ Alternatively, the loss of long-range order can also be connected with the free melting enthalpy at room temperature.¹¹⁶ In the two phase regime, the excess lithium potential can be described either by free melting energies or by the difference in the surface tensions, i.e. $\Delta_m G_1 - \Delta_m G_2$, or $(2\gamma_1/r_0)V_1 - (2\gamma_2/r_0)V_2$. This can be also extended to other special cases, for example, if only one phase is amorphous phase, and the other phase is nanocrystalline or macrocrystalline. In the single phase mode, however, we have to interpret the excess lithium potential from the defect chemistry point of view.

When lithium intercalates into a material, assuming lithium interstitial and electron form simultaneously, $Li_i^x \rightleftharpoons Li_i^\bullet + e'$. As a result, the excess lithium potential is determined by excess formation energies of both ionic defects and electrons. These quantities can differ a lot in the amorphous state from the microcrystalline state. The excess lithium potentials for various metastable cases are summarized in Table 4.1.

Table 4.1 Excess lithium potential for various metastable cases (colon indicates two phase coexistence).

nano 1 (single phase)	nano 1: nano 2		nano 1: macro 2
$\frac{2\gamma_1}{r_1} V_{Li,1}$	$\frac{2\gamma_1}{r_1} V_1 - \frac{2\gamma_2}{r_2} V_2$		$\frac{2\gamma_1}{r_1} V_1$
amorphous 1 (single phase)	amorphous 1 :amorphous 2	amorphous 1 :nano 2	amorphous 1 :macro 2
$\mu_{Li}^{ex} = \mu_i^{ex} + \mu_n^{ex}$	$\Delta_m G_1 - \Delta_m G_2 \approx \frac{2\gamma_1}{r_0} V_1 - \frac{2\gamma_2}{r_0} V_2$	$\Delta_m G_1 - \frac{2\gamma_2}{r_2} V_2 \approx \frac{2\gamma_1}{r_0} V_1 - \frac{2\gamma_2}{r_2} V_2$	$\Delta_m G_1 \approx \frac{2\gamma_1}{r_0} V_1$

$\gamma_{1,2}$ = surface tension of phase 1, 2

$V_{1,2}$ = mole volume of phase 1, 2

$V_{Li,1}$ = partial molar volume of Li in phase 1

$r_{1,2}$ = particle size of phase 1, 2

r_0 = atomistic size

$\Delta_m G_{1,2}$ = melting free enthalpy of phase 1, 2

μ_i^{ex} = excess chemical potential of Li interstitial

μ_n^{ex} = excess chemical potential of electrons

Now let us take metastable LiFePO₄ (nanocrystalline LiFePO₄ with different particle sizes and amorphous LiFePO₄) as an example in order to apply the thermodynamic prediction of lithium potential variations to the experimental results. Firstly, let us focus on nanocrystalline LiFePO₄ with different sizes.

As shown in Figure 4.2, in a typical CV curve for LiFePO₄, V_{ox} and V_{re} represent peak potentials of oxidation and reduction, respectively. $E_{1/2}$ is average voltage between oxidation peak and reduction peak and can be considered to be OCV. The OCV values obtained from CV curves of LiFePO₄ with different particle sizes are summarized in Table 4.2. From the obtained results, it can be concluded that with the decrease of the particle size in LiFePO₄, the cell voltage of LiFePO₄/Li cell also decreases. When the particle size is smaller than 100 nm, OCV decrease is more pronounced. However, in further tests by CV method, it was found that the OCV values obtained by CV measurement are also dependent on the scan rate. When the scan rates are increased, the OCV values also increase, possible due to the non-equilibrium state. However, obtained OCV values from CV can be qualitatively compared with each other in order to get the tentative trend on the OCV vs. particle size behavior. Real OCV values are expected to be lower than the values reported in Table 4.2 if small enough scan rate is applied.

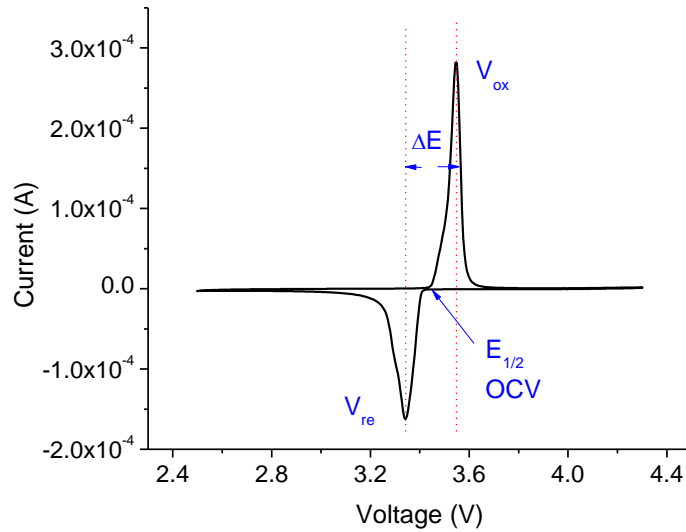


Figure 4.2 Typical CV curve for LiFePO₄ (commercial 500 nm LiFePO₄) with scan rate 0.1mV/s. $E_{1/2}$ is the average potential of reduction peak and oxidation peak, and can be considered to be OCV value.

Table 4.2 OCV values obtained from CV curves for crystalline LiFePO₄ with different particle sizes. (Error bar is 2 mV.)

Particle size	V_{ox}	V_{re}	$E_{1/2}$ (V)
29nm	3.465	3.385	3.425
62nm	3.492	3.363	3.428
150nm	3.523	3.358	3.441
500nm	3.554	3.339	3.446

In this work, we measured the OCV profiles (Figure 4.3) of LiFePO₄ for various particle sizes as a function of different lithium content using GITT technique. 1/20 C currents were used for charging and discharging the samples for 1 hour followed by a 10 hours waiting time leading to the relaxation to equilibrium state as a function of different lithium content. For commercial carbon-coated ~500 nm LiFePO₄, the obtained OCV profile exhibited an almost constant potential of 3.423 V for a majority

of lithium compositions, indicating a typical two phase electrochemical reaction. Similar behaviour is observed for 150 nm sized carbon-free LiFePO₄ particles, except for the lower practical capacity due to lack of current collecting carbon. However, for 44 nm and 37 nm LiFePO₄ samples without carbon coating, the plateau region decreases. Especially for 29 nm sized sample, no plateau is observed. Firstly, it can probably be attributed to a different lithium intercalation mechanism for smaller particles, which was already confirmed by the miscibility gap variation (PITT curves in Figure 4.1). Secondly, 44 nm, 37 nm and 29 nm sized samples were synthesized using the surfactant-assisted polyol method. The residual organic molecules on the surface of LiFePO₄ nanoparticle are not favored for electronic conduction. Moreover, considerable amount of defects can be expected (predominately anti-site defect) due to such a low temperature synthesis route, leading to larger polarization and poor electrochemical performance. Especially for 29 nm LiFePO₄, the 10 hour relaxation time is probably not long enough to achieve equilibrium state. Furthermore, due to small particle sizes, the interface effect becomes more pronounced, and the residual nonconductive carbon or organic molecules can also influence the final OCV values by changing the surface tension (γ) value.

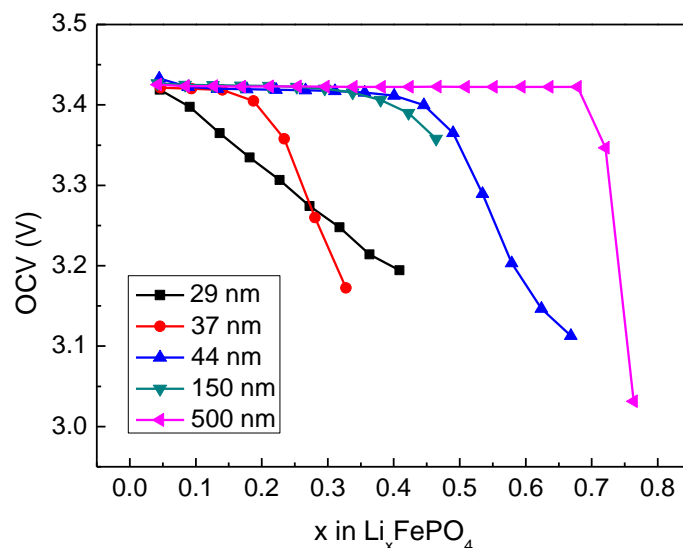


Figure 4.3 OCV profiles for different sized LiFePO₄ as function of lithium content obtained using GITT technique.

GITT is a widely used method to investigate OCV profiles of electrode materials and in most cases 10 hours relaxation time is applied. However, in order to access the real equilibrium as close as possible, longer relaxation times are applied here to measure the OCV values. In the literature, the OCV values are measured by either half-discharging cell following by long-time relaxation or half-charging cell with long-time relaxation. However, the measured OCV values from only half-charged or half-discharged electrodes were not always obtained from equilibrium states, indicated by the hysteresis between charge and discharge¹³⁵ or due to the polarization behavior of charge and discharge processes. As a result, in this work, the OCV for both 50% state of charge (SOC) and 50% depth of discharge (DOD) followed by a long time relaxation (normally 3- 5 days) was measured, which allowed full relaxation and minimized polarization. As show in Figure 4.4, during the relaxation process, the OCV will rise gradually for the discharging process, and drop gradually for the charging process until the stable value is reached. The difference between charging and discharging was not large (see in Table 4.3), thus the average value from OCV-charge and OCV-discharge could be safely taken as an approximation of the reversible OCV value. All of the so-obtained OCV values for nominal Li_{0.5}FePO₄ of different sizes are summarized in the Table 4.3.

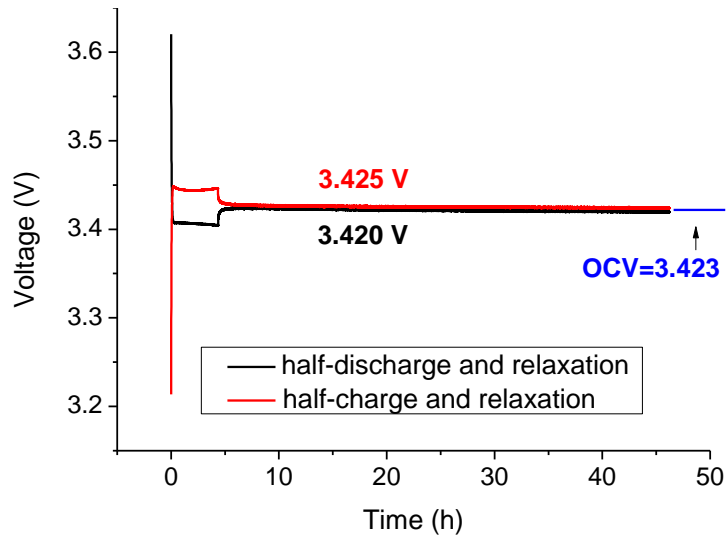


Figure 4.4 Representative voltage vs time curves from direct measurement of OCV while charging and discharging at half capacity with long-time relaxation. (Example is commercial 500 nm LiFePO₄.)

Table 4.3 OCV and surface tension for LiFePO₄ with different particle sizes.

	OCV-50%SOC (V)	OCV-50%DOD (V)	OCV (V)	γ (Jm ⁻²)
29nm	3.408	3.373	3.391	1.15
37nm	3.414	3.410	3.412	0.61
44nm	3.421	3.421	3.421	0.29
150nm	3.427	3.427	3.427	-
500nm	3.425	3.421	3.423	-

OCV values of $3.425\text{V} \pm 0.002\text{V}$ are found for bulk and 150 nm LiFePO₄, while when the particle size is decreased to less than 50 nm, the OCV was shown to decrease (around 10~30 mV). The plot of OCV values vs. $1/r$ is shown in the Figure 4.5. As far as the variation of OCV values are concerned, the effects continuously increase with increased capillary pressure, i.e. ratio of surface tension (γ) to radius (r).

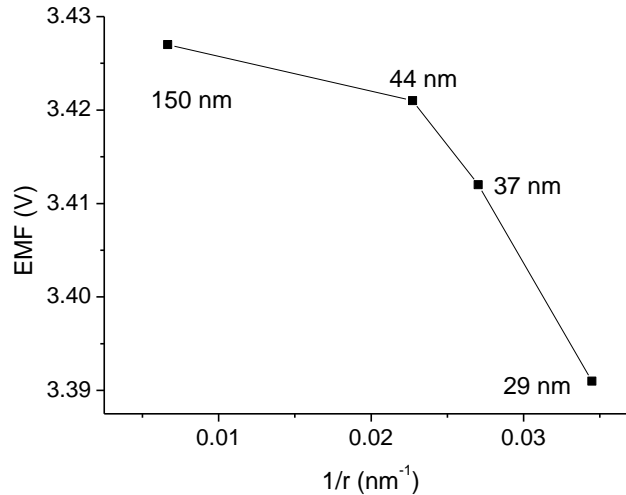


Figure 4.5 The plot of EMF vs. $1/r$ showing that the surface tension varies for the various particle sizes.

Surface tensions can be calculated from the Figure 4.5, and these values are also summarized in the Table 4.3. It indicates that the variation of surface chemistry (γ) is crucial for the OCV variation. The surface tension difference for bulk and 150 nm LiFePO₄ can be neglected, while the surface tension increases dramatically with particle size reduction. Substantial changes in the surface tension are expected according to the preparation procedure.

Assumptions are already given for different cases of metastable LiFePO₄, and in order to understand the obtained results, the lithium intercalation regime for nanocrystalline LiFePO₄ should be determined. In case of bigger LiFePO₄ particles, they are definitely in the two phase regime, which can also be confirmed by PITT curves. However, for small particles, we should be more careful since previous reports propose single phase lithium intercalation regime for 40 nm LiFePO₄. As a result, half-discharging of a 29 nm LiFePO₄ particle was investigated by XRD (Figure 4.6). It demonstrates clearly that a LiFePO₄/FePO₄ phase mixture exists in half-discharged LiFePO₄. Finally, as to nanocrystalline LiFePO₄, we refer to a two-phase situation and the excess e.m.f. (OCV) can be described by $\Delta(2\gamma V_{\text{phase}}/r)$ (Table 4.1). As r and V_{phase} are similar in the two phases, it is essentially $\Delta\gamma$ that decides upon the excess OCV (E^{ex}). The expected effect is a negative E^{ex} (higher chemical potential) which is

experimentally confirmed. The magnitude is on the order of $\Delta\gamma=1\text{J/m}^2$, which is reasonable, particularly for a core-shell mechanism ($\Delta\gamma\approx\gamma_1$).

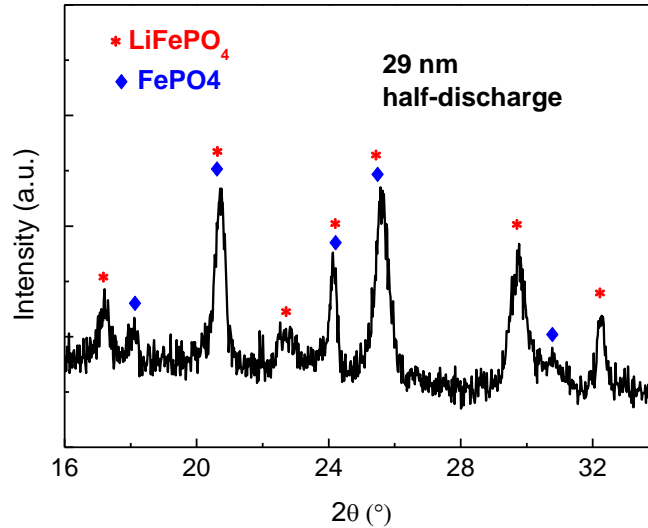


Figure 4.6 XRD pattern of half-discharged LiFePO₄ with particle size of 29 nm, indicating the coexistence of LiFePO₄ and FePO₄.

For amorphous LiFePO₄, the single phase character for lithium intercalation was already confirmed by PITT measurement (Figure 4.1). The comparison of lithium potential between the amorphous and crystalline LiFePO₄ will only be meaningful if both of them are in the single phase regime. For nanocrystalline LiFePO₄, the single phase Li_{1-y}FePO₄ and Li_xFePO₄ only exist on the very narrow range ($x, y < 0.1$) near two end members. For example, for 40 nm LiFePO₄, solid solution single phase Li_{0.074}FePO₄ and Li_{0.891}FePO₄ were experimentally confirmed.¹²⁶

Figure 4.7 displays the OCV curves obtained from GITT for 44 nm nanocrystalline LiFePO₄ and amorphous LiFePO₄ in the single phase regime region. Note that only the first point of nanocrystalline LiFePO₄ belongs to the single phase regime, so only the first point for nanocrystalline and amorphous LiFePO₄ can be compared. It can be clearly seen that the values for the amorphous LiFePO₄ are lower by around 200mV, which means that introduction of metastability would increase lithium potential.

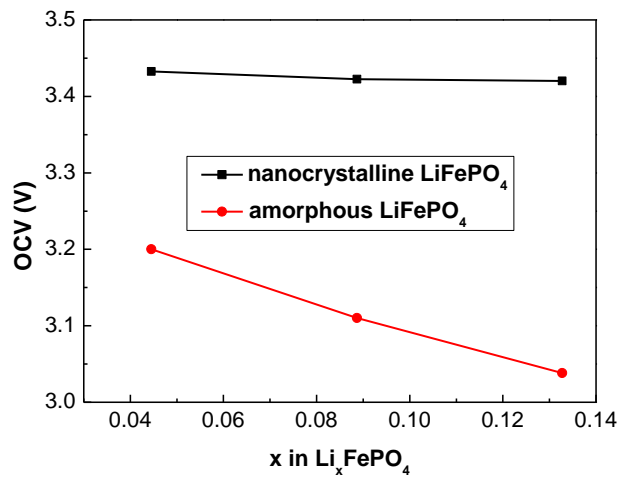


Figure 4.7 OCV curves obtained from GITT for nanocrystalline LiFePO_4 and amorphous LiFePO_4 in the single phase regime region.

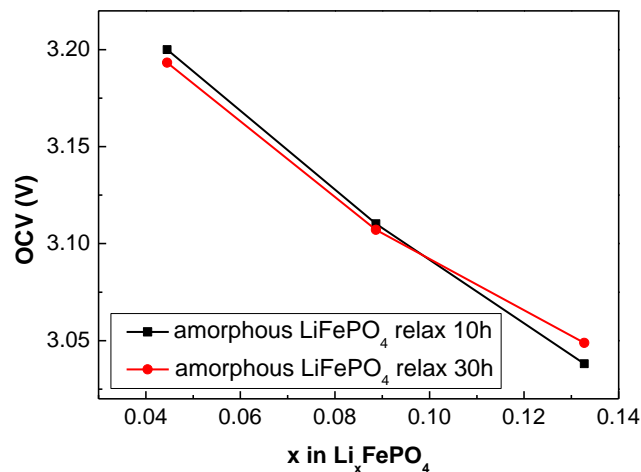


Figure 4.8. OCV curves obtained from GITT for amorphous LiFePO_4 in the single phase regime region for different relaxation times (10 hours and 30 hours).

Figure 4.8 compares OCV values from different relaxation times (10 hours and 30 hours) for amorphous LiFePO_4 . The difference of the OCV (10 h and 30 h) is only around 7mV, which can be easily ignored compared to the OCV difference (around 200 mV) between amorphous and crystalline LiFePO_4 . It shows that 10 hours relaxation time is already long enough in this experiment.

Contrary to LiFePO_4 , crystalline FePO_4 can be found in different polymorphs, e.g. orthorhombic heterosite FePO_4 (the same crystal structure as LiFePO_4) and hexagonal FePO_4 . It is interesting to investigate the influence of different crystal

structures of FePO₄ on the OCV values compared to amorphous FePO₄. Thus, the OCV values of commercial amorphous FePO₄ and crystalline hexagonal FePO₄ are also compared.

Figure 4.9 shows XRD patterns of commercial amorphous FePO₄ and the one after heating at 350 °C and 550 °C. Upon heating at 350 °C, amorphous FePO₄ still maintains its amorphous state; while upon heating at 550 °C, it transforms to hexagonal FePO₄ (JCPDS card No. 50-1635) with a very small amount of impurity phases such as FeO(OH) and Fe₄(PO₄)₃(OH)₃.

Figure 4.10 shows OCV curves obtained from GITT for amorphous FePO₄ and hexagonal FePO₄ obtained from heating amorphous FePO₄ at 550 °C as function of different lithium content. OCV values for the amorphous FePO₄ are higher than those for crystalline FePO₄ for the whole lithium content. Figure 4.11 displays OCV curves of both charge and discharge process obtained from GITT for amorphous FePO₄ and hexagonal FePO₄, confirming the increase of OCV values for the amorphous FePO₄, if an average value from charge and discharge process is taken as final reversible OCV value.

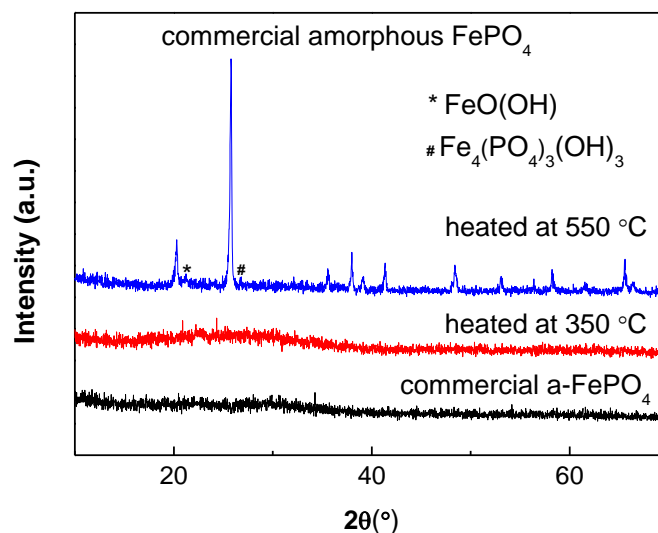


Figure 4.9 XRD patterns of commercial amorphous FePO₄ and after heating at 350 °C and 550 °C.

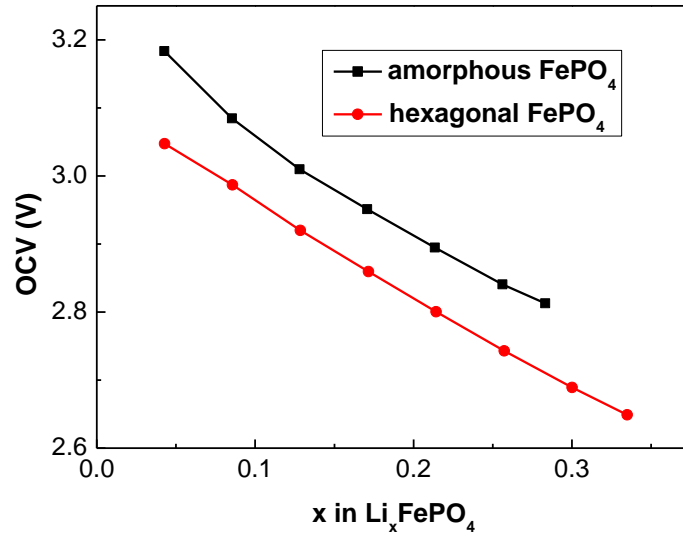


Figure 4.10 OCV curves obtained from GITT for amorphous FePO_4 and hexagonal FePO_4 obtained from heating amorphous FePO_4 at $550\text{ }^\circ\text{C}$ as function of different lithium content.

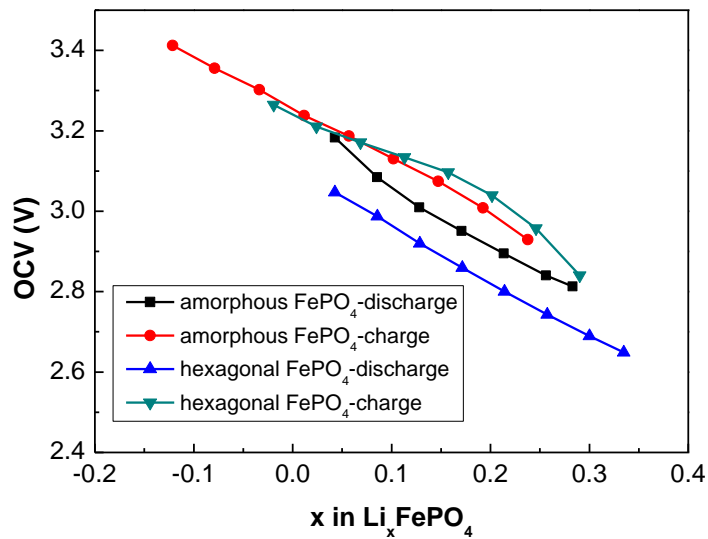


Figure 4.11 OCV curves of charge and discharge process obtained from GITT for amorphous FePO_4 and hexagonal FePO_4 obtained from heating amorphous FePO_4 at $550\text{ }^\circ\text{C}$ as function of different lithium content.

In two phase systems, for the amorphous materials the excess voltage can be related with $\Delta_m G$ (or with an atomistic capillary effect). Here we refer to a single phase regime (Table 4.1). Defect formation in amorphous materials (arrangement of

clusters loss long range order) can be very different compared to nanocrystalline materials. As Li defects should be more easily accommodated in the amorphous structure, since vacancies and interstitials probably favorably form at spots where inhomogeneity stress could be released.¹³³ As a result, the ionic part of $\mu_{\text{Li}}^{\text{ex}}$ is expected to be negative. On the other hand, as electrons might be accommodated less favorably in amorphous structure, even the sign of $\mu_{\text{Li}}^{\text{ex}}$ is a priori not clear. Experimentally, both higher and lower lithium potentials are observed. Compared with crystalline heterosite FePO₄, the excess OCV is negative in the amorphous Li_xFePO₄, while it is positive if compared to crystalline hexagonal FePO₄ structure. As hexagonal FePO₄ is obtained by crystallizing the amorphous material, it is to be assumed that the short range order of the amorphous material is close to hexagonal phase. Then $\mu_{\text{Li}}^{\text{ex}} = \mu_i^{\text{ex}} + \mu_n^{\text{ex}} < 0$, would explain the obtained experimental results qualitatively.

4.5 Conclusions

In this chapter, size effects on lithium storage have been investigated, including size effect on the miscibility gap and size effect on lithium potential variations. For the former, shrinking of miscibility gap with reduction of the particle size was observed. On the other hand, lithium potential variations for metastable phase (both nanocrystalline and amorphous phase) are systematically investigated in the case of single phase regime and two phase regime. As for nanocrystalline LiFePO₄, the reversible OCV values decrease with the particle size reduction, and surface chemistry (γ) is found to be crucial for the OCV variations. The effects continuously increase with increased capillary pressure, i.e. ratio of surface tension to radius (r). For amorphous LiFePO₄, the situation is more complex. Compared with crystalline heterosite FePO₄, the excess OCV is negative in the amorphous Li_xFePO₄, while it is positive if compared to crystalline hexagonal FePO₄ structure, which seems closer to the short range order in the amorphous material. At any rate, ionic and electronic

4. Size effects on lithium storage in LiFePO₄

contributions to $\mu_{\text{Li}}^{\text{ex}}$ will play a crucial role in deciding upon lithium potential variations.

Chapter 5

Size effects on phase transition process in LiFePO₄/FePO₄

5.1 Introduction

At the moment, the mechanism of Li⁺ intercalation/deintercalation in the LiFePO₄ has not been completely clarified. Charge/discharge profiles with voltage plateau are a good indication of a two phase reaction. A variety of models under the names core-shell⁷ (shrinking core¹³⁷), mosaic,²⁸ “new core-shell”,¹³⁸ domino-cascade¹³⁹ and many particles model¹³⁵ etc. have been proposed based on such two phase transition mechanism between LiFePO₄ and FePO₄.

The shrinking-core model¹³⁷ (core-shell model) claimed that during charge (discharge) process, deintercalation (intercalation) of lithium is initiated from the shell to the core. Thus, during charging, a newly formed FePO₄ shell with FePO₄/LiFePO₄ interface will migrate from the particle surface through a continuous shrinking of the LiFePO₄ core. The reverse process happens during discharge. The capacity loss is easily explained by this model, which is ascribed to residual unconverted LiFePO₄ at the center of the particle. Afterwards, the “mosaic model”²⁸ was proposed by Anderson and Thomas, which is essentially similar to the shrinking-core model, but it shows that the intercalation/deintercalation of lithium most probably starts at different nucleation sites. However, recent experimental results (HR-EELS, HR-TEM) invalidated the shrinking-core model.

A “new core-shell” model¹³⁸ has been proposed by Laffont et al. with help of high-resolution electron energy loss spectroscopy (HR-EELS) and consideration of anisotropic 1D lithium transport along the *b* direction within particle of LiFePO₄. As proposed in this model, during the charging process, lithium ions in the center of the particle will be removed outward first while lithium ions insertion will take place at the external part of the sample during discharge. As a result, during charging and discharging, a LiFePO₄ shell around a FePO₄ core is always present. Two end

members (FePO₄ and LiFePO₄) instead of solid solution Li_xFePO₄ were observed in the interfacial region.

The “domino-cascade” model¹³⁹ proposed by Delmas et al. takes into account structural constraints and the influence of the LiFePO₄/FePO₄ reaction interface. For the single particle, once lithium intercalation/deintercalation is initiated, the particle will be either totally charged or totally discharged.

In the many particles model,¹³⁵ Dreyer et al. provided a general explanation of the occurrence of inherent hysteretic behaviour in the behavior of multiple LiFePO₄ particles. They also showed that the observation that the particles are either fully lithiated or delithiated particles is a very consequence of the multi-particle thermodynamics (particle-by-particle charging/discharging mechanism). Owing to the non-monotonic composition dependence of the Li-potential, a situation where the overall Li content is represented by an adequate distribution of Li-free and fully lithiated particle ensemble rather than by homogeneous particle composition is favored.

Although two phase transition process in LiFePO₄/FePO₄ systems by both chemical and electrochemical delithiation at bulk level has been confirmed, the single phase reaction for LiFePO₄ has been reported for the first time by Gibot et al. in highly disordered LiFePO₄ with small particle size (40 nm).¹²⁷ Recently, different types of non-equilibrium single phase scenario during the two phase reactions are confirmed experimentally. Sharma et al. found simultaneous occurrence of solid-solution and two phase reactions through deep discharge in nonequilibrium conditions by real-time *in situ* neutron powder diffraction.¹⁴⁰ Liu et al. found an intermediate single phase within a limited region in electrochemically delithiated sample by soft X-ray absorption spectroscopy and theoretical simulations.¹⁴¹

There are also several simulation studies which confirm the single phase pathway for LiFePO₄ phase transition process. The Gibbs energies for the various compositions were modeled by Malik et al. whereby significant short-range ordering was found.¹⁴² The same authors also stressed the point that even in a single phase path the intermediate compositions are quickly passed throughout, due to the

non-monotonic dependence of the Li potential on composition.

Based on the discussion above, it is evident that there is an ongoing debate on the phase transition mechanism of LiFePO₄. The complex LiFePO₄/FePO₄ phase transition appears to depend strongly on the particle size and morphology. In order to investigate the phase transition mechanism thoroughly, in this chapter, phase transition process in both large single crystals and nanosized LiFePO₄ is studied in detail. At first, the phase transition process in large LiFePO₄ single crystals by chemical delithiation method is investigated. Afterwards, focus will be shifted to the nanostructured LiFePO₄ where staging effect is observed for the first time in half-delithiated LiFePO₄ nanowires. Finally, size-dependent staging structure and phase transition mechanism in LiFePO₄ are discussed in the light of phase transition thermodynamics and kinetics.

5.2 Experimental

Material preparation:

Single crystals of LiFePO₄ were prepared by the optical floating zone technique. Synthesis and characterization details can be seen in Ref.⁹⁷. The crystal (2.5 x 2.1 x 1.3 mm) was cut oriented along the main crystallographic axes.

Carbon-coated LiFePO₄ with particle size of 50nm was prepared by the polyol method with post heat treatment. Synthesis details for as-prepared LiFePO₄ nanoparticles can be seen in Chapter 3. The obtained LiFePO₄ powders were dispersed in the D-glucose water solution with magnetic stirring. After water evaporation, the LiFePO₄/glucose mixture was heated at 700 °C for 12 hours in 5% H₂ / 95% Ar to prepare the carbon-coated LiFePO₄ nanoparticles. 70 nm LiFePO₄ were prepared by ball milling of commercial LiFePO₄ (Advanced Lithium Electrochemistry Co., Ltd, Taiwan) under Ar atmosphere. LiFePO₄ nanowires were prepared by electrospinning method, detailed information can be found in Chapter 3.

Chemical and electrochemical delithiations were performed for LiFePO₄ samples. 10% chemical delithiation was carried out for 70 nm LiFePO₄. LiFePO₄ powders were mixed with suitable amount of nitronium tetrafluoro-borate (NO₂BF₄) in

acetonitrile with magnetic stirring for 24h at room temperature in the glove box. The product was washed several times with acetonitrile before drying under vacuum for 24h (T=80 °C). 50% electrochemical delithiation was performed for 50 nm LiFePO₄ and single crystalline LiFePO₄ nanowires. The charge and discharge cycling was performed two times at 0.1C (10h to fully charge and discharge), and then the fully charged battery was discharged for 5h to obtain Li_{0.5}FePO₄. The battery was disassembled in the glove box under argon atmosphere and the active materials on the Al current collector were washed by anhydrous dimethyl carbonate (DMC) several times for further characterization.

Characterization:

In order to study the delithiation kinetics of large single crystal LiFePO₄, an Olympus PME3 inverted optical microscope was used. The rectangular single crystal with faces parallel to the major axes of the crystal was placed in a custom-made glass container filled with acetonitrile. Bright-field images of the crystal edges at specific positions were taken. Afterwards NO₂BF₄ (stoichiometric amounts for ca. 20 % delithiation of the crystal) dissolved in 150 ml acetonitrile was added. The images were taken at the same positions of the crystal as a function of different time intervals at room temperature. The LiFePO₄/FePO₄ interface and the FePO₄ layer thickness were determined by profiles of the image intensity using Digital Micrograph software (Gatan, Pleasanton, USA).¹⁴³

Secondary Ion Mass Spectroscopy (SIMS) profiles were taken by TOF-SIMS IV from Ion-Tof (primary gun: Ga⁺, 15 keV, 1.8 pA, analysis area 30 μm x 30 μm, sputtering gun O₂⁺, 2 keV, 361 nA, sputtering area 200 μm x 200 μm). Only the positive ions were measured by the mass spectrometer. This surface analysis is performed by service group in Max Planck Institute for Solid State Research.

Aberration-corrected annular-bright-field (ABF) scanning transmission electron microscopy (STEM) was performed using a JEOL ARM 200F microscope operated at 200 keV. A collection semiangle of 12-25 mrad was used with the illumination semiangle of 25 mrad for the best ABF contrast. TEM specimens were prepared by drop-coating the materials individually onto carbon lacey films approximately one

week after the electrochemical treatment, which were further aligned in the microscope at desired orientation via precise goniometry control. ABF is performed in Sendai, Japan.

5.3 Phase transition in large LiFePO₄ single crystals

Up to now, most of investigations on the phase transition mechanism in LiFePO₄ were performed with micro-sized or nano-sized LiFePO₄ particles, and no in-situ macroscopic observation of phase transition process in large single crystal has been reported.

The phase transition process is able to occur through two pathways: electrochemical delithiation and chemical delithiation. In principle, both pathways are similar in terms of their internal mechanism. Since the transport of electrons is faster than the ionic transport, finally Li⁺ transport in the FePO₄ layers will determine the rate of LiFePO₄ delithiation process. However, the major difference between electrochemical and chemical delithiation lies in their the boundary conditions¹⁴³ (Figure 5.1). During electrochemical delithiation, if potentiostatic mode is used, the lithium activity is fixed at the surface; if a galvanostatic mode is applied, a lithium activity gradient exists. On the other hand, during chemical delithiation, due to a large reservoir and quick liquid diffusion, the lithium activity at the surface is fixed. As a result, boundary conditions are similar if potentiostatic electrochemical mode is used.

In this work, by chemical delithiation (NO₂BF₄) of large LiFePO₄ single crystals, FePO₄ growth as a function of reaction time was investigated *in situ* by optical microscopy. Figure 5.2 shows the transition process of blackish LiFePO₄ into the transparent FePO₄ by chemical delithiation in the NO₂BF₄/acetonitrile solution due to following reaction: LiFePO₄+NO₂BF₄→NO₂+FePO₄+LiBF₄. It is clear that the newly formed FePO₄ phase appears as an outer shell of the parent LiFePO₄.

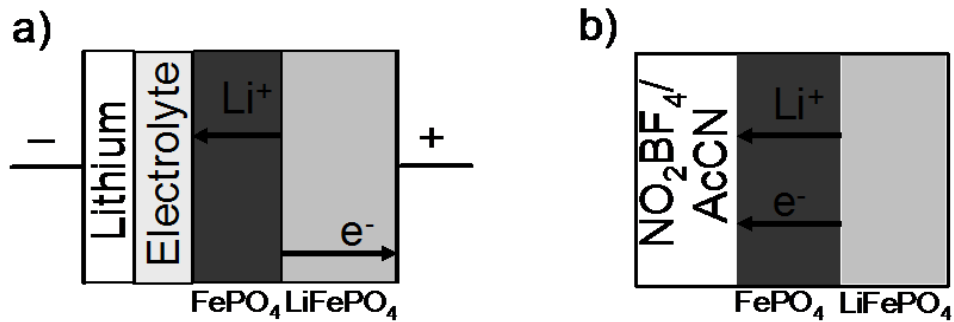


Figure 5.1 a) Owing to the predominant electronic conductivity in both phases, in the electrochemical experiment (galvanostatic charge) Li^+ is transported through the FePO_4 layer while the electron runs towards the positive electrode through the LiFePO_4 phase. b) During chemical delithiation Li^+ and e^- are transported simultaneously through the FePO_4 layer, this process is also determined by ion transport.¹⁴³

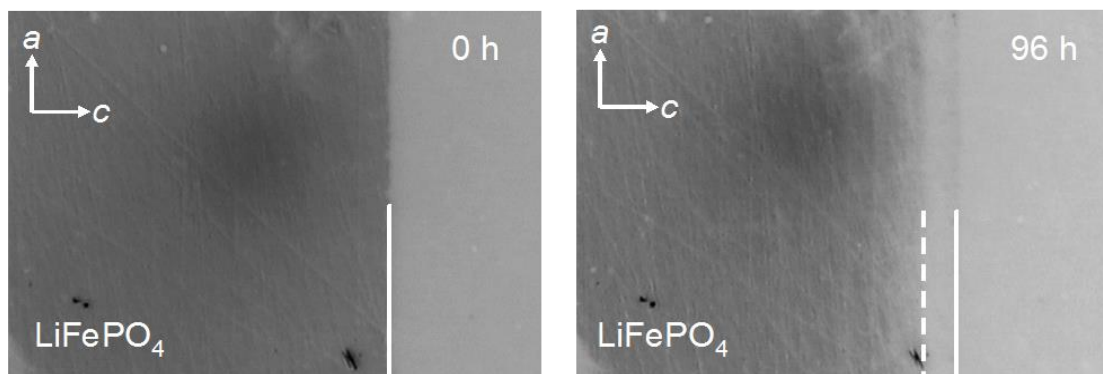


Figure 5.2 Formation of transparent FePO_4 layer at the surface of the blackish LiFePO_4 single crystal after chemical delithiation observed by optical microscopy (negatives of the pictures are shown for better contrast). Solid line marks the solid/solution interface, dashed line the $\text{LiFePO}_4/\text{FePO}_4$ interface. The interface motion could be early followed as a function of time.¹⁴³

Besides this optical microscopy images, depth profiling of partial delithiated single crystal by time-of-flight secondary ion mass spectrometry (TOF-SIMS, Figure 5.3) as well as electro energy loss spectroscopy (EELS),¹⁴⁴ demonstrate the FePO_4

formation is on the outer surface layer of the crystals, which is in agreement with firstly proposed shrinking-core model.¹³⁷

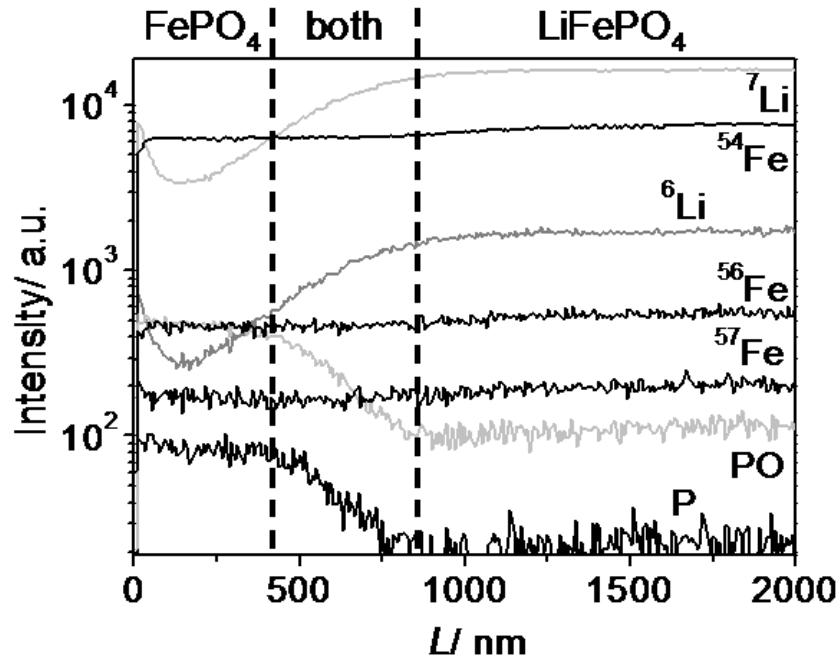


Figure 5.3 SIMS analysis: depth profile of the partially delithiated LiFePO_4 single crystal (investigated area $30 \times 30 \mu\text{m}^2$, crystal size $2.5 \times 2.1 \times 1.3 \text{ mm}$).¹⁴³

The partially chemically delithiated LiFePO_4 single crystal was also investigated by scanning electron microscopy (SEM) after cutting by focused ion beam (as show in Figure 5.4). Deep cracks were observed in the partially delithiated LiFePO_4 crystal in the micrometer scale. On the other hand, the FePO_4 layer is not dense but highly porous. It is the severe strain between the $\text{FePO}_4/\text{LiFePO}_4$ phases that leads to cracks and formation of porous FePO_4 layer.

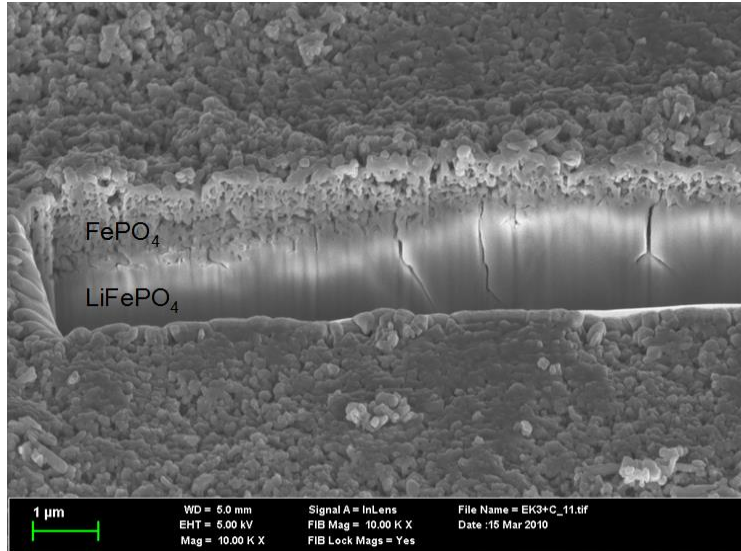


Figure 5.4 SEM image of the partially delithiated LiFePO_4 single crystal. The highly porous FePO_4 layer can be seen at the surface of the crystal.¹⁴³

The growth of FePO_4 layer was additionally studied *in-situ*. After initial time delay, the propagation of the phase boundary was investigated during several days. The thickness of FePO_4 layer was recorded and is shown in Figure 5.5, as a plot of the square of thickness of the FePO_4 layer as function of time.

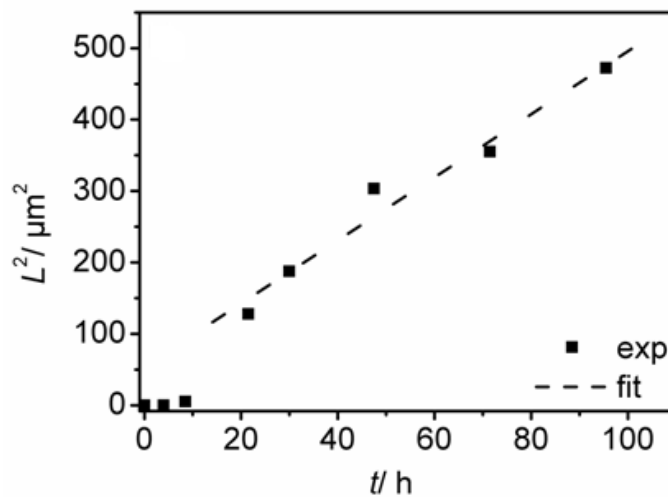


Figure 5.5 Square of thickness L^2 of the FePO_4 layer as a function of time t .¹⁴³

The very first period in Figure 5.5 is typical for an induction period, describing the transition process from stoichiometric LiFePO_4 to maximum lithium deficiency

Li_{1-β}FePO₄. If we ignore the very first induction period, the behavior is square-root-like (i.e., the plot of L^2 vs t is linear). This square-root behavior ($L = \sqrt{2\kappa t}$) is the well-known transport-controlled phase growth law in solid state chemistry. The slope of L^2 vs t gives an effective rate constants κ between 10^{-11} to 10^{-12} cm²/s.

Let us discuss the effective rate constant value κ obtained from the low diffusion. If we consider that Li⁺ is transported only in the pores, a higher κ value should be obtained, since diffusion coefficients in pores are normally in the range of 10^{-5} to 10^{-6} cm²/s.¹⁴³ On the other hand, if Li⁺ is transported in the pure bulk, a pronouncedly lower κ value should be derived. As a result, the lithium transport does occur not only within the FePO₄ layer but also involves the liquid in the pore. The pore/crack network provides a fast diffusion channels interrupted by solid state transport. This phase transition scenario is also of relevance for batteries, if one namely starts from comparatively large crystals, they are down-sized in the first cycle to a sustainable morphology.

5.4 Size-dependent staging and phase transition in LiFePO₄/FePO₄

5.4.1 Direct observation of lithium staging in partially delithiated LiFePO₄

Besides the theoretical calculation and simulation, transmission electron microscopy (TEM) is the most powerful technique to study the phase transition mechanism of olivine phosphate, due to its relatively high resolution enabling the crystal structure and local morphology investigation. Almost all of the proposed phase transition models have supporting TEM evidences. In this section, experimental results available in the literature by conventional TEM will be reviewed and several new observations using advanced STEM-ABF technique will be brought into the game.

5.4.1.1 Literature review on phase transition in LiFePO₄ investigated by conventional TEM technique

Chen et al.⁹⁵ reported that Li_{0.5}FePO₄ (well-crystallized LiFePO₄ pellet,

chemically delithiated) is a mixture of FePO_4 and LiFePO_4 phases. An amorphous interface region between FePO_4 domain and LiFePO_4 domain along a direction was visualized (Figure 5.6).

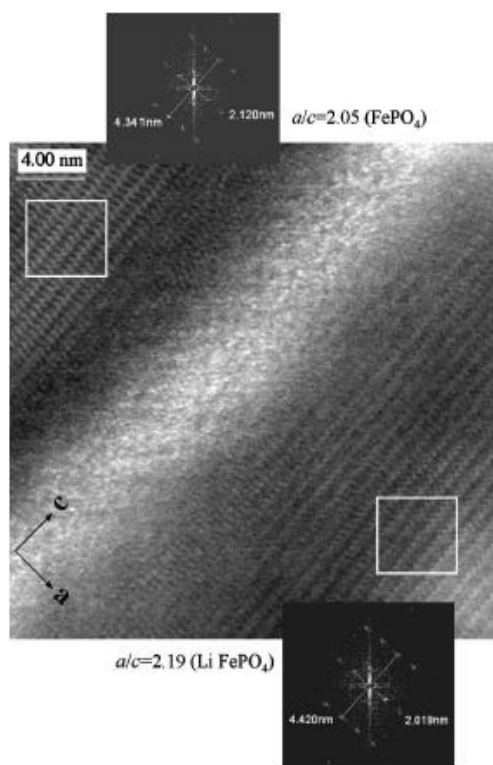


Figure 5.6 HRTEM images of disordered interfacial region between LiFePO_4 and FePO_4 for partially delithiated LiFePO_4 from Chen et al.⁹⁵

Laffont et al. imaged the interface between LiFePO_4 and FePO_4 based on a HRTEM of chemically delithiated 140 nm LiFePO_4 sample (Figure 5.7).¹³⁸ Based on the results, they proposed the “new core-shell” model.

Delmas et al.¹³⁹ investigated 80-150 nm delithiated Li_xFePO_4 ($x=0.41\sim 0.61$, x value was not specifically stated) and did not observe the two phase interfaces. Rather, they found either totally charged or totally discharged particles and proposed “Domino-cascade” model (Figure 5.8).

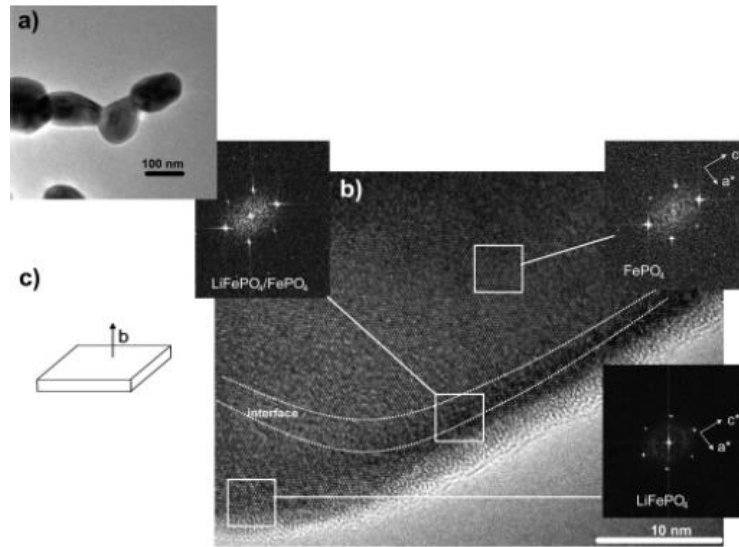


Figure 5.7 TEM results from Laffont's work. (a) TEM and (b) HRTEM imaging of the chemically delithiated sample of $\text{Li}_{0.45}\text{FePO}_4$. The Fourier transforms of the HRTEM imaging enables the determination of the nature of the phase present in the edge, core, or interface of the particle, respectively. (c) Particle Sketch.¹³⁸

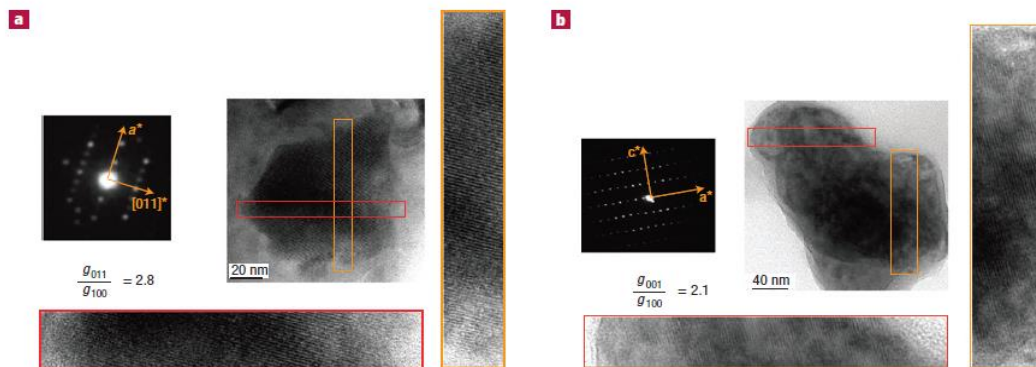


Figure 5.8 TEM images from Delmas's report. High-resolution images of crystallites with their electron diffraction patterns. Magnified views of two parts of these crystallites are also shown in the bottom and on the right. a), $\text{Li}_{1-\beta}\text{FePO}_4$. b), $\text{Li}_\alpha\text{FePO}_4$.¹³⁹

As seen above, the reported conventional HRTEM results lead to different phase transition models depending in particularly on size, composition and nature of delithiation process. Unfortunately, resolution in the conventional HRTEM is relatively low. The key point at present research lies in the improvement of the

resolution of TEM in particularly for direct imaging of lithium ions at atomic resolutions.

5.4.1.2 Observation of staging structure for partially delithiated LiFePO₄ by STEM-ABF technique

The attainable spatial resolution of a conventional TEM is limited to 50 times the wavelength of the fast electrons (close to 2 angstrom) due to the lens aberrations, restricting the direct observation of light atoms at atomic resolutions. Up to now, lithium columns in lithium containing materials (LiCoO₂) have been resolved by focal-series reconstruction method,¹⁴⁵ an operationally-complicated and computationally-expensive method. The idea of incorporating an aberration-corrector⁷¹ to TEM made a great improvement on both atomically-resolved microscopy as well as spectroscopy. Aberration-corrected annular-bright-field (ABF) scanning transmission electron microscopy (STEM) recently provided details of the structure at sub-angstrom resolution, and offered the possibility to resolve atomic columns, even for light elements such as Li.⁷² ABF has been successfully applied to observe lithium ions in spinel-structured LiMn₂O₄ and LiV₂O₄.¹⁴⁶ In this work, this advanced technique is applied to directly observe lithium ions at atomic resolution in LiFePO₄.

Figure 5.9 displays a scheme of the ABF imaging geometry. A fine probe with a spot size less than 1 angstrom scans across the specimen. An annular detector is fixed at the post column, defining a collection semi-angle between 11 to 20 mrad. The advantage of this collection geometry is readily envisaged compared to normal bright-field acquisition that the optical-axis collection, corresponding to the phase contrast conventional high resolution imaging condition, is modified. The ABF micrograph of pure pristine LiFePO₄ in Figure 5.9b directly indicates the lithium atomic sites with the corresponding structural schematic illustrated in the upper inset. Detailed contrast analyses by the line-profile (Figure 5.9c) acquired at the box region (see both ABF micrograph and structural schematic) confirmed the lithium contrast compared to that of the oxygen. Contrast dependence of $Z^{1/3}$ with respect to the

atomic number is revealed⁷². The intensities of O, P and Fe are also shown for comparison. Due to the overlapping of the relatively large atomic radii along the [010] projection, the columns of Fe, P and part of O can not be distinguished.

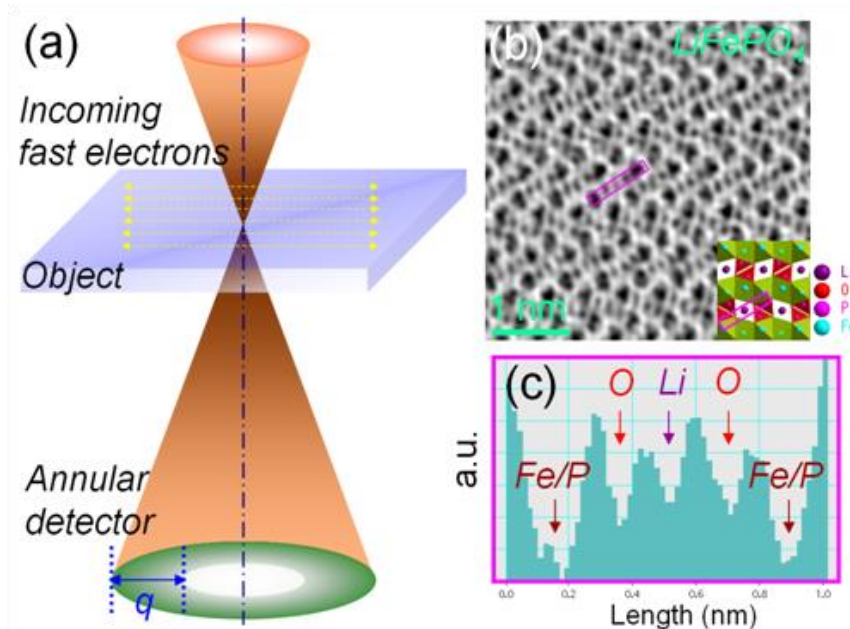


Figure 5.9 (a) Schematic of the annular-bright-field (ABF) imaging geometry. A demonstration of lithium sites within a LiFePO_4 crystal is shown in (b) with the corresponding line-profile acquired at the box region shown in (c) to confirm the lithium contrast with respect to oxygen.¹⁴⁷

As can be seen, the success of ABF technique, provides a feasible way to investigate the phase transition process based on direct observation of lithium. The firstly investigated sample was the LiFePO_4 nanowire prepared by an electrospinning method (more details on this method can be seen in Chapter 3). The morphology of the investigated nanowire is shown in the Figure 5.10. The upper inset is an SEM micrograph, which shows the nanowire with the diameter around 65 nm. The SAED pattern and HRTEM image indicate the single-crystallinity of the LiFePO_4 nanowires. The full-delithiated (FePO_4) and half-delithiated ($\text{Li}_{0.5}\text{FePO}_4$) LiFePO_4 were obtained by an electrochemical method. Electron energy-loss spectroscopy (EELS) shows Fe-L_{2,3} edge spectra for pristine, half-charged and full-charged LiFePO_4 in Figure 5.11.

The increase ratio of L_3/L_2 indicates a systematic alteration of the Fe valence from 2^+ to 3^+ for LiFePO_4 , $\text{Li}_{0.5}\text{FePO}_4$ and FePO_4 .

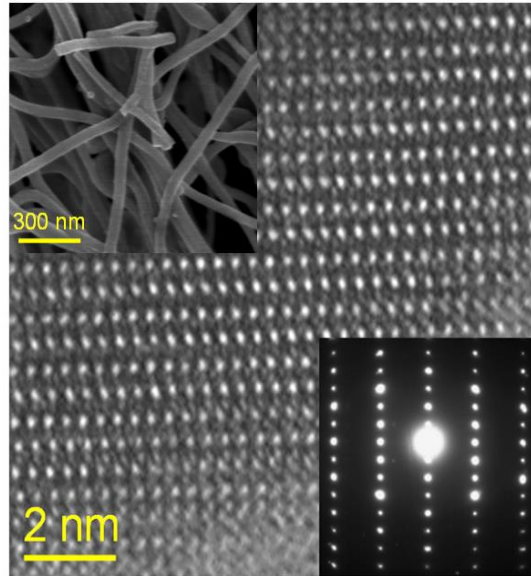


Figure 5.10 High-resolution transmission electron micrograph (HRTEM) reveals the pristine LiFePO_4 lattice with the corresponding diffraction shown in the inset. A scanning electron micrograph is shown in the inset to display the nanowire morphology.

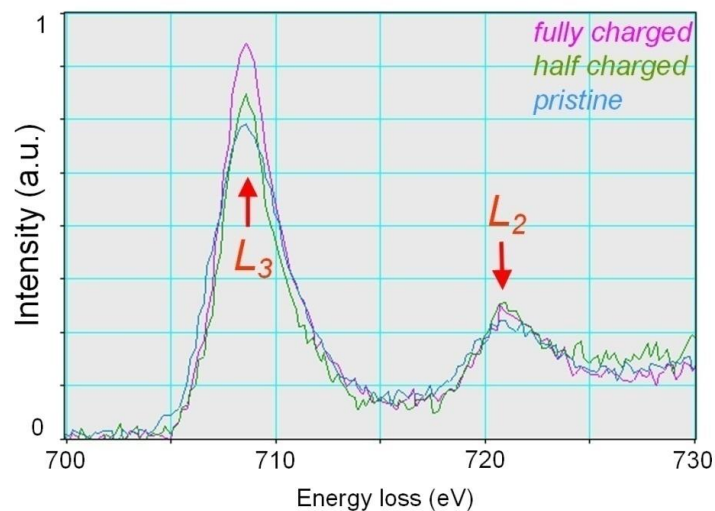


Figure 5.11 EELS comparison of the pristine, half charged and fully charged LiFePO_4 . The enhanced L_3/L_2 ratio after charging indicates a systematic alteration of the Fe valence from 2^+ to 3^+ .

Figure 5.12a shows an ABF micrograph of pristine LiFePO_4 acquired from [010] axis (refer to space group $Pnma$), and the lithium sites are marked by the yellow circles. For fully charged LiFePO_4 , i.e. FePO_4 , in the ABF images (Figure 5.12b), the delithiated sites are marked by the orange circles. The Li-extraction directions are indicated by the red arrows. As for the partially delithiated LiFePO_4 (~ 0.5 mol Li is delithiated), the lithium occupies every second row in the crystal lattice (Figure 5.12c). This phenomenon is very similar to the lithium intercalation into graphite. Schemes of the LiFePO_4 , FePO_4 and $\text{Li}_{0.5}\text{FePO}_4$ structures are shown as insets, respectively.

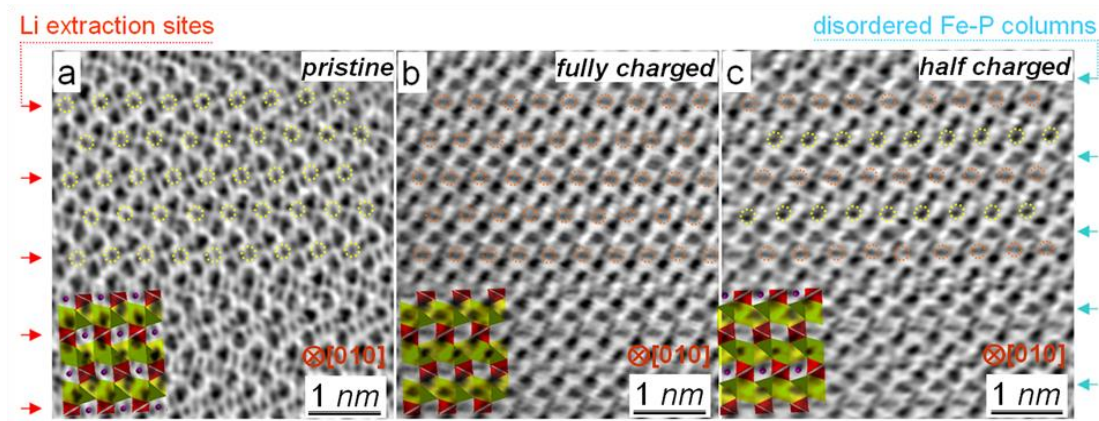


Figure 5.12 ABF micrographs showing Li ions of partially delithiated LiFePO_4 at every other row. (a) Pristine material with the atomic structure of LiFePO_4 shown at inset; (b) fully charged state with the atomic structure of FePO_4 shown for comparison; and (c) half charged state showing the Li staging. Note that Li sites are marked by yellow circles; and the delithiated sites are marked by the orange circles.¹⁴⁷

Within the unit cell, when lithium ions are extracted, the upper nearby Fe-P columns, as indicated by the cyan arrows, display a fuzzy contrast, which indicates a disorder local structure. The atoms do not occupy the original position any more but with a small deviation of $r-r_0$ instead. A faint contrast corresponding to diffused O columns is present close to the vacant places in the rows where Li ions are extracted. This can be related to the above mentioned upper nearby Fe-P column distortion.¹⁴⁷ In Figure 5.12b, for fully charged FePO_4 , the Fe-P distortion was detected as well.

Detailed contrast comparison for lithiated and delithiated states is displayed in Figure 5.13.

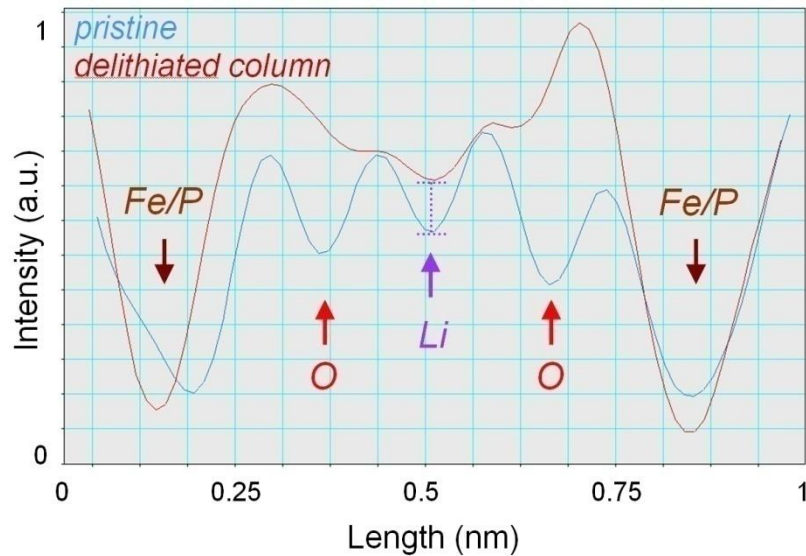


Figure 5.13 Comparison of the ABF contrast for pristine and delithiated materials. The intensity of the Li column shows a significant difference, which directly reflects the amount of lithium remaining in the column after charging.

In summary, the high resolution ABF images demonstrate clearly that a first order lithium staging structure exists for the partially delithiated $\text{Li}_{1-x}\text{FePO}_4$ ($x \sim 0.5$). Such a microstructure has never been observed by conventional HRTEM technique. Although the formation of the staging structure is well known in graphite intercalation compounds and some other layer compounds, i.e. TiS_2 , its appearance for LiFePO_4 was surprising. Staging is generally due to the existence of elastic coherence strain and minimization of the Li-Li repulsive interaction. This long range order adds another degree of complexity for the discussion of phase structure and interface structure.

5.4.2 Size-dependent lithium staging structure

As mentioned in the last section, with the help of STEM-ABF, surprisingly, a pronounced long-range lithium ordering was observed. However, further experimental

and theoretical work has to be done in order to clarify the related fundamental issues, such as origin, stability, formation kinetics of staging structure, as well as the role of the decisive parameters (e.g. particle size, morphology, charge state and preparing method etc.). The Gibbs energies for the various compositions of LiFePO₄ were modeled by Malik et al., whereby significant short-range ordering was found.¹⁴² Recently, a distinct ordering was also observed in the form of an ordered staging interphase at the contact of LiFePO₄ and FePO₄ (LiFePO₄/staging Li_{0.5}FePO₄/FePO₄ three phases coexistence) for the Nb-doped LiFePO₄ with particle size of ~200nm by ABF. The width of this interfacial zone was 2 nm.¹⁴⁸ Afterwards, Sun et al. investigated this LiFePO₄/ stage-II Li_{0.5}FePO₄/FePO₄ three phase coexistence by DFT calculation, and they concluded the staging structure to be kinetically controlled state, which is corresponding to a thermodynamic metastable phase.¹⁴⁹

In this work, in order to investigate the possible size effect on the staging structure, besides nanowires, LiFePO₄ nanocrystals with smaller sizes (50nm and 70nm) compared to reported Nb-doped 200 nm LiFePO₄¹⁴⁸ were investigated.

The dispersion of fine particles down to 25 nm size was not successful for ABF operation, because of the highly overlapping. Therefore, the smallest particle could be investigated by ABF in this work is a carbon-coated 50 nm LiFePO₄ particle. Figure 5.14 shows HAADF and ABF micrographs of an electrochemically half-delithiated LiFePO₄ particle with size of 50 nm, which were acquired at two different areas with (a) and (c) from the center of specimen and (b) and (d) from the edge, respectively. Similar HAADF images were obtained from Figure c) and d) corresponding to the center and edge of the particle, which only show the atomic positions of Fe and P.⁷³ As shown in the Figure 5.14 a) and b), orange and cyan arrows represent Li occupied sites and delithiated sites respectively. The staging structure was observed in the entire nano particle. The diffused contrast pointed by the cyan rows implies distortion of the local structure which related to the electrochemical delithiation. It should be noted that the staging structure throughout the entire particle was also observed on single-crystalline LiFePO₄ nanowire (~ 60 nm).¹⁴⁷

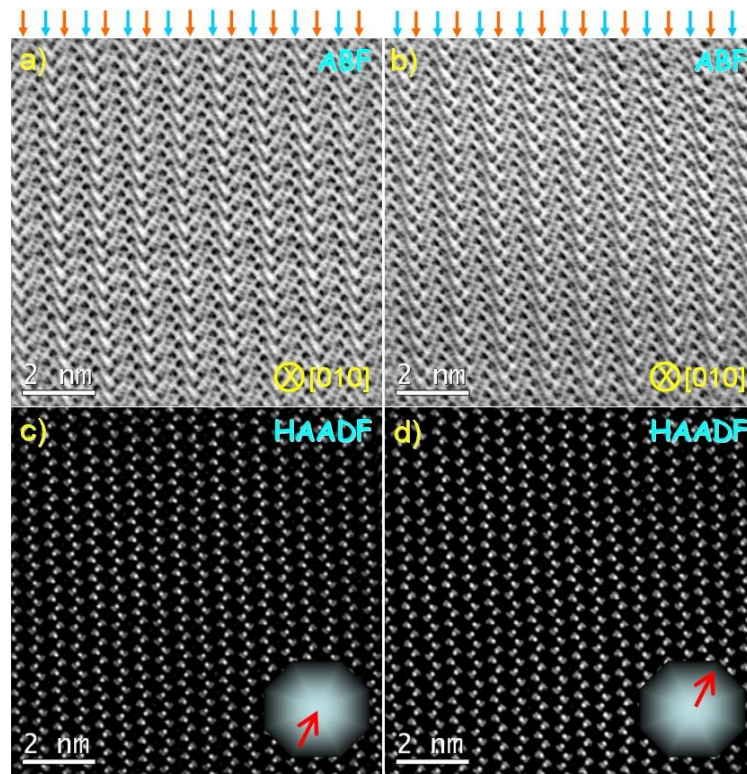


Figure 5.14 HAADF and ABF images of electrochemically half-delithiated carbon-coated 50 nm LiFePO_4 viewed from $[010]$ zone axis. The micrographs were acquired at two different areas with (a) and (c) taken from the center of sample and (b) and (d) taken from the edge. Orange and cyan arrows distinguish atomic rows which have different Li quantities in the projection column.

Figure 5.15 shows the line profiles of the ABF micrographs from the center and edge of the same particle investigated previously (Figure 5.14). Staging structure is confirmed by orange and cyan atomic rows, which have different Li quantities in the projection column. More pronounced difference in lithium quantity appears in the center than at the edge, demonstrating that the decrease of ordering occurs from the center to the edge in one particle. As a result, the staging structure not only appears for the entire particle but also displays slight variation of the local structure from the center to the edge. The origin of the gradual variation of staging structure is not clear yet. It could be probably attributed to the symmetry break by the surface weakening long range order.

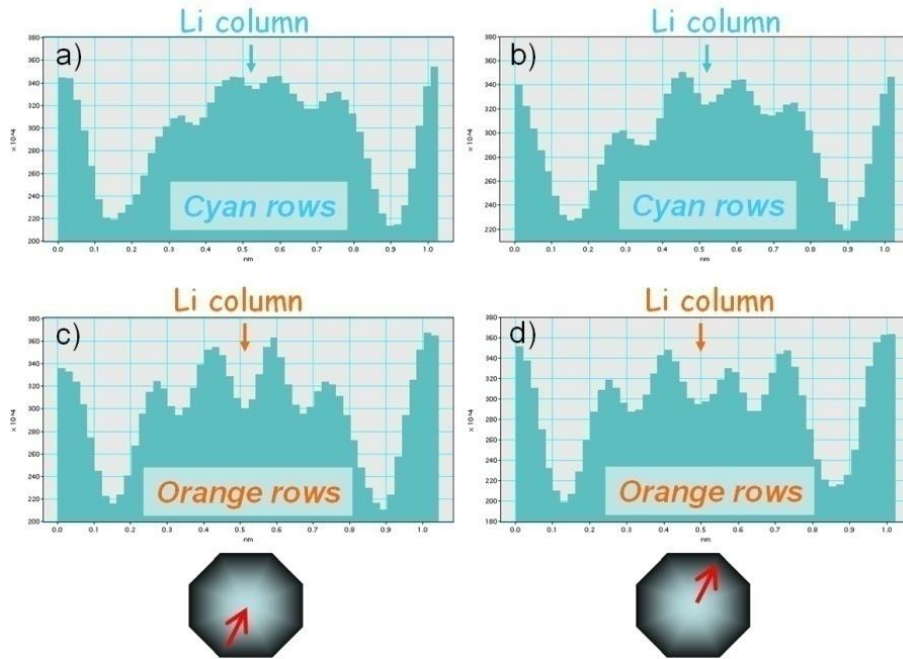


Figure 5.15 Line profiles of the ABF images from the center and edge of the sample. The profiles were acquired at two different areas with (a) and (c) taken from the center of sample and (b) and (d) taken from the edge. Cyan and orange rows indicate different Li quantities.

Another staging situation was observed, when we investigated a ball-milling 70 nm LiFePO_4 sample in the state of 10% chemical delithiation. Figure 5.16 shows an ABF-STEM micrograph viewed from $[010]$ zone axis. ABF images (Figure 5.16 a) as well as the line profiles (in Figure 5.16 f, see the significant difference of Li columns intensity) from three different regions (Figure 5.16 b, c, d), confirm that a staging structure appears as the interfacial region between LiFePO_4 and FePO_4 . Note that in the ABF line profile, image contrast of the dark dots is inverted and shown as peaks. The results here show that the morphology and purity are not decisive factors for the appearance of staging, since the staging structure can be observed in both LiFePO_4 nanowires and nanoparticles, as well as in Nb doped materials. The interfacial staging structure is along the a direction and perpendicular to the b directions, while the phase boundary moves along the c direction. Figure 5.16 indicates curved rather than planar interphase boundaries. In addition, it is improbable that the electron beam radiation

significantly affects the local structure, since no structure changes were observed during the radiation experiments. The results are similar to those reported for 10% delithiated Nb-doped LiFePO₄ sample.¹⁴⁸ A remarkable difference lies in the width of the interphases. For the 70 nm LiFePO₄, the width was around 15 nm (the staging structure is marked by yellow dash lines in Figure 5.16a), while for 200 nm Nb-doped LiFePO₄, it shows a smaller width of 2nm.¹⁴⁸

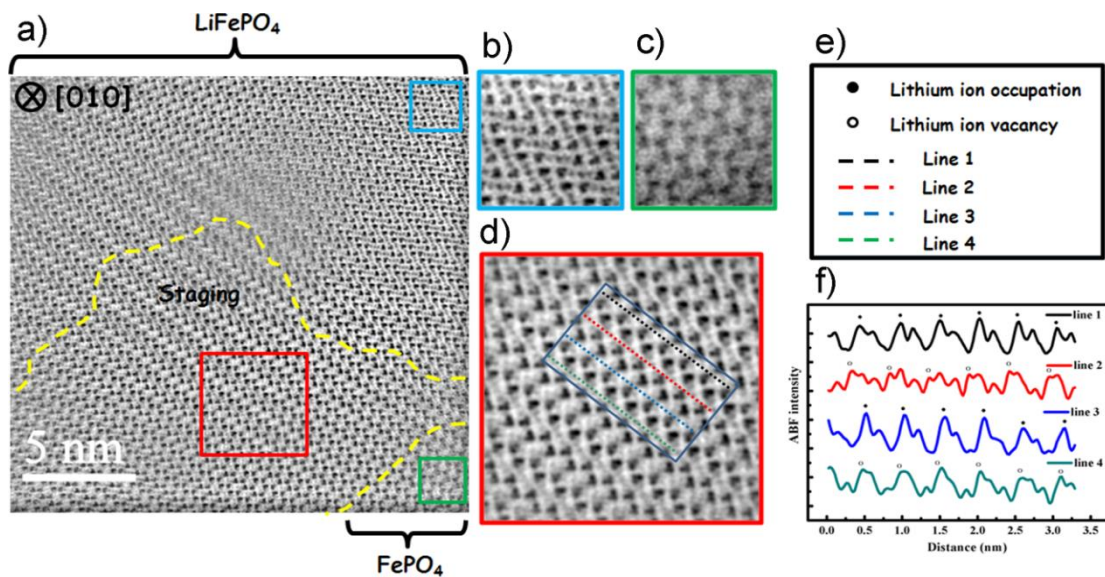


Figure 5.16 (a) ABF-STEM micrographs of ball-milling 70 nm LiFePO₄ viewed at the [010] orientation. The staging region is marked by the yellow dashed lines. (b), (c) and (d) magnifying images of LiFePO₄, FePO₄ and interfacial phase with staging structure, corresponding to blue, green and red squares respectively in (a). (e), (f) the line profiles corresponding to the different colored dashed lines in (d).

Based on the LiFePO₄ samples with different sizes, the size-dependent staging structures are summarized as follows: for small nanoparticle with electrochemically half-delithiation, a homogeneous staging structure throughout the entire particle was observed. On the other hand, in larger nanoparticles, a staging structure was found as a contact interphase between LiFePO₄ and FePO₄, with its width decreasing with increasing particle size.

In terms of homogenous staging structure, the observation of the Li_{0.5}FePO₄

staging structure throughout the entire particle can be understood if the extremely sluggish relaxation of such an intermediate metastable phase is considered. It is reasonable to assume that such ordered structure will show a local minimum in the Gibbs energy as a function of Li-content ($\Gamma(\xi_{\text{Li}})$) curves (see Figure 5.17 a). Regarding additional constraints such as capillary, charge or stress effects, staging structure can even be thermodynamic stable phase ($\text{Li}_{0.5}\text{FePO}_4$ as coexisting phase, Figure 5.17 b). In the first case, the $\text{Li}_{0.5}\text{FePO}_4$ phase will eventually vanish if all the gradients in the chemical potential of Li have disappeared, eventually relaxing towards the two phase mixture. On the other hand, in Figure 5.17b, one of the end-members will disappear but $\text{Li}_{0.5}\text{FePO}_4$ will remain. In Figure 5.17 c, the corresponding Li-potential ($\mu_{\text{Li}}(\xi_{\text{Li}})$ curve) is displayed by obtaining the derivation of $\Gamma(\xi_{\text{Li}})$ curve (Figure 5.17a or b).

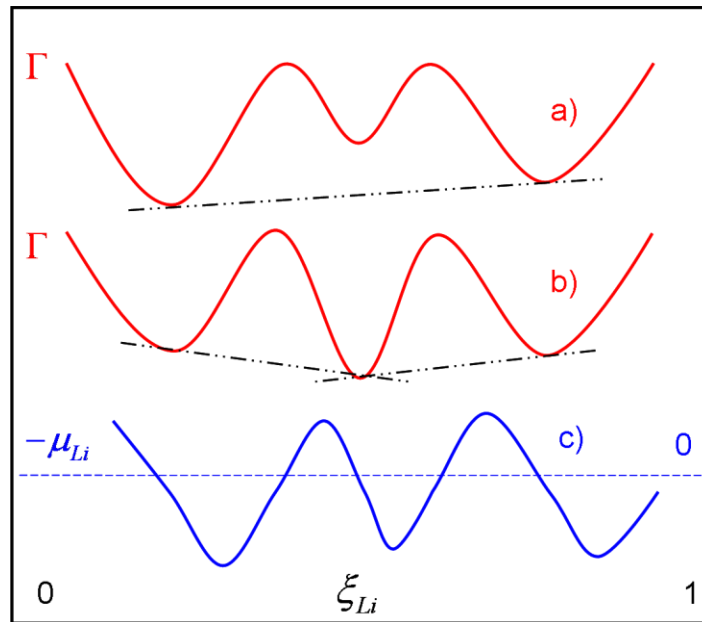


Figure 5.17 (a), (b) Different Gibbs free energy curves in the LiFePO_4 as function of Li content with the existence of low energy staging structure. Γ is the Gibbs energy per number FePO_4 unit and ξ_{Li} is the ratio of number of Li to number of FePO_4 . (c) The chemical potential of Li, owing to the definition of Γ and ξ_{Li} , as derivative of one of above curves.

Besides appearing as homogenous metastable or stable staging structure, Li_{0.5}FePO₄ staging structure also appeared as a contact phase between LiFePO₄ and FePO₄. This morphology may be attributed to a very sluggish redistribution as well, but expressed in terms of a spatial distribution, which is particularly clear if referring to in Figure 5.17c. A non-vanished gradient in the Li-potential would prefer such morphology in particular in the case of Figure 5.17 b. This is then similar to an oxide layer sequence (FeO/Fe₃O₄/Fe₂O₃), when Fe is under a high O₂ partial pressure.

If the staging structure is a thermodynamically metastable phase, then the chemical diffusion coefficient of Li in the corresponding phases is crucial, since it reveals the relaxation kinetics. The extrapolated diffusion coefficients at room temperature for LiFePO₄, Al-doped LiFePO₄ and Si-doped LiFePO₄ large single crystals^{32, 63, 64, 67} are listed in the Table 5.1. Note that the values already include anti-site defects, which reduce effective transport. As shown in the Table 5.1, anisotropy of chemical diffusion coefficients was observed. The extrapolated values of 10⁻¹² cm²/s at room temperature were found along the *b*, *c* axis, and 10⁻¹⁴ cm²/s for the *a* direction in LiFePO₄. There are no available diffusion coefficient values of FePO₄ or staging structure, but we do not expect D^δ in these phases to show extremely lower values. It is also not expected that D^δ will vary by many orders of magnitude with impurity content. If we safely take 100 nm as the diffusion length, a diffusion coefficient of 10⁻¹² cm²/s would lead to a redistribution within 1 minute. In this work, the staging structure can be observed even after half a year, which demands a D^δ value of less than 10⁻¹⁷ cm²/s or a huge transfer resistance for Li at the boundaries to prevent Li redistribution (not expected). As a result, there are two possibilities: either the unmixing energy is extremely close to zero resulting in negligible driving force, or there is a thermodynamic reason for its stability.

Table 5.1 Extrapolated diffusion coefficient of LiFePO₄ and (Al, Si)-doped LiFePO₄ large single crystals at room temperature from the literature.^{32, 64-66}

D ^δ (cm ² /s)	<i>a</i> -direction	<i>b</i> -direction	<i>c</i> -direction
LiFePO ₄	10 ⁻¹⁴	10 ⁻¹²	10 ⁻¹²
Al-doped LiFePO ₄	10 ⁻¹³	10 ⁻¹⁰	10 ⁻¹¹
Si-doped LiFePO ₄	10 ⁻¹⁴	10 ⁻¹²	10 ⁻¹²

Now let us discuss the possibility of staging structure as a low energy solution of the LiFePO₄/FePO₄ coexistence from the thermodynamic point of view. Similar to an ABAB interface forming the junction of AAAA and BBBB, it is reasonable to assume a staging structure for constituting the LiFePO₄/FePO₄ interface. The volume difference between LiFePO₄ and FePO₄ is about 6%, which would result in an arrangement of misfit dislocations or severe coherency strain. From the energy point of view, in order to form an interphase staging structure, the additional energy forming Li_{0.5}FePO₄ in between LiFePO₄ and FePO₄ must be overcompensated by the energy gain, when one LiFePO₄ / FePO₄ interface is replaced by the two LiFePO₄ / Li_{0.5}FePO₄ and Li_{0.5}FePO₄ / FePO₄ interfaces. In a simple elastic model, according to Hooke's law, the elastic energy is proportional to the square of the misfit (*f*), which leads to $2E(f/2) < E(f)$ (if prefactors do not vary too much). On the other hand, for extended identical phases, if the misfit is released by a dislocation array, $2E(f/2) > E(f)$ would result.¹⁵⁰ However, if the varied material constants and charging of dislocation are taken into account at the hetero-contact, it may be reasonable to assume that the total energy of the two interfacial energy can be less than the energy of the LiFePO₄/FePO₄ interfaces.

If there is no repulsion of the interfaces, the "equilibrium thickness" might be very small, much smaller than experimentally observed. An extended "equilibrium thickness" can be explained if elastic effects or charging effects will result in interfacial repulsion. (For a repulsion of dislocation arrays see Ref. ¹⁵¹) In Figure 5.18 and appendix, a quadratic distance law is tentatively supposed for such interfacial

repulsion (i.e. total interfacial energy decays quadratically with increasing distance), and the excess energy of the interphase is assumed to increase linearly. Figure 5.18 displays the equilibrium thickness so-obtained. If either interaction energy or phase energy change with the size, the equilibrium thickness will be size-dependent, which may even explain these experimental results (size-dependent staging). In addition, the phase energy will probably change with size through capillary effect. However, more experimental and theoretical work is necessary to confirm or disprove such a thermodynamic model.¹⁵²

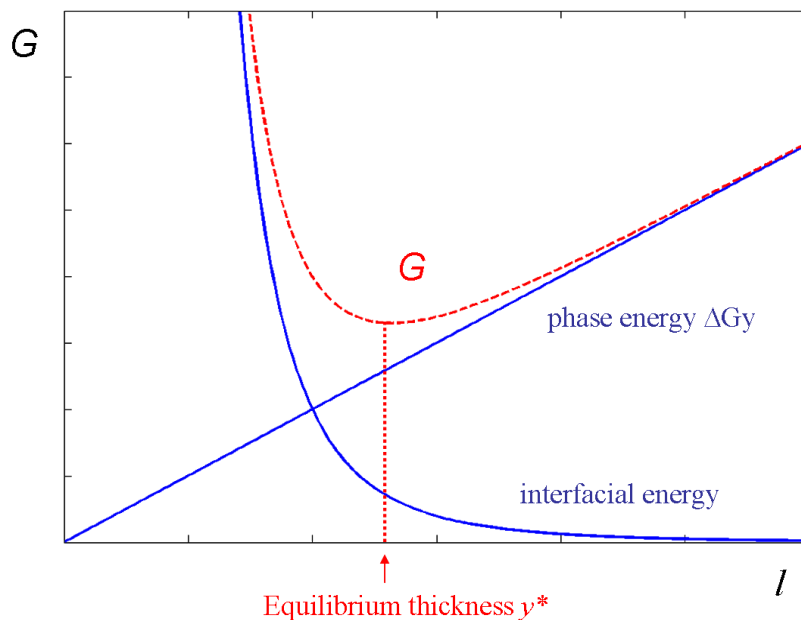


Figure 5.18 Equilibrium thickness of staging zone derived from a simple thermodynamic model.

5.5 Conclusions

In this chapter, the phase transition of LiFePO_4 was investigated systematically for large single crystals and nanosized materials. For the former case, the large single crystal was chemically delithiated. After an induction period, porous FePO_4 layers formed at the surface of LiFePO_4 due to the volume difference of the two phases, which confirmed the core-shell model for such big crystals. The thickness of FePO_4 layer was studied as function of reaction time as well. The kinetics is governed by a

parabolic growth law that indicates diffusion limitation. The effective rate constant of parabolic growth amounts to 10^{-11} cm²/s - 10^{-12} cm²/s. These effective diffusion coefficients are in between pure pore and pure solid state diffusion, indicating that the pore/crack network provides fast diffusion channels. For the nanosized LiFePO₄, with the help of the advanced STEM-ABF techniques, a first order lithium staging structure was directly observed for the partially delithiated Li_{1-x}FePO₄ (x~0.5) nanowires, which challenges the traditional phase transition model. The staging structure seems to be size dependent. In the small crystals, staging throughout with a decrease of order from center to the surface was found. For the larger nano-crystal, a staging interphase occurs constituting the interfacial zone (width around 15nm) between LiFePO₄ and FePO₄. This is compared to recent experiments on even larger nano-crystals showing such an interphase of smaller extent (around 2 nm). Thus, it appears that staging zones narrow with increasing size. These findings are discussed in the light of phase transition thermodynamics and kinetics. In particular, the possibility that the staging interphase constitutes a low energy solution to the LiFePO₄/FePO₄ contact is discussed.

Chapter 6

Overall Conclusions

LiFePO₄ is one of most promising cathode materials and has attracted large attention in the last decade. In terms of electrochemical performance, it is indeed a success story due to the efforts of many research groups all over the world. At the moment, the improvement of LiFePO₄ mainly focuses on two directions. One is to develop new synthetic methods to tailor size and the morphology to improve the electrochemical performance. The other direction is to understand fundamental properties of LiFePO₄, such as size effects and phase transition mechanisms. In this thesis, size effects on lithium storage and phase transition in the LiFePO₄/FePO₄ system are systematically investigated. Hence, the thesis is divided into two parts: 1) morphology and size controlled synthesis of LiFePO₄ and related electrochemical performance; 2) size effects on miscibility gap, lithium potential variations and phase transition process.

Part I: Morphology- and size-controlled synthesis of LiFePO₄ and related electrochemical performance

Carbon-coated single-crystalline LiFePO₄ nanowires were successfully prepared by the electrospinning method. The nanowires are not only thinner (~100 nm) compared to previous reported ones, but also single-crystalline. The growth orientation of nanowire is along the *c*-directions, with the uniform and continuous carbon coating. The unique morphology of the nanowire improves both electronic and ionic conductivities, which lead to good rate performance and excellent cycling stability.

LiFePO₄ nanoparticles with sizes below 40 nm (the thickness around 10 nm) can be prepared by the oleylamine-assisted polyol method and the particle sizes can be controlled by carefully adjusting the experimental parameters. Higher oleylamine to

TEG ratios, lower precursor concentrations and shorter reaction times lead to smaller particle sizes. In addition, adding carbon nanotubes *in-situ* can prevent particle growth. The as-prepared nanoparticles do not show good electrochemical performance due to non-conductive amorphous carbon and residue organic molecules on the surface. However, the material sintered at 700 °C for 2 hours offers good rate performance (up to 100C) and cycling stability (1000 cycles at 10C). This indicates that, for a given size window of 20~150 nm, the surface modification (quality of carbon coating) is more important than the particle size in terms of electrochemical performance.

Amorphous FePO₄ and LiFePO₄ were prepared by the precipitation method. Heat treatment of amorphous LiFePO₄ at high temperature (550°C) leads to nanocrystalline LiFePO₄ particles. Sloped-type charge and discharge curves of amorphous LiFePO₄ were found instead of voltage plateau, which indicates single phase regime for lithium intercalation.

Part II: Size effects on miscibility gap, lithium potential variations and phase transition process

A single phase lithium intercalation regime for amorphous LiFePO₄ was confirmed by PITT technique. On the other hand, a shrinkage of the miscibility gap with decreasing particle size was also observed by the same method.

Lithium potential variations for nanocrystalline and amorphous LiFePO₄ were investigated thermodynamically and experimentally. It is crucial to distinguish between single phase and two phase regimes. For the nanocrystalline LiFePO₄/FePO₄ two phase regime, the reversible OCV values decrease with decreasing particle size. In addition, surface chemistry (γ) plays a crucial role in the OCV variations. The effects continuously increase with increased capillary pressure, *i.e.* ratio of surface tension (γ) to radius (r). For amorphous LiFePO₄, the excess OCV is negative as compared with crystalline heterosite FePO₄, while it is positive if compared to the crystalline hexagonal FePO₄ structure. As the latter appears to be closer to the short range order in the amorphous material, the excess potential of introducing Li will be

negative. At any rate, ionic and electronic contributions to $\mu_{\text{Li}}^{\text{ex}}$ play a crucial role in deciding upon lithium potential variations.

Phase transition of large LiFePO_4 single crystals was investigated by chemical delithiation. After an induction period, FePO_4 layers with high porosity and cracks form at the surface of LiFePO_4 owing to the volume difference of phases, which confirm the shrinking core model for such large crystals. The kinetics is governed by a parabolic growth law that indicates diffusion limitation. The effective rate constant of parabolic growth is $\sim 10^{-11} \text{ cm}^2/\text{s}$ to $10^{-12} \text{ cm}^2/\text{s}$. These effective diffusion coefficients are in between pure pore and pure solid state diffusion. As a result, the pore/crack network provides fast diffusion channels.

On the other hand, for the nanosized LiFePO_4 , by means of the advanced STEM-ABF techniques, a lithium staging structure was directly observed in the partially delithiated $\text{Li}_{1-x}\text{FePO}_4$ ($x \sim 0.5$) nanowires for the first time, which challenge the traditional two-phase separation model. Various staging phenomena were observed. For large crystals, staging structures exist as a contact phase between LiFePO_4 and FePO_4 , and the staging width narrows with increasing size. For small crystals, the staging structure appears throughout the whole particle with decrease of order from center to the surface. The findings are discussed in the light of thermodynamics and kinetics. In particular, the possibility is discussed that the staging interphase constitutes a low energy solution to the $\text{LiFePO}_4/\text{FePO}_4$ contact.

Appendix:¹⁵²

Here we discuss the possibility of $\text{Li}_{0.5}\text{FePO}_4$ ($\text{L}_{0.5}\text{FP}$) to be a stable interphase between LiFePO_4 and FePO_4 even though exhibiting a higher excess free energy than $\frac{1}{2} \text{LiFePO}_4: \frac{1}{2} \text{FePO}_4$.

I_0 : free enthalpy of a LiFePO_4 (LFP) / FePO_4 (FP) interface

I' : free enthalpy of LFP / $\text{L}_{0.5}\text{FP}$ interface

I'' : free enthalpy of FP / $\text{L}_{0.5}\text{FP}$ interface

x : thickness of LFP region (FP region)

y : thickness of $\text{L}_{0.5}\text{FP}$ region

We assume planar interfaces.

First assumption is $I^* \equiv I' + I'' < I_0$, (see Section 5.4.2)

The second assumption is that I^* decreases with increased thickness of the interphase (see Section 5.4.2).

The overall thickness L is:

$$L = 2x + y$$

Note that this thickness stays constant in a possible transformation process:

$$\text{L}_{0.5}\text{FP} \rightarrow \frac{1}{2} \text{LFP} + \frac{1}{2} \text{FP}, \text{ since } \Delta y = -2\Delta x \text{ (conservation of PO}_4 \text{ units).}$$

Owing to the above:

$$I^*(y=0) = I_0 \text{ and } \frac{dI^*}{dy} < 0$$

While with increasing y , I^* will decrease, the free enthalpy of the material in between will increase owing to

$$\Delta G_d \equiv \Delta G\{\text{L}_{0.5}\text{FP} \rightarrow \frac{1}{2} \text{LFP} + \frac{1}{2} \text{FP}\} < 0$$

The total free enthalpy is:

$$G = x(G_{\text{LFP}} + G_{\text{FP}}) + yG_{\text{L}_{0.5}\text{FP}} + I^*$$

$$G = \frac{L}{2}(G_{\text{LFP}} + G_{\text{FP}}) + y(-\Delta G_d) + I^*$$

$$\frac{dG}{dy} = -\Delta G_d + \frac{dI^*}{dy}$$

The counteracting behavior leads to interesting consequences. If $I^*(y)$ decreases linearly, we either find no or only staging phase in equilibrium.

(i) $I^* = -my + I_0$ and $\frac{dI^*}{dy} = -m$ ($m > 0$)

$$\frac{dG}{dy} = -\Delta G - m = |\Delta G| - |m|$$

If $|m| < |\Delta G| \Rightarrow \frac{dG}{dy} > 0 \Rightarrow$ no intermediate staging phase ($y=0$)

If $|m| > |\Delta G| \Rightarrow \frac{dG}{dy} < 0 \Rightarrow$ the entire crystallite adopts the staging structure ($y=L$)

(providing surface energy differences are not very significant)

If $|m| = |\Delta G| \Rightarrow$ indifferent (i.e. surface energy difference will be decisive)

If however I^* decreases super-linearly, then there will be an equilibrium thickness $0 < y < L$.

Two formal cases are considered: quadratic decrease (ii) and exponential decrease (iii):

(ii)

$$I^* = I_0 - \varepsilon y^2 \quad (\text{For } y < \sqrt{\frac{I_0}{\varepsilon}}, \varepsilon > 0)$$

$$\frac{dI^*}{dy} = -2\varepsilon y$$

$$\hat{y}^* = \frac{-\Delta G_d}{2\varepsilon} = \frac{|\Delta G_d|}{2\varepsilon}$$

(iii) $I^* = I_0 e^{-\alpha y}$

$$\frac{dI^*}{dy} = -\alpha I_0 e^{-\alpha y}$$

$$\hat{y} = \frac{1}{\alpha} \ln\left(\frac{\alpha I_0}{-\Delta G_d}\right)$$

For the sake of simplicity, case (ii) was chosen for the discussion in Section 5.4.2.

Note that $|\Delta G_d|$ may increase, if y is reduced below the Debye length owing to double layer repulsion.

Reference:

1. B. Scrosati and J. Garche, *Journal of Power Sources*, 2010, **195**, 2419-2430.
2. J. B. Goodenough and Y. Kim, *Journal of Power Sources*, 2011, **196**, 6688-6694.
3. B. Dunn, H. Kamath and J.-M. Tarascon, *Science*, 2011, **334**, 928-935.
4. K. Mizushima, P. C. Jones, P. J. Wiseman and J. B. Goodenough, *Materials Research Bulletin*, 1980, **15**, 783-789.
5. Y.-K. Sun, S.-T. Myung, B.-C. Park, J. Prakash, I. Belharouak and K. Amine, *Nature Materials*, 2009, **8**, 320-324.
6. C. S. Johnson, N. Li, C. Lefief, J. T. Vaughey and M. M. Thackeray, *Chemistry of Materials*, 2008, **20**, 6095-6106.
7. A. K. Padhi, K. S. Nanjundaswamy and J. B. Goodenough, *Journal Of The Electrochemical Society*, 1997, **144**, 1188-1194.
8. M. S. Whittingham, *Chem. Rev.*, 2004, **104**, 4271-4301.
9. S. Liang, U. H. Choi, W. Liu, J. Runt and R. H. Colby, *Chemistry of Materials*, 2012, **24**, 2316-2323.
10. V. Di Noto, S. Lavina, G. A. Giffin, E. Negro and B. Scrosati, *Electrochimica Acta*, 2011, **57**, 4-13.
11. L. Xia, D. Wang, H. Yang, Y. Cao and X. Ai, *Electrochemistry Communications*, 2012, **25**, 98-100.
12. W. Fu-Ming, Y. Meng-Han, C. Chin-Shu, S. A. Pradanawati, L. Shen-Chuan and J. Rick, *Journal of Power Sources*, 2013, **231**, 18-22.
13. N. Byrne, P. C. Howlett, D. R. MacFarlane and M. Forsyth, *Adv. Mater.*, 2005, **17**, 2497.
14. Y. Lu, S. K. Das, S. S. Moganty and L. A. Archer, *Adv. Mater.*, 2012, **24**, 4430-4435.
15. C. Zhu, H. Cheng and Y. Yang, *Journal of the Electrochemical Society*, 2008, **155**, A569-A575.

16. R. Dominko, M. Bele, J.-M. Goupil, M. Gaberscek, D. Hanzel, I. Arcon and J. Jamnik, *Chemistry of Materials*, 2007, **19**, 2960.
17. S. F. Yang, P. Y. Zavalij and M. S. Whittingham, *Electrochemistry Communications*, 2001, **3**, 505-508.
18. H. Yang, X. L. Wu, M. H. Cao and Y. G. Guo, *J. Phys. Chem. C*, 2009, **113**, 3345-3351.
19. C. Delacourt, P. Poizot, M. Morcrette, J. M. Tarascon and C. Masquelier, *Chemistry Of Materials*, 2004, **16**, 93-99.
20. B. L. Ellis, W. R. M. Makahnouk, Y. Makimura, K. Toghill and L. F. Nazar, *Nature Materials*, 2007, **6**, 749-753.
21. C. Delacourt, J. Rodriguez-Carvajal, B. Schmitt, J. M. Tarascon and C. Masquelier, *Solid State Sciences*, 2005, **7**, 1506-1516.
22. J. Maier and R. Amin, *Journal Of The Electrochemical Society*, 2008, **155**, A339-A344.
23. B. Ellis, L. K. Perry, D. H. Ryan and L. F. Nazar, *Journal Of The American Chemical Society*, 2006, **128**, 11416-11422.
24. R. G. Iyer, C. Delacourt, C. Masquelier, J. M. Tarascon and A. Navrotsky, *Electrochemical And Solid State Letters*, 2006, **9**, A46-A48.
25. C. Delacourt, P. Poizot, J. M. Tarascon and C. Masquelier, *Nature Materials*, 2005, **4**, 254-260.
26. J. M. Tarascon and M. Armand, *Nature*, 2001, **414**, 359.
27. A. Yamada, H. Koizumi, N. Sonoyama and R. Kanno, *Electrochemical And Solid State Letters*, 2005, **8**, A409-A413.
28. A. S. Andersson, B. Kalska, L. Haeggstroem and J. O. Thomas, *Solid State Ionics*, 2000, **130**, 41.
29. A. S. Andersson and J. O. Thomas, *Journal Of Power Sources*, 2001, **97-8**, 498-502.
30. L.-X. Yuan, Z.-H. Wang, W.-X. Zhang, X.-L. Hu, J.-T. Chen, Y.-H. Huang and J. B. Goodenough, *Energy Environ. Sci.*, 2011, **4**, 269-284.
31. A. S. Andersson, J. O. Thomas, B. Kalska and L. Haggstrom, *Electrochemical*

- and Solid State Letters*, 2000, **3**, 66-68.
32. R. Amin, P. Balaya and J. Maier, *Electrochemical And Solid State Letters*, 2007, **10**, A13-A16.
33. S. Okada, S. Sawa, M. Egashira, J.-i. Yamaki, M. Tabuchi, H. Kageyama, T. Konishi and A. Yoshino, *Journal of Power Sources*, 2001, **97-98**, 430-432.
34. M. S. Islam, D. J. Driscoll, C. A. J. Fisher and P. R. Slater, *Chemistry Of Materials*, 2005, **17**, 5085-5092.
35. Y. Wang, P. He and H. Zhou, *Energy Environ. Sci.*, 2011, **4**, 805-817.
36. N. Ravet, Y. Chouinard, J. F. Magnan, S. Besner, M. Gauthier and M. Armand, *Journal of Power Sources*, 2001, **97-98**, 503.
37. P. S. Herle, B. Ellis, N. Coombs and L. F. Nazar, *Nature Materials*, 2004, **3**, 147-152.
38. C. Delacourt, P. Poizot, S. Levasseur and C. Masquelier, *Electrochemical And Solid State Letters*, 2006, **9**, A352-A355.
39. C. Delacourt, L. Laffont, R. Bouchet, C. Wurm, J. B. Leriche, M. Morcrette, J. M. Tarascon and C. Masquelier, *Journal of The Electrochemical Society*, 2005, **152**, A913.
40. K. S. Park, S. B. Schougaard and J. B. Goodenough, *Adv. Mater.*, 2007, **19**, 848.
41. P. P. Prosini, M. Lisi, D. Zane and M. Pasquali, *Solid State Ionics*, 2002, **148**, 45-51.
42. K. Tang, X. Yu, J. Sun, H. Li and X. Huang, *Electrochimica Acta*, 2011, **56**, 4869-4875.
43. R. Amin, J. Maier, P. Balaya, D. P. Chen and C. T. Lin, *Solid State Ionics*, 2008, **179**, 1683-1687.
44. J. J. Wang and X. L. Sun, *Energy Environ. Sci.*, 2012, **5**, 5163-5185.
45. F. Croce, A. D. Epifanio, J. Hassoun, A. Deptula, T. Olczac and B. Scrosati, *Electrochemical and Solid-State Letters*, 2002, **5**, A47.
46. N. Ravet, J. B. Goodenough, S. Besner, M. Simoneau, P. Hovington and M. Armand, *The Electrochem. Soc. and The Electrochem.Soc. of Japan Meeting*

- Abstracts*, 1999, 99.
47. S. Beninati, L. Damen and M. Mastragostino, *Journal of Power Sources*, 2008, **180**, 875-879.
 48. N. Ravet, M. Gauthier, K. Zaghbi, J. B. Goodenough, A. Mauger, F. Gendron and C. M. Julien, *Chemistry of Materials*, 2007, **19**, 2595-2602.
 49. R. Dominko, M. Bele, M. Gaberscek, M. Remskar, D. Hanzel, J. M. Goupil, S. Pejovnik and J. Jamnik, *Journal of Power Sources*, 2006, **153**, 274-280.
 50. R. Dominko, M. Bele, M. Gaberscek, M. Remskar, D. Hanzel, S. Pejovnik and J. Jamnik, *Journal of The Electrochemical Society*, 2005, **152**, A607.
 51. R. Dominko, J. M. Goupil, M. Bele, M. Gaberscek, M. Remskar, D. Hanzel and J. Jamnik, *Journal of The Electrochemical Society*, 2005, **152**, A858.
 52. B. Kang and G. Ceder, *Nature*, 2009, **458**, 190.
 53. Y. Wang, Y. Wang, E. Hosono, K. Wang and H. Zhou, *Angewandte Chemie International Edition*, 2008, **47**, 7461-7465.
 54. Y.-S. Hu, Y.-G. Guo, R. Dominko, M. Gaberscek, J. Jamnik and J. Maier, *Adv. Mater.*, 2007, **19**, 1963.
 55. H.-H. Chang, C.-C. Chang, C.-Y. Su, H.-C. Wu, M.-H. Yang and N.-L. Wu, *Journal of Power Sources*, 2008, **185**, 466-472.
 56. H. Liu, G. X. Wang, D. Wexler, J. Z. Wang and H. K. Liu, *Electrochemistry Communications*, 2008, **10**, 165-169.
 57. P. Bruce, B. Scrosati and J. M. Tarascon, *Angewandte Chemie International Edition*, 2008, **47**, 2930.
 58. W.-J. Zhang, *Journal of Power Sources*, 2011, **196**, 2962-2970.
 59. D. Morgan, A. Van der Ven and G. Ceder, *Electrochemical And Solid State Letters*, 2004, **7**, A30-A32.
 60. S. Y. Chung, J. T. Bloking and Y. M. Chiang, *Nature Materials*, 2002, **1**, 123-128.
 61. N. Ravet, A. Abouimrane and M. Armand, *Nature materials*, 2003, **2**, 702-703.
 62. C. A. J. Fisher, V. M. H. Prieto and M. S. Islam, *Chemistry Of Materials*, 2008, **20**, 5907-5915.

63. R. Amin, C. T. Lin and J. Maier, *Physical Chemistry Chemical Physics*, 2008, **10**, 3519-3523.
64. R. Amin, C. T. Lin, J. B. Peng, K. Weichert, T. Acarturk, U. Starke and J. Maier, *Adv. Funct. Mater.*, 2009, **19**, 1697-1704.
65. D. Samuelis and J. Maier, *Chemical Energy Storage*, 2013, R. Schlögl (ed.), W. De Gruyter, Berlin, 225-248.
66. R. Amin and J. Maier, *Solid State Ionics*, 2008, **178**, 1831.
67. R. Amin, C. T. Lin and J. Maier, *Physical Chemistry Chemical Physics*, 2008, **10**, 3524-3529.
68. C. Zhu, K. Weichert and J. Maier, *Adv. Funct. Mater.*, 2011, **21**, 1917.
69. W. Bragg, *Proceedings of the Cambridge Philosophical Society*, 1913, **17**, 43-57.
70. R. Jenkins and R. Snyder, *Introduction to X-ray powder diffractometry*, 1996, New York: Wiley.
71. S. D. Findlay, N. Shibata, H. Sawada, E. Okunishi, Y. Kondo, T. Yamamoto and Y. Ikuhara, *Applied Physics Letters*, 2009, **95**, 191913.
72. S. D. Findlay, N. Shibata, H. Sawada, E. Okunishi, Y. Kondo and Y. Ikuhara, *Ultramicroscopy*, 2010, **110**, 903-923.
73. X. He, L. Gu, C. Zhu, Y. Yu, C. Li, Y.-S. Hu, H. Li, S. Tsukimoto, J. Maier, Y. Ikuhara and X. Duan, *Materials Express*, **1**, 43.
74. A. Bard and L. Faulkner, *Electrochemical. Methods: Fundamentals and Applications*, 2000, John Wiley and Sons: New York.
75. Y. Zhu and C. Wang, *J. Phys. Chem. C*, 2010, **114**, 2830-2841.
76. A. H. Thompson, *Physical Review Letters*, 1978, **40**, 1511-1514.
77. A. H. Thompson, *Journal of the Electrochemical Society*, 1979, **126**, 608-616.
78. S. Franger, F. Le Cras, C. Bourbon and H. Rouault, *Journal of Power Sources*, 2003, **119–121**, 252-257.
79. M. K. Devaraju and I. Honma, *Advanced Energy Materials*, 2012, **2**, 284-297.
80. J. J. Chen, M. J. Vacchio, S. J. Wang, N. Chernova, P. Y. Zavalij and M. S. Whittingham, *Solid State Ionics*, 2008, **178**, 1676-1693.

81. J. Ni, M. Morishita, Y. Kawabe, M. Watada, N. Takeichi and T. Sakai, *Journal of Power Sources*, 2010, **195**, 2877-2882.
82. D.-H. Kim and J. Kim, *Electrochemical and Solid-State Letters*, 2006, **9**, A439.
83. J.-S. Lim, D.-H. Kim, V. Mathew, D.-C. Ahn and J.-K. Kim, *J. Nanosci. Nanotechnol.*, 2011, **11**, 1451-1454.
84. J. Lim, V. Mathew, K. Kim, J. Moon and J. Kim, *Journal Of The Electrochemical Society*, 2011, **158**, A736-A740.
85. K. Saravanan, M. V. Reddy, P. Balaya, H. Gong, B. V. R. Chowdari and J. J. Vittal, *Journal of Materials Chemistry*, 2009, **19**, 605-610.
86. P. P. Prosini, M. Carewska, S. Scaccia, P. Wisniewski, S. Passerini and M. Pasquali, *Journal Of The Electrochemical Society*, 2002, **149**, A886-A890.
87. X. Wang, C. Miao, J. Zhou, C. Ma, H. Wang and S. Sun, *Mater. Lett.*, 2011, **65**, 2096-2099.
88. C. M. Doherty, R. A. Caruso, B. M. Smarsly, P. Adelhelm and C. J. Drummond, *Chemistry of Materials*, 2009, **21**, 5300.
89. S. Lim, C. S. Yoon and J. Cho, *Chemistry of Materials*, 2008, **20**, 4560.
90. D. Li and Y. Xia, *Adv. Mater.*, 2004, **16**, 1151.
91. A. Greiner and J. Wendorff, *Angewandte Chemie International Edition*, 2007, **46**, 5670.
92. W. Sigmund, J. Yuh, H. Park, V. Maneeratana, G. Pyrgiotakis, A. Daga, J. Taylor and J. C. Nino, *Journal of the American Ceramic Society*, 2006, **89**, 395.
93. Y. Yu, L. Gu, C. Wang, A. Dhanabalan, P. van Aken and J. Maier, *Angewandte Chemie International Edition*, 2009, **48**, 6485.
94. E. Hosono, Y. Wang, N. Kida, M. Enomoto, N. Kojima, M. Okubo, H. Matsuda, Y. Saito, T. Kudo, I. Honma and H. Zhou, *ACS Applied Materials & Interfaces*, 2009, **2**, 212.
95. G. Y. Chen, X. Y. Song and T. J. Richardson, *Electrochemical And Solid State Letters*, 2006, **9**, A295-A298.

96. A. V. Murugan, T. Muraliganth, P. J. Ferreira and A. Manthiram, *Inorganic Chemistry*, 2009, **48**, 946.
97. D. P. Chen, A. Maljuk and C. T. Lin, *J. Cryst. Growth*, 2005, **284**, 86-90.
98. C. Ban, N. A. Chernova and M. S. Whittingham, *Electrochemistry Communications*, 2009, **11**, 522.
99. A. L. Viet, M. V. Reddy, R. Jose, B. V. R. Chowdari and S. Ramakrishna, *The Journal of Physical Chemistry C*, 2009, **114**, 664.
100. H.-K. Seong, M.-H. Kim, H.-J. Choi, Y.-J. Choi and J.-G. Park, *Metals and Materials International*, 2008, **14**, 477.
101. Y. Hong, H. Fan and X. Zhang, *The Journal of Physical Chemistry B*, 2009, **113**, 5837.
102. X. M. Liu and Y. C. Zhou, *J. Cryst. Growth*, 2004, **270**, 527.
103. C. Rui and et al., *Applied Physics Letters*, 2009, **95**, 061908.
104. Z. G. Lu, H. Cheng, M. F. Lo and C. Y. Chung, *Adv. Funct. Mater.*, 2007, **17**, 3885-3896.
105. Y.-L. Ding, J. Xie, G.-S. Cao, T.-J. Zhu, H.-M. Yu and X.-B. Zhao, *Adv. Funct. Mater.*, 2011, **21**, 348-355.
106. J. K. Kim, G. Cheruvally and J. H. Ahn, *J. Solid State Electrochem.*, 2008, **12**, 799-805.
107. C. Wei-Ming, W. Cheng-Chien and C. Chuh-Yung, *J. Mater. Sci.*, 2013, **48**, 1042-1052.
108. E. Uchaker, N. Zhou, Y. Li and G. Cao, *J. Phys. Chem. C*, 2013, **117**, 1621-1626.
109. J. Kang, S. Baek, V. Mathew, J. Gim, J. Song, H. Park, E. Chae, A. K. Rai and J. Kim, *Journal of Materials Chemistry*, 2012, **22**, 20857-20860.
110. D. Rangappa, K. Sone, M. Ichihara, T. Kudo and I. Honma, *Chem. Commun.*, 2010, **46**, 7548-7550.
111. D. Kim, J. Lim, E. Choi, J. Gim, V. Mathew, Y. Paik, H. Jung, W. Lee, D. Ahn, S. Paek and J. Kim, *Surf. Rev. Lett.*, 2010, **17**, 111-119.
112. V. K. Lamer and R. H. Dinegar, *Journal Of The American Chemical Society*,

- 1950, **72**, 4847-4854.
113. A. V. Murugan, T. Muraliganth and A. Manthiram, *Electrochemistry Communications*, 2008, **10**, 903-906.
114. D. Rangappa, K. Sone, Y. Zhou, T. Kudo and I. Honma, *Journal Of Materials Chemistry*, 2011, **21**, 15813-15818.
115. D. Rangappa, M. Ichihara, T. Kudo and I. Honma, *Journal Of Power Sources*, 2009, **194**, 1036-1042.
116. O. Delmer, P. Balaya, L. Kienle and J. Maier, *Adv. Mater.*, 2008, **20**, 501.
117. M. Isono, S. Okada and J.-i. Yamaki, *Journal of Power Sources*, 2010, **195**, 593-598.
118. P. P. Prosini, M. Lisi, S. Scaccia, M. Carewska, F. Cardellini and M. Pasquali, *Journal of The Electrochemical Society*, 2002, **149**, A297.
119. Y.-S. Hong, K. S. Ryu, Y. J. Park, M. G. Kim, J. M. Lee and S. H. Chang, *Journal of Materials Chemistry*, 2002, **12**, 1870-1874.
120. C. Delacourt, P. Poizot, D. Bonnin and C. Masquelier, *Journal of The Electrochemical Society*, 2009, **156**, A595.
121. Y. J. Lee, H. Yi, W.-J. Kim, K. Kang, D. S. Yun, M. S. Strano, G. Ceder and A. M. Belcher, *Science*, 2009, **324**, 1051-1055.
122. N. Aliouane, T. Badeche, Y. Gagou, E. Nigrelli and P. Saint-Gregoire, *Ferroelectrics*, 2000, **241**, 255-262.
123. Y. S. Hong, K. S. Ryu, Y. J. Park, M. G. Kim, J. M. Lee and S. H. Chang, *Journal of Materials Chemistry*, 2002, **12**, 1870-1874.
124. N. Meethong, H. Y. S. Huang, W. C. Carter and Y. M. Chiang, *Electrochemical And Solid State Letters*, 2007, **10**, A134-A138.
125. A. Yamada, H. Koizumi, S. I. Nishimura, N. Sonoyama, R. Kanno, M. Yonemura, T. Nakamura and Y. Kobayashi, *Nature Materials*, 2006, **5**, 357-360.
126. G. Kobayashi, S. I. Nishimura, M. S. Park, R. Kanno, M. Yashima, T. Ida and A. Yamada, *Adv. Funct. Mater.*, 2009, **19**, 395-403.
127. P. Gibot, M. Casas-Cabanas, L. Laffont, S. Levasseur, P. Carlach, S. Hamelet,

- J. M. Tarascon and C. Masquelier, *Nature Materials*, 2008, **7**, 741-747.
128. N. Meethong, Y. H. Kao, W. C. Carter and Y. M. Chiang, *Chemistry of Materials*, 2010, **22**, 1088-1097.
129. M. Wagemaker, D. P. Singh, W. J. H. Borghols, U. Lafont, L. Haverkate, V. K. Peterson and F. M. Mulder, *Journal of the American Chemical Society*, **133**, 10222.
130. K. Zaghib, A. Mauger, F. Gendron and C. M. Julien, *Chemistry Of Materials*, 2008, **20**, 462-469.
131. J. Jamnik and J. Maier, *Physical Chemistry Chemical Physics*, 2003, **5**, 5215-5220.
132. P. Buffat and J. P. Borel, *Physical Review A*, 1976, **13**, 2287-2298.
133. J. Maier, *Angewandte Chemie International Edition*, 2012, in press.
134. K. T. Lee, W. H. Kan and L. F. Nazar, *Journal Of The American Chemical Society*, 2009, **131**, 6044.
135. W. Dreyer, J. Jamnik, C. Gohlke, R. Huth, J. Moskon and M. Gaberscek, *Nature Materials*, 2010, **9**, 448-453.
136. M. Wagemaker, F. M. Mulder and A. Van der Ven, *Adv. Mater.*, 2009, **21**, 2703.
137. V. Srinivasan and J. Newman, *Journal Of The Electrochemical Society*, 2004, **151**, A1517-A1529.
138. L. Laffont, C. Delacourt, P. Gibot, M. Y. Wu, P. Kooyman, C. Masquelier and J. M. Tarascon, *Chemistry Of Materials*, 2006, **18**, 5520-5529.
139. C. Delmas, M. Maccario, L. Croguennec, F. Le Cras and F. Weill, *Nature Materials*, 2008, **7**, 665-671.
140. N. Sharma, X. W. Guo, G. D. Du, Z. P. Guo, J. Z. Wang, Z. X. Wang and V. K. Peterson, *Journal Of The American Chemical Society*, 2012, **134**, 7867-7873.
141. X. Liu, J. Liu, R. Qiao, Y. Yu, H. Li, L. Suo, Y.-S. Hu, Y.-D. Chuang, G. Shu, F. Chou, T.-C. Weng, D. Nordlund, D. Sokaras, Y. J. Wang, H. Lin, B. Barbiellini, A. Bansil, X. Song, Z. Liu, S. Yan, G. Liu, S. Qiao, T. J. Richardson, D. Prendergast, Z. Hussain, F. M. F. de Groot and W. Yang, *Journal of the*

- American Chemical Society*, 2012, **134**, 13708.
142. R. Malik, F. Zhou and G. Ceder, *Nature Materials*, 2011, **10**, 587-590.
143. K. Weichert, W. Sigle, P. A. van Aken, J. Jamnik, C. Zhu, R. Amin, T. Acartuerk, U. Starke and J. Maier, *Journal of the American Chemical Society*, 2012, **134**, 2988.
144. W. Sigle, R. Amin, K. Weichert, P. A. van Aken and J. Maier, *Electrochemical And Solid State Letters*, 2009, **12**, A151-A154.
145. S.-H. Yang, L. Croguennec, C. Delmas, E. C. Nelson and M. O'Keefe, *Nature Materials*, 2003, **2**, 464-467.
146. Y. Oshima, H. Sawada, F. Hosokawa, E. Okunishi, T. Kaneyama, Y. Kondo, S. Niitaka, H. Takagi, Y. Tanishiro and K. Takayanagi, *Journal of Electron Microscopy*, 2010, **59**, 457-461.
147. L. Gu, C. Zhu, H. Li, Y. Yu, C. Li, S. Tsukimoto, J. Maier and Y. Ikuhara, *Journal of the American Chemical Society*, 2011, **133**, 4661.
148. L. M. Suo, W. Z. Han, X. Lu, L. Gu, Y. S. Hu, H. Li, D. F. Chen, L. Q. Chen, S. Tsukimoto and Y. Ikuhara, *Physical Chemistry Chemical Physics*, 2012, **14**, 5363-5367.
149. Y. Sun, X. Lu, R. Xiao, H. Li and X. Huang, *Chemistry of Materials*, 2012.
150. W. T. Read and W. Shockley, *Physical Review*, 1950, **78**, 275-289.
151. W. Sigle, C. Sarbu, D. Brunner and M. Rühle, *Philosophical Magazine*, 2006, **86**, 4809-4821.
152. C. B. Zhu, L. Gu, L. M. Suo, J. Popovic, H. Li, Y. Ikuhara and J. Maier, *to be submitted*, 2013.

Abbreviations and Symbols

List of Abbreviations

ABF	Annular-bright- field
AES	Atomic Emission Spectroscopy
BET	Brunauer-Emmett-Teller
CNT	Carbon nanotubes
CTAB	Hexadecyl- trimethylammonium bromide
CV	Cyclic voltammetry
DC	Direct current
DMC	Dimethyl carbonate
DOD	Depth of discharge
DSC	Differential Scanning Calorimetry
EC	Ethylene carbonate
ED	Electron diffraction
EDS	Energy dispersive spectra
EDX	Energy-dispersive X-ray spectroscopy
EELS	Electron energy loss spectroscopy
EIS	Electrochemical impedance spectroscopy
e.m.f.	Electromotive force
EV	Electric vehicle
FTIR	Fourier transform infrared spectroscopy
GITT	Galvanostatic intermittent titration technique
HAADF	High angle annular dark field
HEV	Hybrid electric vehicle
HR-TEM	High-resolution transmission electron microscope

Abbreviations and Symbols

ICE	Internal combustion engine
ICP	Inductively Coupled Plasma Analysis
LIB	Lithium ion battery
MCMB	Mesocarbon microbeads
NO ₂ BF ₄	Nitronium tetrafluoro-borate
OCV	Open circuit voltage
OL	Oleylamine
PANI	Polyaniline
PEDOT	Poly(3,4-ethylenedioxythiophene)
PEG	Polyethylene glycol
PEO	Poly(ethylene oxide)
PITT	Potentiostatic intermittent titration technique
PPy	Polypyrrole
SAED	Selected area electron diffraction
SCNW-LFP	Single-crystalline LiFePO ₄ nanowires
SEM	Scanning electron microscopy
SOC	State of charge
STEM	Scanning transmission electron microscopy
TEG	Tetraethyleneglycol
TEM	Transmission electron microscopy
TG	Thermogravimetry
TMAOH	Tetramethylammonium hydroxide
TOF-SIMS	Time-of-flight secondary ion mass spectrometry
XRD	X-ray diffraction

List of Symbols

μ	chemical potential
μ_A	chemical potential of lithium in anode
μ_C	chemical potential of lithium in cathode
n	number of electrons
E	thermodynamic equilibrium cell voltage
F	Faraday constant
$\Delta_r G$	Gibbs free energy of the reaction
t	diffusion time
L	diffusion distance
D	diffusion coefficient
D_{Li}^δ	chemical diffusion for Li
Fe_{Li}^\bullet	anti-site defects
V_{Li}'	lithium vacancies
h^\bullet	holes
Li_i^\bullet	lithium interstitials
e'	electrons
d_{hkl}	interplanar spacing in specific crystalline lattice
θ	Bragg diffraction angle
d	average grain size
K	shape factor
$\beta_{1/2}$	width of diffraction peak at half-height
I_p	current maximum
A	electrode area

Abbreviations and Symbols

C	concentration
v	scan rate
γ	surface tension
r	effective radius
V_{Li}	partial molar volume of lithium
$V_{1,2}$	molar volume of phase 1 or 2
r_0	atomistic size
$\Delta_m G$	free melting energy
$r_{1,2}$	particle size of phase 1, 2
μ_i^{ex}	excess chemical potential of Li interstitial
μ_n^{ex}	excess chemical potential of electrons
$E_{1/2}$	average voltage between oxidation and reduction peak
V_{ox}	peak potentials of oxidation
V_{ox}	peak potentials of oxidation
V_{re}	peak potentials of reduction
κ	effective rate constants
Γ	Gibbs energy per number FePO ₄ -units
ξ_{Li}	the ratio of number of Li and number of FePO ₄
λ	wavelength of X-ray

Acknowledgements

First and foremost, I would like to express my greatest gratitude to Prof. Dr. Joachim Maier who gave me this value opportunity to perform my research in such a famous institute. I will never forget his support, great questions, fruitful discussions and lots of patience during this journey. Without those, this thesis would not have been possible. His devotion and my thanks to him can not be expressed in words.

I acknowledge Prof. Dr. Cosima Stubenrauch and Prof. Dr. Joachim Bill for spending significant time being my examination committee.

I would like to especially thank Dr. Katja Weichert who is my internal supervisor in the first two more years. She really helped me a lot not only on my research but also on my daily life. I am also very appreciative for Prof. Dr. Yan Yu and Prof. Dr. Lin Gu's great help on experiments and supportive advices.

I am appreciative of Dr. Jelena Popović and Prof. Dr. Chunlei Wang's help for correcting my thesis, and Christian Pfaffhuber's assistance for the "Zusammenfassung". In addition, I acknowledge Sofia Weiglein's patient administrative support and Dieter Fischer's correction for my annual PhD report.

I would like to thank Dr. Rotraut Merkle, who is always been ready for any discussion and for performing TG/DSC measurements. I appreciated Prof. Dr. Hong Li's suggestions on the project of "phase transition of LiFePO_4 ", Dr. Chilin Li's helpful scientific discussions, and all the help from our "battery group".

I am very grateful to the people who assisted me with technical support, including: Viola Duppel, Xiaoke Mu, Dan Zhou for TEM micrographs, Dr. Lin Gu for ABF

images, Gabi Götz for hundreds of XRD patterns, Anette Fuchs for SEM and BET measurements, Armin Schultz for Raman spectra, Udo Klock for DSC measurement and solving technical problem, Peter Senk for oven and gas assistance, Ewald Schmitt for metal processing, Uve Traub for solving all the IT problems, Albrecht Meyer for chemical analysis, W. König for FTIR spectra, Evaporation and sputtering group for Ti deposition, Service group for surface analysis.

Many thanks to Dr. Lijun Fu and Dr. Lei Wang's help when I just joined our group. Special thanks to all of my Chinese colleagues and friends in our institute for their help and accompanying during my PHD.

In addition, I acknowledge my previous supervisors Prof. Dr. Yong Yang and Prof. Dr. Shengtao Zhang, who have supported and encouraged me all the time.

Of course, special thanks to all my colleagues and former members in our group: Dr. Giuliano Gregori, Dr. Klaus-Dieter Kreuer, Dr. Dominik Samuelis, Dr. Denis Gryaznov, Dr. Eugene Kotomin, Dr. Kun Tang, Barbara Reichert, Kiran Adepalli, Federico Baiutti, Evgeny Blokhin, Chia-Chin Chen, Oliver Gerbig, Elisa Gilardi, Marcus Göbel, Michael Marino, Jan Melchior, Nils Ohmer, Daniel Pötzsch, Sebastian Stämmler, Anja Wedig, Michael Weissmayer, Andreas Wohlfarth, Prof. Dr. Palani Balaya, Dr. Carla Cavalca de Araujo, Dr. Olga Delmer, Prof. Dr. Miran Gaberscek, Prof. Dr. Xin Guo, Prof. Dr. Yuguo Guo, Prof. Dr. Yongsheng Hu, Prof. Dr. Xiangxin Guo, Dr. Anna Jarosik, Dr. Jong-Hoon Joo, Dr. Nitin Kaskhedikar, Dr. Piero Lupetin, Dr. Ji-Yong Shin, Dr. Mona Shirpour, Dr. Seniz Sörgel (ehem. Beyazyildirim), Dr. Linas Vilciauskas, Qian Cao and Renee Stotz.

Last but not least, I also want to express my deepest gratitude to my parents who always support me. My deepest thanks go to my lovely wife, Yanpeng Fu, who supports me through all the time of this thesis with her love and encouragement.

Curriculum Vitae

Name: **Changbao Zhu**

Date of Birth: 19.06.1982

Place of Birth: Zhangjiakou, Hebei, China

Education:

- ◆ 2009-present Max Planck Institute for Solid State Research, Stuttgart, Germany
Ph.D. candidate, plan to graduate in spring, 2013
- ◆ 2007-2009 European master program (Erasmus Mundus scholarship), France
Materials for Energy Storage and Conversion, **overall ranking: 2/26**
- ◆ 2005-2007 Xiamen University, Xiamen, Fujian, China, Master of Science
Majored in physical chemistry, electrochemistry
- ◆ 2001-2005 Chongqing University, Chongqing, China, Bachelor of Engineering
Majored in Applied chemistry, **overall ranking: 1/60**

Research Experiences:

Max Planck Institute for Solid State Research, 2009-present

Ph.D. thesis and European master thesis

Research Advisor: Prof. Joachim Maier

- Defect chemistry of $\text{LiFePO}_4/\text{FePO}_4$ redox couple
- Morphology controlled synthesis of LiFePO_4 by electrospinning method
- Controlled synthesis of LiFePO_4 nanoparticles by surfactant-assisted polyol method
- Size effects in LiFePO_4
- Staging effect and phase transition in $\text{LiFePO}_4/\text{FePO}_4$

Xiamen University, 2005-2007, master thesis

Research Advisor: Prof. Yong Yang

- Investigation on the solid-solid interface between lithium electrode and polymer electrolyte with in-situ micro-FTIR technique
- PEO-based polymer electrolyte with room temperature ionic liquids
- Practical production of LiFePO_4 cathode materials

Chongqing University, 2005, bachelor's degree thesis

Research Advisor: Prof. Shengtao Zhang

- Study on mass transfer mechanism near electrode surface in electrolyte in chromium redox flow batteries

Awards and Honors:

- ◆ Chinese Government Award for Outstanding Self-Financed Students Abroad, 2011

- ◆ Erasmus Mundus Scholarship, France, 2007-2009
- ◆ “Outstanding Student”, Xiamen University
- ◆ “Tang Zhongying Scholarship”, for every year(total 4 times), Chongqing, 2001-2005
- ◆ “Excellent Graduate Student in Chongqing”, Chongqing University, 2005
- ◆ “Excellent Graduate Student in Chongqing University”, Chongqing University, 2005
- ◆ “Excellent innovative example for science and technology”, Chongqing University
- ◆ “Excellent Student”(2%), Chongqing University, (twice) ,2002-2003
- ◆ “Outstanding Student”(1%), Chongqing University, for every year(total 3 times),2001-2005
- ◆ “The Scholarship of Excellent Undergraduate”, Chongqing University, for every semester (total: 7 times, first prize:3 times), 2001-2005
- ◆ The third prize in the 2004 National English Contest for College Students

Leadership training:

- Chairman of Stuttgart branch of Chinese academic organization of chemistry and chemical engineering (GCCCD), 2010-present, organizing 22nd GCCCD annual meeting (56 people participate from all over Germany)
- Member of “Young Volunteers Association” 2002-2005
- Commissary in charge of studies 2001-2005

Teaching Experience:

Teaching assistant of physical chemistry experiment in Xiamen University 2006.9-2006.12

Peer-reviewed publications:

1. **C. Zhu**, Y. Yu, L. Gu, K. Weichert, and J. Maier, Electrospinning of Highly Electroactive Carbon-Coated Single-Crystalline LiFePO₄ Nanowires, *Angew. Chem. Int. Ed.*, 50, 6278 (2011).
2. **C. Zhu**, K. Weichert, and J. Maier, Electronic Conductivity and Defect Chemistry of Heterosite FePO₄, *Adv. Funct. Mater.*, 21, 1917 (2011).
3. **C. Zhu**, H. Cheng, Y. Yang, Electrochemical Characterization of Two Types of PEO-Based Polymer Electrolytes with Room-Temperature Ionic Liquids, *J. Electrochem. Soc.*, 155, A569 (2008)
4. L. Gu, **C. Zhu**, H. Li, Y. Yu, C. L. Li, S. Tsukimoto, J. Maier, and Y. Ikuhara, Direct Observation of Lithium Staging in Partially Delithiated LiFePO₄ at Atomic Resolution, *J. Am. Chem. Soc.*, 133, 4661 (2011).
5. Y. Yu, L. Gu, **C. Zhu**, P. A. van Aken, and J. Maier, Tin Nanoparticles Encapsulated in Porous Multichannel Carbon Microtubes: Preparation by Single-Nozzle Electrospinning and Application as Anode Material for High Performance Li-based Batteries, *J. Am. Chem. Soc.*, 131, 15984 (2009).
6. Y. Yu, L. Gu, **C. Zhu**, S. Tsukimoto, P. A. van Aken, and J. Maier, Reversible Storage of Lithium in Silver-Coated Three-Dimensional Macroporous Silicon, *Adv. Mater.*, 22, 2247 (2010).
7. Y. Yu, L. Gu, X. Lang, **C. Zhu**, T. Fujita, M. W. Chen, and J. Maier, Li Storage in 3D Nanoporous Au-Supported Nanocrystalline Tin, *Adv. Mater.*, 23, 2443 (2011).
8. K. Weichert, W. Sigle, P. A. van Aken, J. Jamnik, **C. Zhu**, R. Amin, T. Acartürk, U. Starke,

- and J. Maier, Phase Boundary Propagation in Large LiFePO₄ Single Crystals on Delithiation, *J. Am. Chem. Soc.*, 134, 2988 (2012).
9. X. He, L. Gu, **C. Zhu**, Y. Yu, C. L. Li, Y.-S. Hu, H. Li, S. Tsukimoto, J. Maier, Y. Ikuhara, and X. Duan, Direct Imaging of Lithium Ions Using Aberration-Corrected Annular-Bright-Field Scanning Transmission Electron Microscopy and Associated Contrast Mechanisms, *Materials Express*, 1, 43 (2011).
 10. H. Cheng, **C. Zhu**, M. Lu and Y. Yang, Spectroscopic and Electrochemical Characterization of the Passive Layer Formed on Lithium in Gel Polymer Electrolytes Containing Propylene Carbonate, *J. Power sources*, 173, 531(2007)
 11. H. Cheng, **C. Zhu**, B. Huang, M. Lu and Y. Yang, Synthesis and Electrochemical Characterization of PEO-Based Polymer Electrolytes with Room Temperature Ionic Liquids, *Electrochim. Acta*, 52,5789(2007)
 12. H. Cheng, **C. Zhu**, M. Lu and Y. Yang, In Situ Micro-FTIR Study of the Solid–Solid Interface between Lithium Electrode and Polymer Electrolytes, *J. Power sources*, 174, 1027(2007)
 13. H. Cheng, **C. Zhu** and Y. Yang, FTIR Characterization of Ion Association and Phase Composition in PEO-based Polymer Electrolytes, *ACTA CHIMICA SINICA*, 65, 2832(2007)

Paper to be submitted:

1. **C. Zhu**, K. Weichert, L. Gu, J. Popovic, and J. Maier, Controlled synthesis of LiFePO₄ nanoparticles and related electrochemical effects
2. **C. Zhu**, L. Gu, L. Suo, J. Popovic, H. Li, Y. Ikuhara, and J. Maier, Size-dependent staging and phase transition in LiFePO₄/FePO₄
3. **C. Zhu**, K. Weichert, J. Popovic, and J. Maier, Lithium potential variations for metastable materials: case study of nanocrystalline and amorphous LiFePO₄

Patents:

1. Y. Yang, Z. Zhang, **C. Zhu**. New synthesis method to prepare LiFePO₄ cathode materials based on phosphorous site doping, *Chinese patent*, application number: 200710008713.2

Selective Conferences:

1. **C. Zhu**, Y. Yu, L. Gu, K. Weichert, and J. Maier, Carbon-coated single-crystalline LiFePO₄ nanowires, 2011 Lithium Battery Discussions (LiBD), Arcachon, France, 12-17 June, 2011, oral talk.
2. **C. Zhu**, L. Gu, K. Weichert, Y. Yu, H. Li and J. Maier, Size effect of LiFePO₄ cathode materials, 16th International Meeting on Lithium Batteries (IMLB 2012), Jeju, Korea, 17-22 June, 2012, poster.
3. **C. Zhu**, L. Gu, K. Weichert, J. Popvic, H. Li, and J. Maier, effect of LiFePO₄ cathode materials, 2013 MRS Spring Meeting, San Francisco, California, USA, 1-5 April, 2013, oral talk.